DEVELOPMENT OF A TIME RESOLVED SCANNING PARTICLE IMAGE VELOCIMETRY SYSTEM FOR MEASUREMENT OF THE SMALL SCALES OF TURBULENT FLOWS

by

MARIA DEL MAR TORREGROSA

A thesis submitted to the

Graduate School-New Brunswick

Rutgers, The State University of New Jersey

in partial fulfillment of the requirements

for the degree of

Master of Science

Graduate Program in Mechanical and Aerospace Engineering

written under the direction of

Professor Francisco Javier Diez

and approved by

_____

_____

_____

New Brunswick, New Jersey

May, 2009

ABSTRACT OF THE THESIS

Development of a Time Resolved Scanning Particle Image Velocimetry System for Measurement of the Small Scales of Turbulent Flows

by MARIA DEL MAR TORREGROSA

Thesis Director:
Professor Francisco Javier Diez

Our knowledge of the quasi-universal intermediate and small scales of turbulent shear flows is incomplete and is a common topic of great interest in modern turbulence research. The temporal and spatial complexity of the turbulent flows at such small scale has prevented the acquisition of full experimental data sets for validating classical turbulent theory and direct numerical Simulations (DNS). To better understand these phenomena, a Time Resolved Scanning PIV system was developed to take three-dimensional two- component velocity data at the small scales of turbulent flows. The TR SPIV system was designed, set-up and tested. A criterion based on the PIV nature of the measurements and basic turbulence concepts is proposed for the determination of the minimum turbulent scales that the system can measure.

Quasi-instantaneous volumetric vector fields at the far field of a round turbulent jet in water (Re~1,500) were reconstructed and studied. The spatial and temporal resolution of

the system allowed the visualization of velocity fields at Taylor length scales of the flow and its evolution in time. According to the quasi-universality theory on turbulent inner scales, the inner-variables scaling become Reynolds independent, and this was validated with the probability density functions of the velocity gradients.

ACKNOWLEDGEMENTS

I would like to thank my advisor, F. Javier Diez, for giving me the great opportunity of coming to Rutgers. Without his guidance, assistance and suggestions, this project would have not been possible. I am grateful for his patience on reading and checking my numerous revisions.

Also thanks to my committee members, Doyle Knight and Stephen Tse, for their time and contributions to this work.

Thanks specially to John Petrowski, for his help on setting up the scanning mirror system, and his helpful assistance in any question I had for him. And thanks to Sunny Wong for his help with the calibration of the scanning mirror.

I would like to thank Ye Cheng for being there for me, at home, class, lab… even off-campus; and sharing with me almost every single aspect of this experience. I would also like to thank Mariusz Zarzecki for his thoughtful comments; and to all the crew in D-124. Thanks to Antonio Moral, Hatice Tekiner, Tyree Oredein and Mohannad Abdo for every single moment they share with me, giving my life here some sense. Also thanks to Bahar, Renata, Eyup, Basar, Mete, Vanesa, Angela, Reyes, Domi, and Tyree's mom, for making my life enjoyable in the USA.

Finally, I would like to thank my parents, Pilar Galindo and Francisco Torregrosa, my sisters Pili y Yiyi Torregrosa, and grandma Ana Baez for their continuous support, love and understanding.

TABLE OF CONTENTS

LIST OF TABLES

LIST OF FIGURES

CHAPTER I

Introduction

1.1 Motivation and background

Many experiences of turbulent flows accompany us in our everyday surroundings, such as the flow around an automobile, the water in a river, or the plume formed by a solid rocket motor. In observing the smoke from a chimney, turbulent motions of many scales can be observed, from eddies comparable in size to the width of the chimney, to the smallest scales size that the naked eye can see. Far from a constant flow, we can observe that these flows are unsteady, irregular, seemly random and chaotic. These features are common to all turbulent flows.

The turbulence "problem" is not yet solved to the degree that we are not capable to predict many practical turbulent flows. There is a vast literature on turbulence and turbulent flows, describing aspects such as how the turbulent flows behave, how can they be described quantitatively and what are the physical processes involved [1].

To simulate the behavior of turbulent flows, approaches such as Reynolds-stress modeling, probability density function (PDF) methods, and large-eddy simulation (LES)

models have been developed. In principle, such LES improved the accuracy in simulating turbulent flows, though current models do not provide very accurate representations for the turbulent transport of mass, momentum and energy between the resolved and subgrid scales [2]. Results from DNS studies succeeded in reaching Taylor-scale Raynolds numbers up to Re_v=1,217, and served to confirm the classical turbulence theory for homogeneous isotropic turbulence [3]. Development of improved subgrid-scale models for LES require a further understanding of the physical structure, statistics and dynamics of the intermediate and small scales of turbulent shear flows.

On the other hand, experimental methods have been limited to techniques that measure 2-D sections of a flow. But flow properties typically vary temporally and throughout the 3-D space. To the date, due to the temporal and spatial complexity of the turbulent flows, it has been difficult to resolve experimentally the intermediate and small scales, and these issues have been primarily studied by direct numerical simulation (DNS).

The present study has developed a Time-Resolved Scanning Particle Image Velocimetry (TR-SPIV) technique for experimental investigation of properties of velocity fields associated with the small scales of turbulence in a turbulent shear flow. The main objectives of this thesis work were to design, assemble and set up the system. A criteria related to the turbulent properties of the small scales of the flow has been proposed for the study, and the capability and limitations of the technique are discussed. Further more, the technique was applied to a typical turbulent shear flow in order to validate the method with previous measurements and explore the potential of the system in the observation of

the small scales of turbulent shear flows. Volumetric 2D velocity and velocity related measurements were obtained in a turbulent jet.

1.2 Review of Particle Imaging Techniques for flow measurement

There are many measurements techniques for flow velocity measurement. Intrusive methods such as hot wire anemometry and pulsed wire anemometry provide measurements at single probe locations, limiting the spatial resolution of the techniques to a few number of probe locations. On the other hand, imaging techniques such as Particle Image Velocimetry are non-intrusive methods that do not influence the flow directly.

Particle Image Velocimetry (PIV) is a measurement technique that has been used extensively in fluid dynamic investigations for the last two decades [4]. The technique involves the processing of particle images captured from a fluid seeded with tracers to obtain mean displacements. A typical experimental arrangement for PIV is shown in Fig. 1.1. In PIV, the flow is seeded with a high density of seed particles, suspended in the flow to follow the motion. A light sheet illuminates the tracer particles at a thin slice of the flow field, and the scattered light from the tracers is detected by a camera. The light sheet, usually generated by a pulsed laser source, is pulsed twice at a known interval. Camera images are recorded, showing the initial and final positions of the particles due to the movement of the flow field during the time interval. Common PIV techniques record the particle images at two light pulses in two separate frames; while alternative approaches apply single-frame recording with double- or multi-pulses. The two camera

frames are processed to find the displacement of particles between frames. Instead of evaluating the motion of individual particles, the displacement of groups of particles is obtained instead. The image frames are divided into small sections called interrogation areas and correlation techniques are used to measure the displacement of the group of particles in each interrogation area between the two frames. The velocity vector corresponding to the interrogation area is calculated using the known time between frames and the distance that corresponds to the particle group displacement in the camera image [5]. As a result, a vector field of the two in-plane components of the velocity at the illuminated plane is obtained.

Continuous improvements in computing power, data transfer and storage, and camera and laser technology have made dramatic advances in the last few years; allowing the study of spatial and temporal flow features with increasing detail. To the date, Time Resolved PIV (TR PIV) experimental fluid techniques can achieve repetition rates up to 2,000 Hz for full High Speed Camera image resolutions of 1,024 x 1,024 pixels. Recently, Chiuan-Ting li *et al* (2009) used High Speed PIV to study a turbulent mixing layer. With a frame rate of 2,565 fps and a field of view of 60x60 mm^2 (512 x 512 $pixel^2$), they measured mean and fluctuating velocities for a fluid with local Taylor micro scale fluids of around 2 mm, and compared the results with the measurements taken with a Hot-Wire prove at a sampling rate of 10 kHz.

Scanning PIV combines conventional PIV with scanning techniques to obtain the two components of the velocity field in a set of light-sheet planes across a volume [7]. For

scanning frequencies adjusted sufficiently high compared to the characteristic time-scale of the flow measurements, the measurements can be considered as quasi-instantaneous over a scan cycle. Burgmann *et al* (2006) applied scanning PIV to investigate structure and dynamics of vortices in a laminar separation bubble. They used 10 diode lasers to create 5 parallel measurement planes separated 2.5 mm as shown in Fig. 1.2, which scanned the measurement volume within 2 seconds to resolve the temporal evolution of the flow in the different planes.

PIV can be extended to measure all three velocity components by adding a second camera to the set-up. The Stereo PIV (SPIV) technique uses two cameras looking at the same particle field illuminated by a light sheet from different angles [7][9]. The stereoscopic configuration allows the measurement of the out-of-plane displacement of the particles, providing the three components of the velocity field on a single plane. Matsuda and Sakakibara (2005) applied a 30 fps Stereo PIV to obtain two-dimensional three component velocity distributions of turbulent outer scale vertical structures in a round free jet with Reynolds numbers of 1,500-5,000. Assuming Taylor's frozen hypothesis based on the convective local mean velocity of the flow, they reconstructed the nine components of the velocity gradient tensor to study the vortical structures of the jet. Burgmann *et al* (2007) combined scanning and Stereoscopic PIV to measure the spatial structure of the flow of a separation bubble on an airfoil. The stereo scanning PIV set-up included two High Speed cameras and ten infrared laser sources that created ten successive parallel lights with a separation of 1 mm in between. The control volume of 80x40x10 mm^3 was scanned in sequences, with a volume recording rate of 92.2 Hz. Hori

and Sakakibara (2004) applied the Stereo Scanning PIV technique to obtain the three dimensional three component velocity distribution of a turbulent round free jet of Re~1,000, using the set-up sketched in Fig 1.3. With a measurement volume of 100x100x100 mm^3 scanned by 50 planes in 0.22 s, their study is focused in the vertical structures at the outer length scales of the jet.

In the study of the quasi-universal intermediate and small scales of a turbulent jet flow, Mullin *et al* (2005) applied simultaneous independent stereo PIV measurements in two differentially spaced light sheet planes. The setup sketched in Fig. 1.4 included two different laser frequencies combined with optical filters, and four cameras arranged in stereoscopic configuration. The results allowed for the resolution of the complete nine-component velocity gradient tensor fields of high Reynolds numbers jets, up to 30,000.

Another imaging method known as “dual-plane PIV” or “spatial correlation” technique, is based on the analysis of the characteristics of the correlation peaks to obtain the out-of-plane velocity component [14]. According to this technique, the height of the correlation peak can be related to the velocity of the particles in the out-of-plane direction. To avoid influence of other parameters, an additional parallel light sheet is required to normalize the peak height. The generation and positioning of the additional light sheet and the required high particle density limit the applications of the system.

A different approach to obtain three dimensional measurements is Holographic PIV. With this technique, the amplitude and phase of the light scattered by particles dispersed in a fluid is processed to locate the position of the particles at two or more instants in time,

obtaining al three components of the fluid velocity throughout an extended volume [15]. The complexity of the calibration and processing of the images, the depth of field and the currently available size of the CCD sensor cells are the main limitations of this technique.

Three dimensional Particle Tracking Velocimetry (3D PTV) reconstruct the Lagrangian trajectories of individual particles in three-dimensional space, providing three component vectors in a 3D measurement volume. This technique is based on the acquisition of image sequences from different views using at least two cameras, although three or four cameras are more common. Recently, T.G. Hwang *et al* (2008) used three High Speed cameras to obtain velocity vectors of the flow field of an impinging jet flow of Re=30,000 at the characteristic outer length scales of the flow by 3D PTV. The application of this technique is considered not appropriate to measure small scales of turbulent flows due to the spatial resolution being limited by the separation required between particles to allow the particle tracking. Future work in 3D PTV may remove this limitation.

In Tomographic PIV, the 3D light intensity field of the illuminated particles is reconstructed from the images of four cameras looking at the control volume from different angles by optical tomography. The velocity vectors in the volume are computed by an iterative three dimensional cross correlation technique. The experiments performed by Elsinga *et al* (2006) allowed the reconstruction of 650 kvectors per volume, providing a clear visualization of the flow structures of the wake behind a circular cylinder and the turbulent boundary layer developing over a flat plate.

The scanning PIV technique was chosen for the present study among the imaging techniques described above due to the high spatial and temporal resolution required to study the flow at the quasi universal small scales of turbulent flows and the relative easy implementation by means of only one High Speed Camera.

1.3 Present study

The Time Resolved Scanning Particle Image Velocimetry developed for measurement of the quasi-universal small scales of turbulent flows is described in Chapter II. The chapter compiles the key elements to be considered on the design and calibration of the different components of a TR SPIV.

A criterion proposed for determining the appropriate spacing between scanning planes for the TR SPIV system is explained in Chapter III. The criteria involve the interpretation of the inner scales of the flow and the definition of an “effective thickness” of the laser sheet, along with a method proposed to measure such thickness.

Chapter IV describes the set up for the turbulent jet used to validate the TR SPIV system along with the final settings for the optical arrangement and synchronization according to the criteria described in Chapter III.

The study of volumetric velocity fields on the small scales in the turbulent shear flow are presented in Chapter V. Results of the quasi-instantaneous volumetric 2-D velocity vector

fields and velocity gradients are illustrated, along with the statistics of the *u*-and-*v* velocity gradients in the *x*-, *y*- and *z*- direction.

Chapter VI includes the conclusion remarks and the suggestion for future work on the measurement of the small scales of turbulent flows.

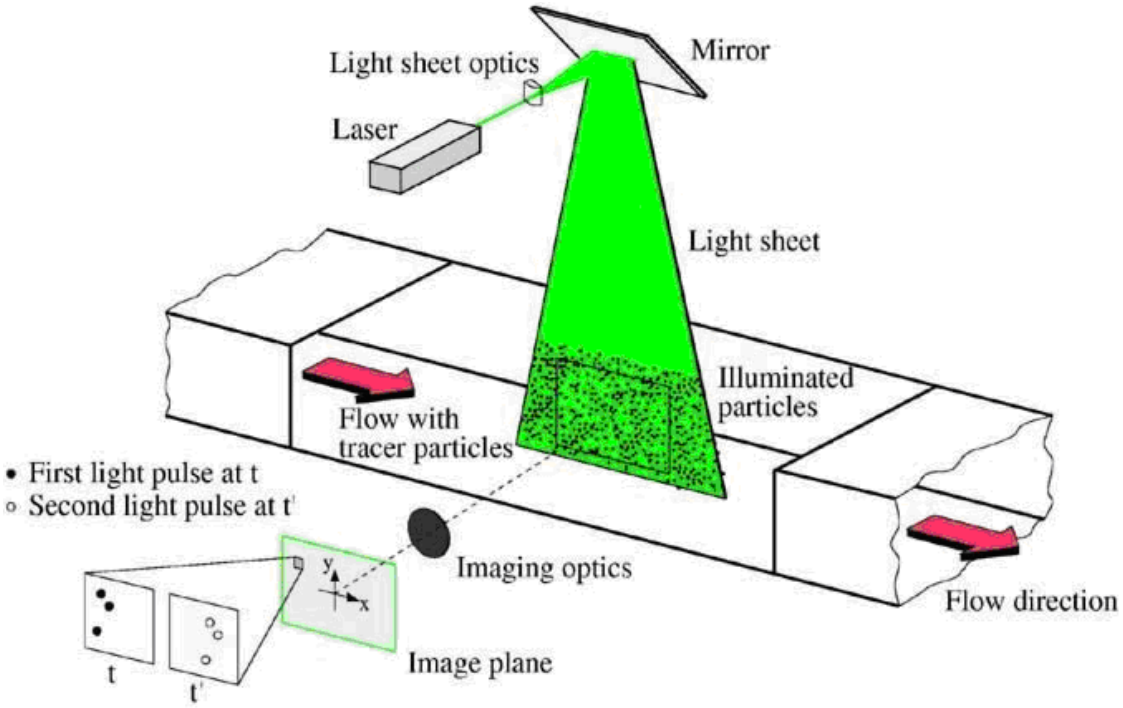

Figure 1.1. Typical configuration of a Particle Image Velocimetry system (Raffel *et al* [5])

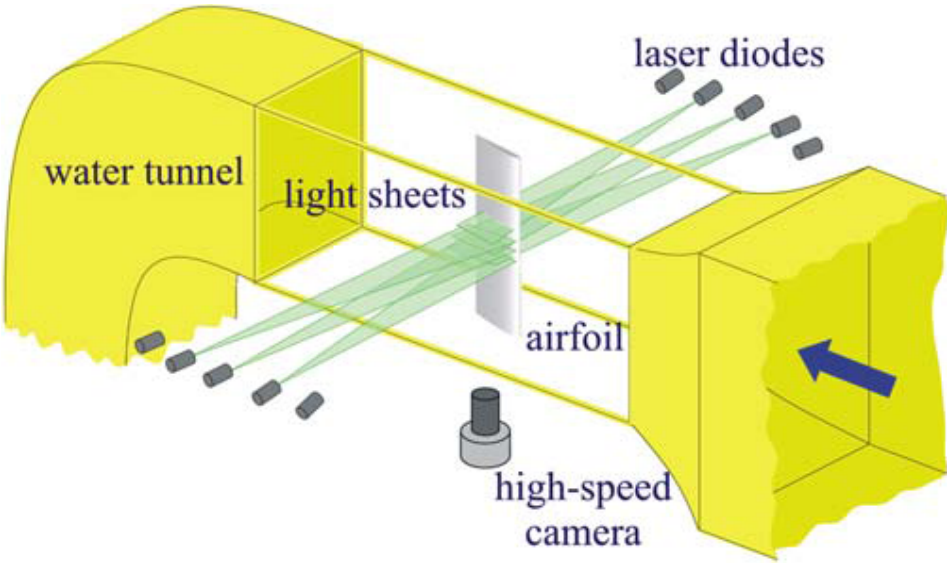

Figure 1.2. Sketch of the laser sheet scanning system used by Burgnmann *et al* [8]. Ten diode lasers were used to create 5 parallel measurement planes.

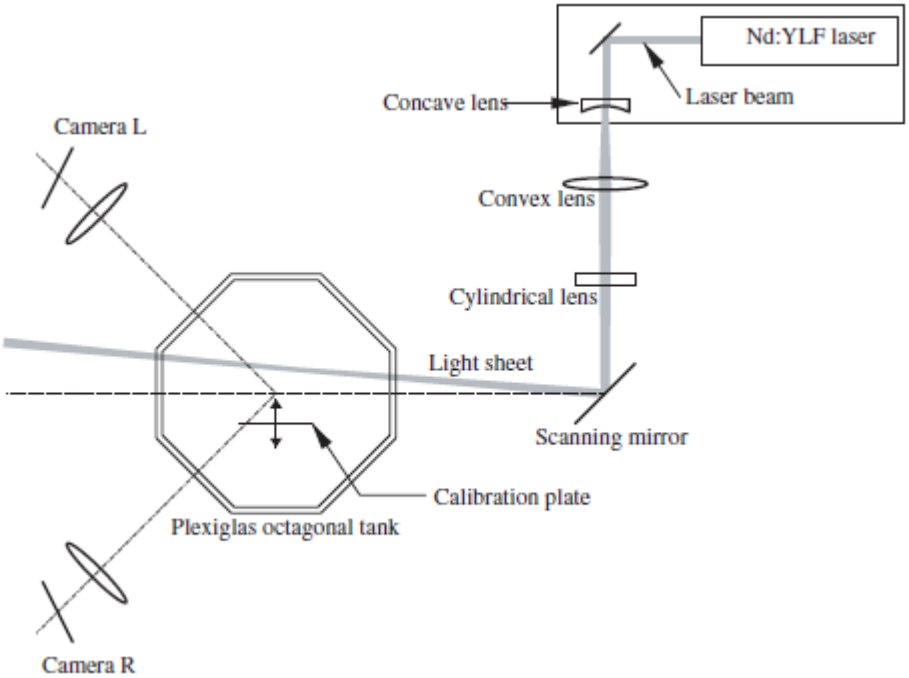

Figure 1.3. Optical arrangement of the High Speed Stereo Scanning PIV used by Matsuda and Sakakibara [10]. The laser sheet was scanned with a flat mirror mounted on an optical scanner controlled with a programmable scanner controller

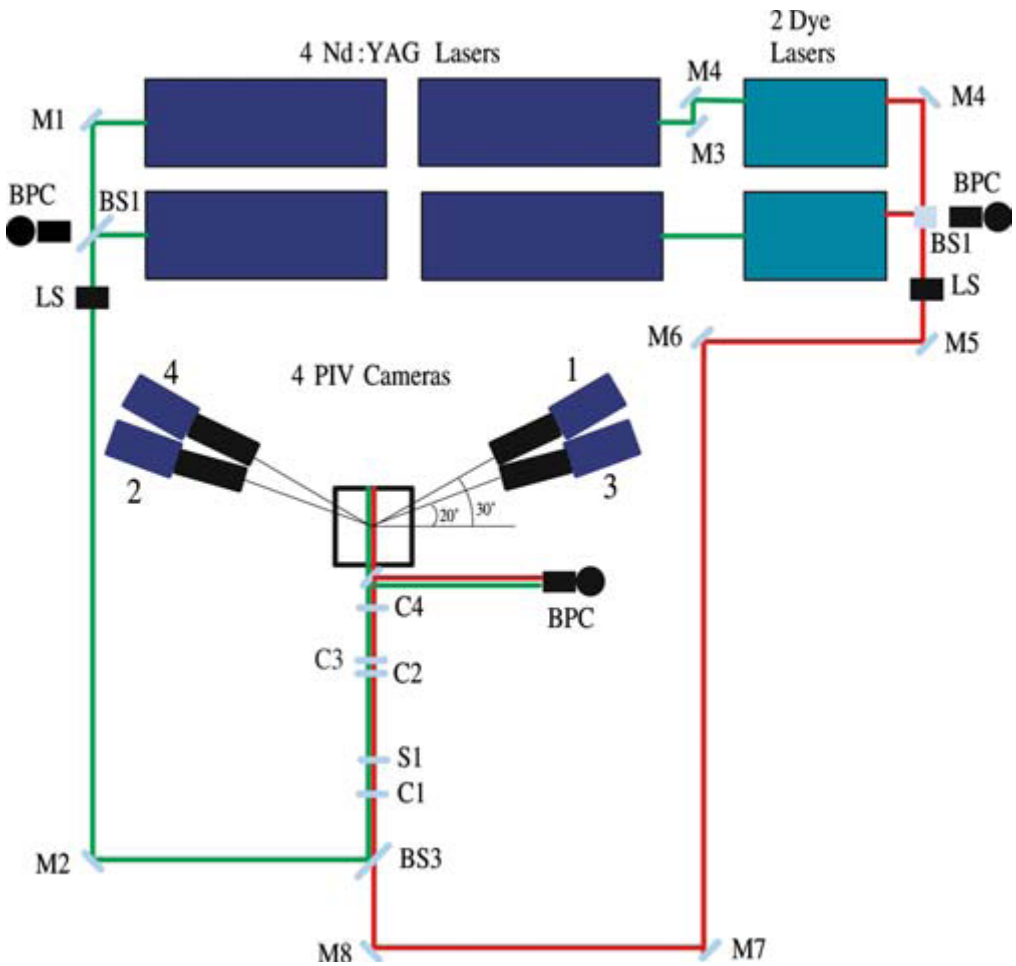

Figure 1.4. Basic layout of the dual-plane stereo PIV system used by Mullin *et al* [13]. Two Nd:YAG lasers provided double-pulsed green light sheet and two additional Nd:YAG lasers pumped two dye lasers to provide double-pulsed red light sheet. Four PIV cameras were arranged in an asymmetric forward–forward scatter configuration

CHAPTER II

Time Resolved Scanning Particle Imaging Velocimetry

During the present study we have developed a high-resolution Time Resolved Scanning PIV (TR SPIV) system. This diagnostic capability has been designed to investigate the quasi-universal intermediate and small scales of turbulent shear flows. This chapter describes the key elements to be considered on the design and calibration of the different components that are part of the system.

The TR SPIV system developed for this study, shown in Fig. 2.1, consisted of a Nd:YAG laser, a High Speed CMOS camera, and a rotating mirror attached to a servomotor. A set of lenses was used to generate the laser sheet, and optic mirrors are used to set the trajectory of the laser beam.

Camera and laser were triggered by a synchronizer (digital delay generator) connected to a computer. The angle and speed of a rotating mirror were controlled by an electric signal created with a signal generator. Laser, camera and mirror were synchronized so that the laser light scanned the same space volume at precise intervals. During each volumetric

scan time, the laser reflected of the mirror at specific angles (based on mirror angle), creating laser sheets at different times and locations, approximately parallel to each other, as shown in Fig. 2.2. Single-color, single-exposure images of the particles illuminated by each of the laser sheets were captured with the high speed camera. The images taken in the same plane at different times were rearranged in pairs and analyzed with a cross correlation algorithm to determine the two in-plane velocity components. The consecutive PIV image planes were rearranged to recreate the velocity field in a volume.

Key elements of this technique that will be discussed include the generation of the laser sheets, the particle image acquisition, and the synchronization scheme between laser, camera and scanning mirror. These aspects are discussed in Sections 2.2 - 2.5.

2.1 Particles Stokes number criteria

Measurements taken with a Particle Image Velocimetry system are based on the displacement of the particles seeded into the flow as tracers of the fluid motion. Therefore, it is important to check that the particles are capable of following the flow.

The particles Stokes number, *St*, expresses the capability of the tracers to follow the fluid motion. The Stokes number relates the characteristic particle and flow time scales (τ_p and τ_δ respectively), as expressed as [18][19]

$$St = \frac{\tau_p}{\tau_\delta} \tag{2.1}$$

It can be assumed that the tracers follow precisely the flow when the particles stokes number is smaller than 0.5 [19].

The particle time scale, τ_p, also known as relaxation time, can be calculated for spherical particles using Stokes Drag Law as shown in Eq. 2.2. This is a convenient measure of the tendency of the particles to attain the velocity equilibrium within the fluid.

$$\tau_p = d_p^2 \frac{\rho_p}{18\mu} \tag{2.2}$$

In Eq. 2.2 ρ_p is the particle mass density, d_p the mean particle diameter, and μ the fluid dynamic viscosity.

The characteristic flow time scale of the energy-containing eddies for turbulent flows is calculated from the local outer length and velocity scales, $\delta(x)$ and $u_c(x)$, respectively, as

$$\tau_\delta = \frac{\delta(x)}{u_c(x)}. \tag{2.3}$$

For turbulent jets in free flow, the local outer velocity scale, $u_c(x)$, is the local centerline velocity; and the local outer length scale, $\delta(x)$ represents the full width over which the mean velocity profile drops 95% of its local peak value (centerline velocity) [20].

It will be shown in Chapter IV that the calculated characteristic flow time scale for the experimental conditions described is ~8.6 seconds, and the particles Stokes number is $7.4 \cdot 10^{-9}$ seconds. These meet the criterion described above, and it confirms the tracers followed the flow accurately.

2.2 Light sheet generation

In order to take measurements in planar sections of the flow, the tracer particles were illuminated using a thin laser sheet created by an Nd-YAG 532 nm pulsed laser source. The laser beam profile had an intensity distribution that can be approximated by a Gaussian function, with a diameter of about 3.3 mm. Figure 2.3 shows the intensity profile across the laser beam measured at 100 mm from the laser source.

The beam traveled through a sheet-forming optical path that consisted of two spherical lenses and a cylindrical lens, as represented in Fig. 2.4. All of them were placed in an optical table that kept the beam aligned with the optical axis of the lenses.

The laser mirror, M_1, was used to direct the laser beam towards the desired direction from the fixed position of the laser head.

Both spherical lenses, L_1 and L_2, were identical, plane-convex lenses, with a focal length of 1 meter. They were used to reduce the width of the round laser beam and focus it at the desired position. Using the paraxial theory and Gaussian lens approximation for thin lenses[21], the position of the focal point resulted from the combination of the two thin lenses, with a collimated beam hitting lens L_1, can be calculated as follows

$$f = \frac{(d - f_1) f_2}{(d - f_1 - f_2)}, \tag{2.4}$$

where d is the separation between the lenses (100 mm), f_1 and f_2 are the focal length of lens L_1 and L_2, and f is the location of the focal point of the combines optic respect to the

last lens (L_2). The resulting focal point for the experimental set up shown in Fig. 2.4 was 473 mm.

The laser beam had its minimum diameter at the focal point of the combined optics (i. e. the waist of the beam). Complex calculations, based on very restrictive assumptions including a Gaussian shape of the beam, are required to determine the waist thickness and length for a combination of two spherical lenses [21]. Due to the complexity of the calculations, the beam waist was determined experimentally for the present study. The procedure used to characterize the light distribution across the laser sheet, and to determine the waist length, is described in Chapter III. The resulting waist of the beam, determined from the second momentum of the Gaussian intensity distribution, was measured to be 2.07 mm. The beam waist remained constant for at least 100 mm around the focal point.

The 15 mm plane-concave cylindrical lens, L_3, was positioned 75 mm after the lens L_2, and used to transform the round incident laser beam into an expanding sheet of light. The calculated total height of the beam at the beginning of the measurement section was 62 mm, which doubled the size of the height of the test section; and therefore it can be assumed that the field of view images by the camera in the plane of the laser sheet was evenly illuminated.

The scanning mirror was located 5 mm after the cylindrical lens L_3, and positioned at its mechanical zero position, which corresponded to 45 degrees respect to the incoming beam.

In the design of the optical arrangement for a PIV experiment, the set up had to be properly designed to guarantee the uniformity of the laser sheet along the field of view, with an appropriate thickness and light intensity that allows a minimum particle density for the desired size of interrogation window. Therefore, the focal length of the spherical lens had to be chosen accordingly to the cylindrical lens radius, and the desired size of the field of view.

2.3 Particle imaging

The accuracy of the PIV measurements depends largely on the quality of the particle images and the accuracy of the inferred particle displacements. These issues are related to camera focusing aberrations and distortions, which affect the particle images. As a general rule, the size of individual particles should be 2 to 4 pixels to estimate with sub-pixel accuracy the centroid location of the particles [5].

The present scanning system was based on the PIV measurements taken on a number of approximately parallel planes. Those planes were nearly parallel to the camera objective, but at different distances from it, as illustrated in Fig 2.2. In order to keep the same measurement uncertainty in the different planes, it was desirable to keep a similar particle size along the different planes. The shutter aperture of the camera played an important

role on this matter. As well as letting more or less light into the camera, the size of the shutter aperture governs the 'depth of field'. The depth of field is the out of plane distance in an image, from foreground to background, that is in sharp focus. A small shutter aperture lets less light into the camera, allowing a bigger depth of field. The focal length of the lens also affects the depth of field available; the longer the focal length, the more restricted the depth of field. The aperture of the shutter used to be given as a number that represents the focal length of the lens divided by the diameter of the aperture. A larger '*f*' number, for example *f*:16, is actually a smaller pin hole, resulting in a bigger depth of field than for example *f*:8.

In the design of the scanning PIV system, the chosen shutter aperture had to be small enough to guarantee a sufficient field of view, with a particle image size similar in all the scanning planes, preferably a number between 2 and 4 pixels, for the reasons explained above. On the other hand, the minimum shutter aperture was limited, as the camera should capture enough light to distinguish the necessary amount of particles in each interrogation window.

For the present study, the particle size and density was investigated to provide the optimal experimental conditions. A particle density between 6 and 12 particles per interrogation windows is considered optimal [5]. PIV images were taken at different plane locations in the control volume (from the closest plane to the camera to the furthest plane from the camera) for different shutter apertures. A shutter aperture of 11 was determined to be the most effective for the present PIV application, with a particle size between the

desired range. Figure 2.5 shows actual particle images near the center plane of the volume (smallest particle size observed), and at closest and the furthest planes from the camera (biggest particle size observed) for a shutter aperture of 11.

2.4 Scanning mirror set up and calibration

An optical scanner allowed the control of the position of the laser sheet. It was positioned after the sheet forming optics described in Section 2.2. The system consisted basically of two parts: a mirror mounted on a galvanometer, also known as a rotating mirror; and a modular driver that drived the galvanometric servo-control.

The galvanometer was a GSI Lumonics VM500, with a mirror of 5 mm of clear aperture. This allowed a maximum scanning angle of ± 25 degrees respect to the mechanical zero position. The MiniSax (Miniature Single Axis) servo-controller was used to condition the signal to the galvanometer. The adjustment of the gain, offset and notch filter were factory-optimized for the fastest step response.

The signal input to the servo-controller was a triangular wave of adjusted peak to peak voltage and frequency, created with an HP 54601-B 100 MHz signal generator. A KH 1200A oscilloscope was used to visualize the electric signal applied to the MiniSax servo.

The scanning system was set up during this study. The servo-controller was assembled to allow for the signal input from the signal generator and the power supply; galvanometer

and servo controller were inter-connected, and a holding base for the scanning mirror unit built.

The scanning angle and rotation speed of the mirror were directly controlled with the voltage and frequency of the triangular wave from the signal generator. The "mechanical center" is defined as the scanner position when the power is off (zero Volts for the input signal). For a fix peak-to-peak voltage V_{pp} and frequency f_s, the mirror oscillated around its mechanical center at a constant speed, with an angle of $\pm\alpha/2$ degrees at the same frequency f_s. This is sketched in Fig. 2.6.

During the scanning system calibration, the relation between the peak-to-peak voltage V_{pp} applied and angle position was obtained. The scanning mirror was mounted such that it reflects a laser beam (He-Ne laser source) to a calibrated optical target, as shown in Fig. 2.7. The target was positioned perpendicular to the beam reflected from the mirror (at its mechanical center position) of the mirror, at 1.55 meters from it. The limits of the path illuminated by the scanning beam on the calibration target at different peak-to-peak voltages of the triangular wave were measured visually. The full angle corresponding to each peak-to-peak voltage was calculated and the results compared. The linear fit of the experimental data is shown on Fig. 2.8 and expressed as

$$\alpha = 0.0081 \cdot V_{pp} - 0.0283\,, \tag{2.5}$$

where α is the full rotating angle (in degrees) corresponding to the peak-to-peak voltage V_{pp} (in mV). Note that for a zero voltage, the calibration curve is not valid, and the angle α equals zero, corresponding to the mechanical center.

2.5 Image acquisition scheme and limitations

2.5.1 Image acquisition scheme

During an image acquisition sequence, the triangular wave signal to the scanner was set with frequency f_s and peak-to-peak voltage V_{pp}. Therefore, the scanning mirror rotated around its mechanical center a full angle α, describing a whole rotating cycle in a time period $T_{mr}=1/f_s$. During one full mirror scanning period T_{mr}, the laser beam was pulsed n_{lp} times, and reflected of the mirror with known angles. This is sketched in Fig. 2.9.

The timing between laser pulses was constant, and given by t_{lp}. The maximum mirror deflection angle was quite small, and, therefore, the control volume was illuminated by consecutive quasi-parallel pulsed laser sheets. On successive scanning periods, the laser reflected of the mirror at exactly the same angle positions.

Images taken for the same plane position, at two consecutive scanning sequences, were paired to form PIV images. A cross correlation algorithm was then applied to obtain the in plane velocity vector field. The timing between the frames that form the PIV images, dt, corresponds to the mirror scanning period T_{mr}. For two successive scanning mirror periods, a n_{lp} number of PIV pair of images were processed, and the vector fields of n_{lp} contiguous planes were grouped together to obtain the vector field in a volume.

The 2D vector fields obtained for the planes that compose the scanning volume were reconstructed on space to form a volumetric two-dimensional vector field. The planes

were positioned on a three dimensional grid as parallel planes, with a separation between planes according to criteria explained in Chapter III.

2.5.2 Laser-camera-mirror synchronization

The schematic of the overall system synchronization is represented in Fig. 2.10. Camera and laser were synchronized through a Laser Pulse synchronizer controlled by Insight 3G software. For a specified laser pulsed frequency f_L, the camera captured an image for each laser pulse, with the timing between laser pulses corresponding to $1/ f_L$. The software was triggered externally, and for each external trigger pulse, the software sends a preset number of pulses to the laser via the synchronizer, keeping the timing between laser pulses $1/ f_L$.

A TTL signal from a signal generator was used as external trigger for Insight 3G software. The number of laser pulses per trigger was set equal to the number of measurement planes in which the volume is scanned. The same signal generator was used to control the scanning mirror angle and to trigger the Insight 3G software.

The frequency of the scanning mirror rotation controlled by the signal generator is set to:

$$f_S = \frac{f_L}{n_{lp}} . \tag{2.6}$$

2.5.3 Limitations of the scanning system

- *Minimum individual acquisition time*

The minimum timing between laser pulses corresponds to the inverse of the maximum frequency of the one of the laser heads of Lee Laser, which is 20 kHz.

Camera and laser were synchronized to acquire a particle image for each laser pulse. The Photron Ultima High Speed Camera was controlled with the Insight 3G software. This allowed a maximum frequency of 1 kHz of individual images associated with one laser pulse (1 kHz of image pairs when using both laser pulses). The limiting speed of the system was the camera speed. Consequently, the fastest acquisition scheme corresponded to a time between laser pulses of 1,000 microseconds at the maximum resolution (1,024x1,024 pixels images). For a lower resolution of 1,024x512 pixels images, the minimum acquisition time is 500 microseconds.

- *Rotating mirror period and number of planes*

During one scanning period, the mirror rotates bouncing clockwise and counterclockwise around the mechanical zero position. The laser pulses were triggered to be reflected by the mirror only in its movement along one of the two directions of rotation. The relation between the number of measurements in a scanning volume (n_{lp}) and the rotating mirror period (T_{mr}), directly obtained from Eq. 2.6, is determined by:

$$T_{mr} = n_{lp} \cdot t_{lp} \,. \tag{2.7}$$

The scan time, t_{scan}, defined as the time that the light sheet takes to scan the test volume once, is calculated as follows:

$$t_{scan} = t_{lp} \cdot \left(n_{lp} - 1\right). \tag{2.8}$$

Also, the scan time limits the number of measurement planes. The relation between the scan time and the flow inner time scale is needed to be kept as small as possible (refer to Chapter III).

The maximum rotating frequency for the scanning mirror was 20 kHz, and therefore the scanning mirror timing was not a limitation for the experimental set up proposed.

Besides the relations stated in Eq. 2.7 and Eq. 2.8, the number of scanning planes was related to the depth of the scanning volume. The maximum number of planes that could be taken was also limited by the depth of field of the camera lens, which needs to keep a constant particle size for all image planes.

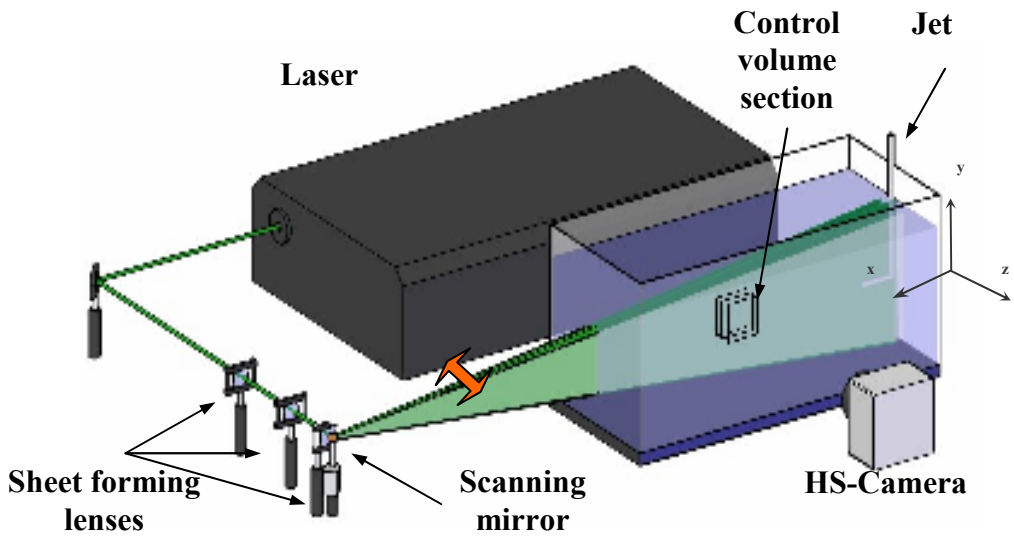

Figure 2.1. Set up of the TR SPIV system.

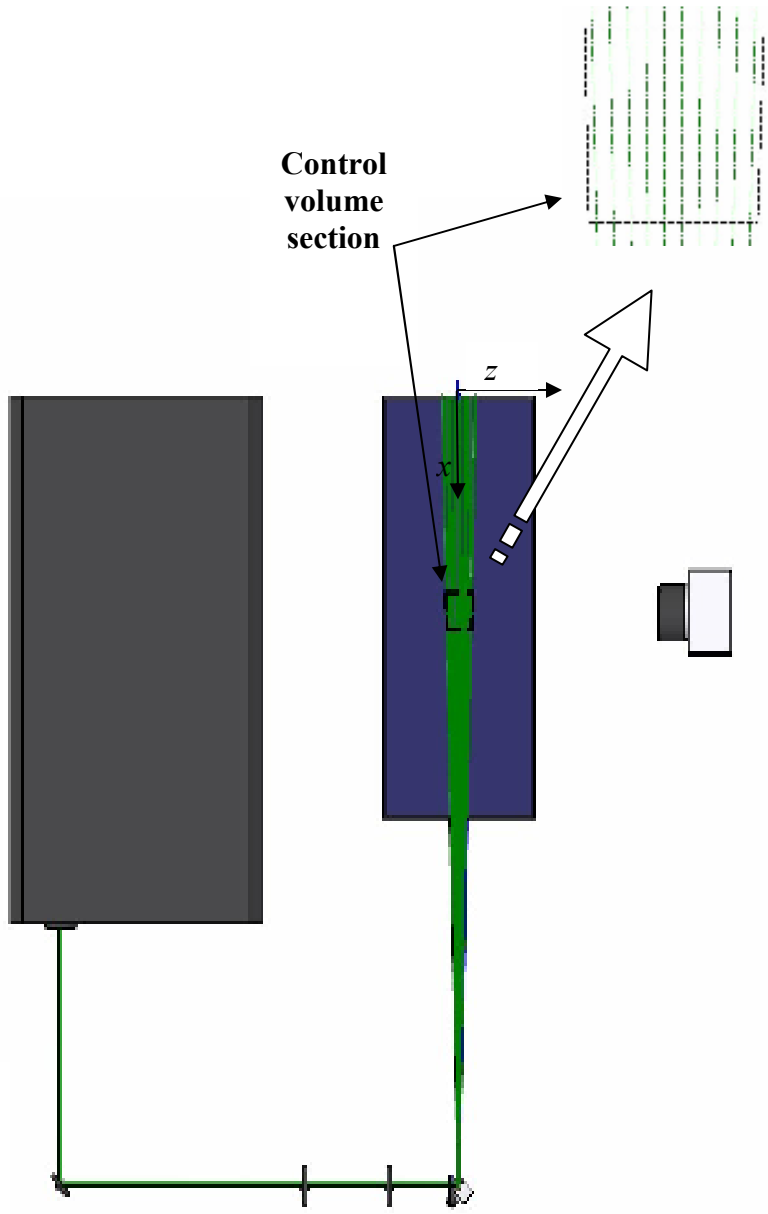

Figure 2.2. Top view of the TR SPIV system. During a scan period, volumetric scan time, 10 quasi-parallel light sheets scan the control volume (shown in inset).

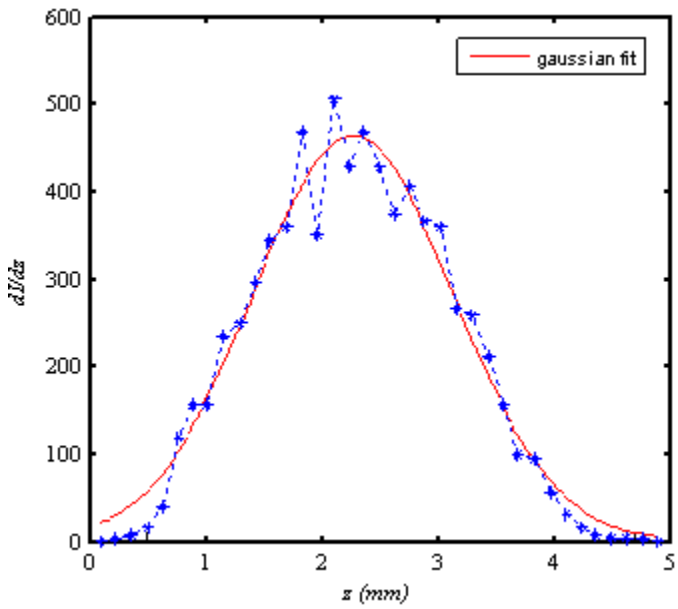

Figure 2.3. Intensity profile of the laser beam measured at 100 mm from the laser source. Data was fit with a Gaussian function.

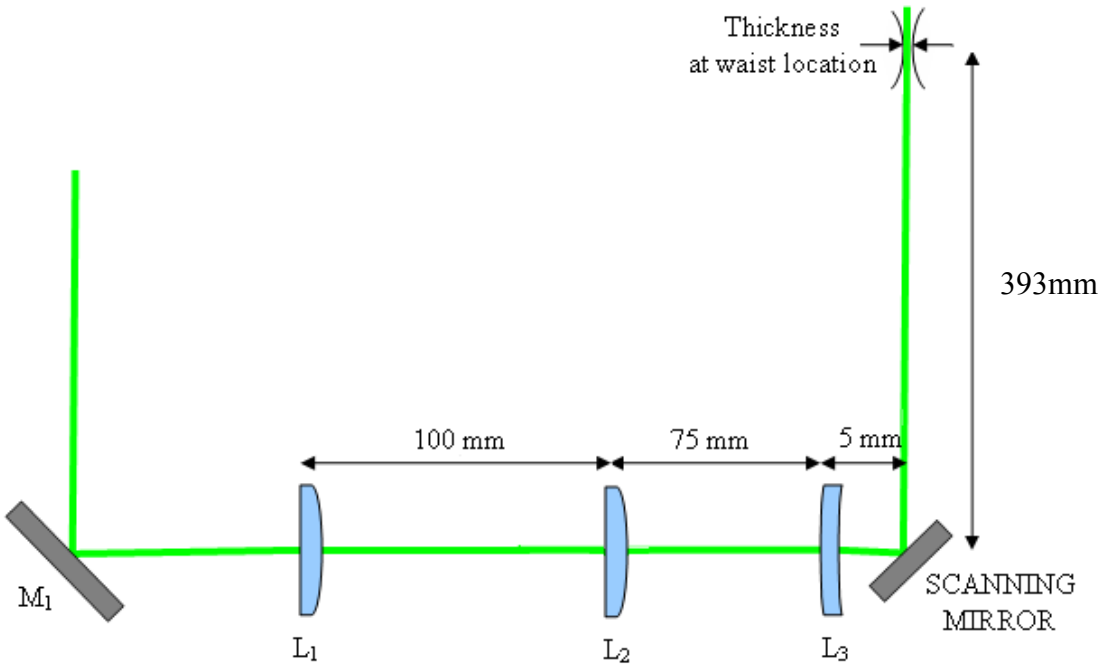

Figure 2.4. Schematic of the optical components used to generate the laser sheet. *M1* is an optical mirror; L_1 and L_2 are two identical plano-convex spherical lenses and L_3 a plane-concave cylindrical lens.

a)

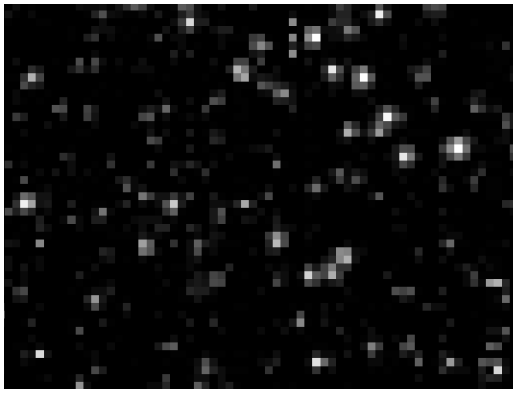

b)

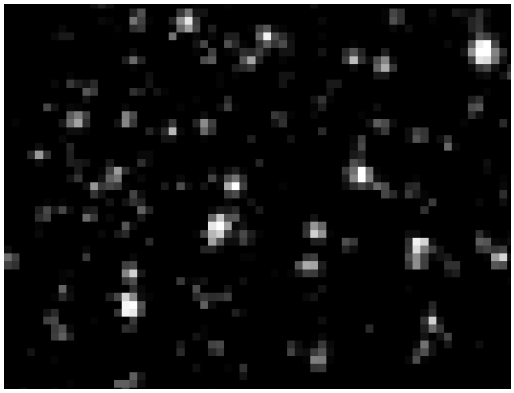

Figure 2.5. Sample particle images taken on two planes; (a) shows an image of one of the center planes; (b) is an image for one of the planes on the edge of the volume.

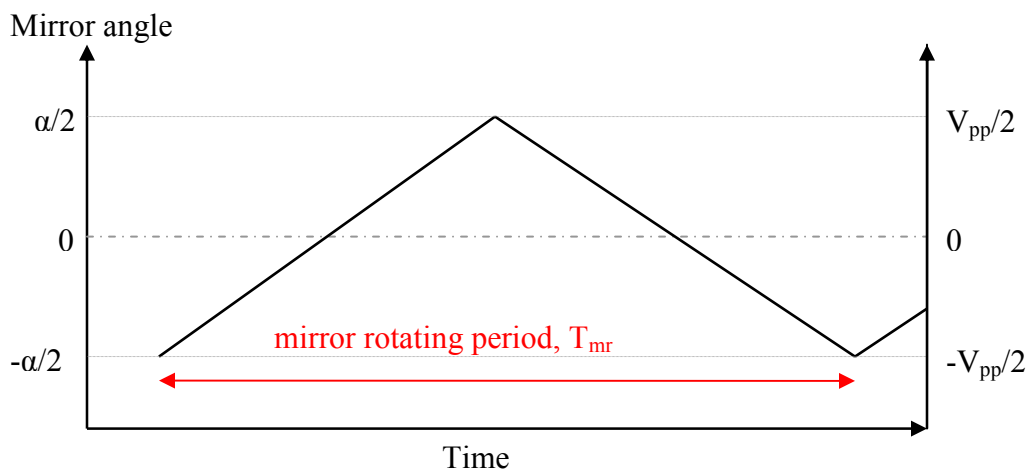

Figure 2.6. Diagram of the mirror angle position on time and voltage applied as a function of time. For a triangular wave of peak to peak voltage V_{pp}, the mirror angle varies from α/2 to –α/2. The relation between V_{pp} and α is established on Eq. 2.5 and Fig. 2.8.

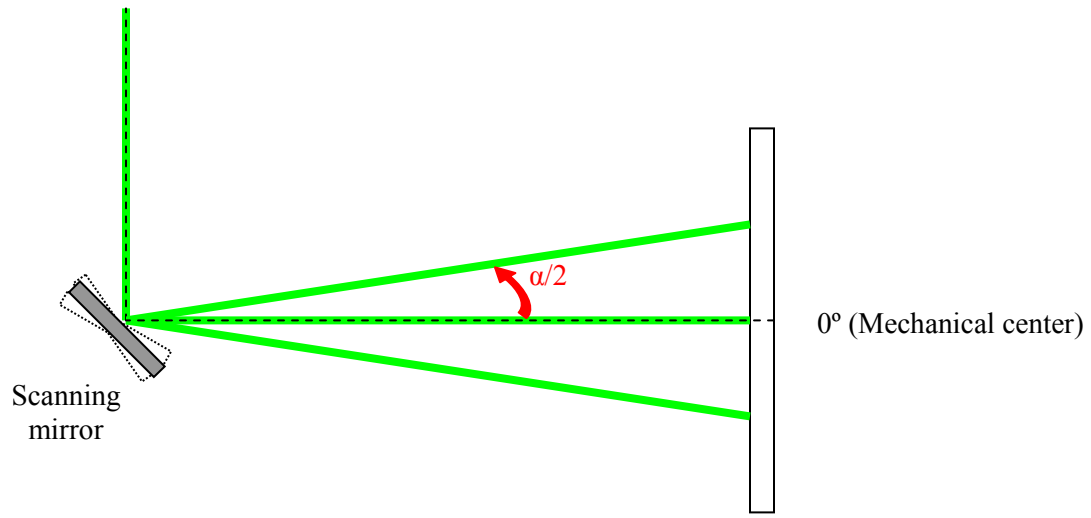

Figure 2.7 Experimental set up for the scanning mirror calibration.

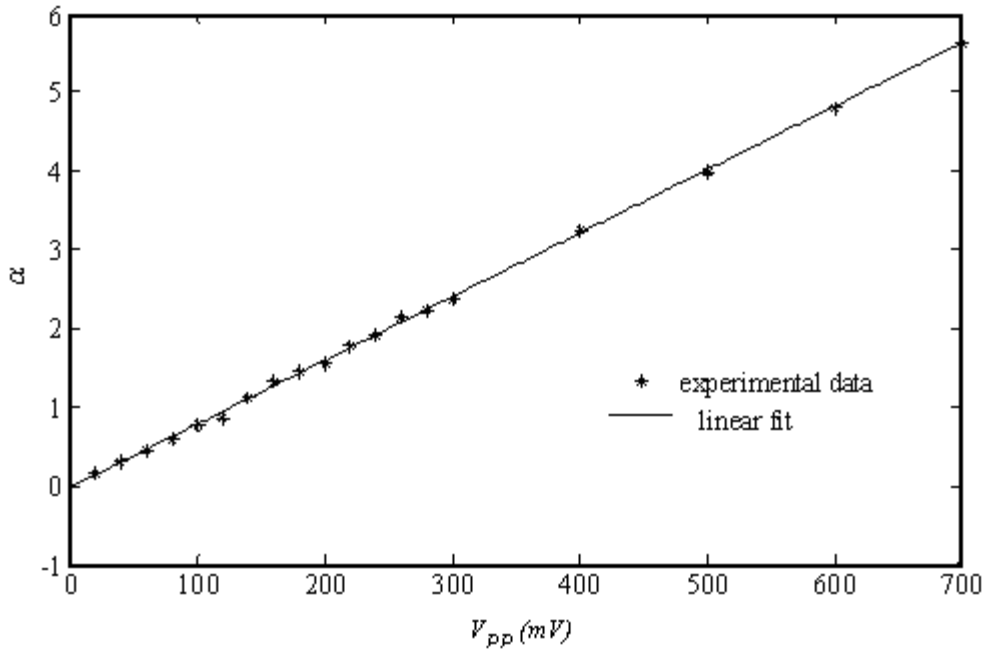

Figure 2.8. Scanning mirror calibration curve. Full scanning angle α (degrees) vs peak-to-peak voltage V_{pp} (mV) of the triangular wave.

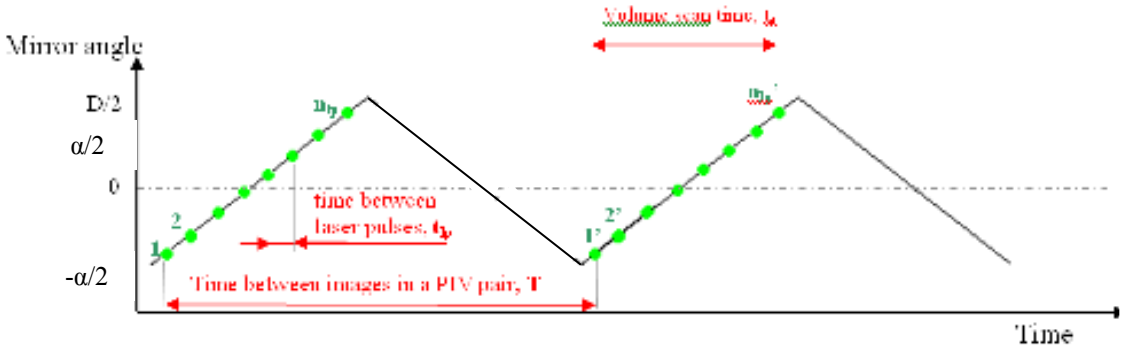

Figure 2.9. Diagram of the laser pulses synchronization with the scanning mirror angle. The triangular wave represents the mirror angle position on time. The laser pulses are represented as green dots. During a volumetric scan period, n_{lp} laser pulses hit the mirror in the corresponding angle position and time. The timing between laser pulses is constant, t_{lp}. Images taken in the same plane position, for two consecutive scanned volumes, are paired to form a PIV pair. The timing between the images in the PIV pair corresponds to T ($=T_{mr}$).

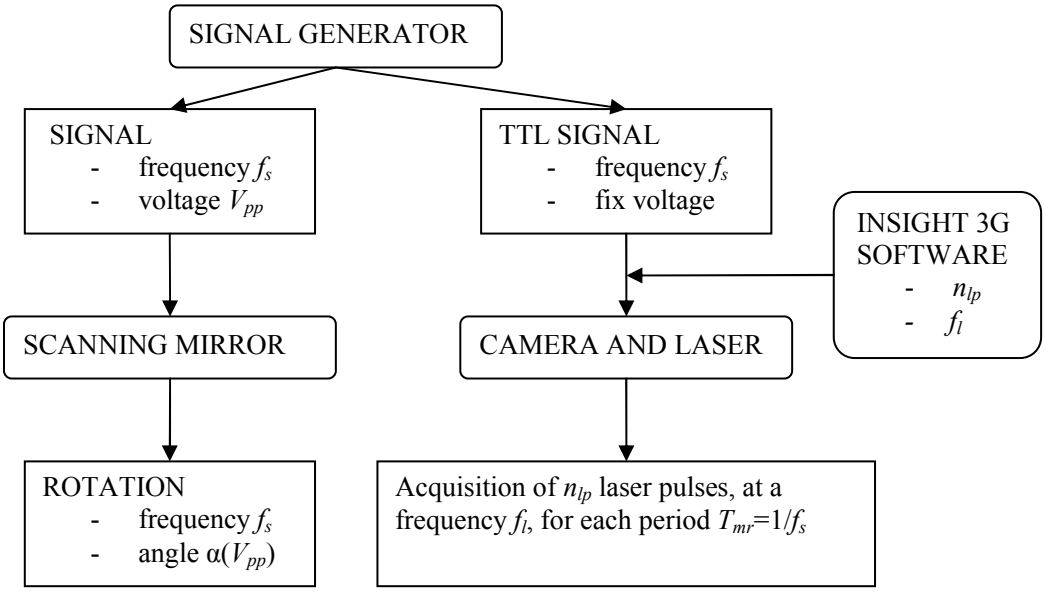

Figure 2.10 Scheme of the synchronization process.

CHAPTER III

Minimum Spacing Between Scanning Planes and Other Limitations of the TR SPIV System

The objective of the analysis of the PIV images is to resolve the fluid motion within a finite volume. This is achieved by the volumetric reconstruction of the velocity fields measured in a series of approximately parallel planes in which the volume is divided. Each plane corresponds to the flow region illuminated by a laser sheet in one laser pulse. The thickness of the laser sheet is small and proportional to the Taylor inner length scale. The light intensity distribution can be considered uniform along the plane of propagation of the laser sheet within the test section, as discussed in Section 2.2. However, the light distribution across the thickness of the laser sheet is approximately Gaussian and, therefore, the thickness of the laser sheet is not clearly defined.

The main objective of this section is to define the criteria for determining the thickness of the laser sheet and for determining the appropriate spacing between scanning planes for the TR SPIV system. The process involves measuring the distribution of particles across the laser sheet thickness observed by the camera. This will help define the concept of an

"effective thickness". This will relate the portion of the Gaussian intensity profile across the laser sheet that can be disregarded when considering the width of the laser sheet.

3.1 "Effective thickness" concept

The definition of the "effective thickness" of the laser sheet plays a vital role in the present scanning PIV system for the following three main reasons:

1. *PIV accuracy*

   The images taken in the same plane at different times are compared using a cross-correlation algorithm. In PIV measurements it is desirable to keep the laser sheet thickness as thin as possible, since it determines the uncertainty of the position of the velocity vector [5]. On the other hand, the minimum thickness depends on the minimum possible size of the interrogation windows, the seeding density and the maximum velocity allowed on the out of plane coordinate.

2. *Fully resolving the scanned volume*

   When scanning a volume, the "effective thickness" determines the spacing between plane measurements. If a portion of the fluid between two consecutive scanned planes is not illuminated by the laser sheet, it is possible that some important information about the fluid motion will be lost during the measurement, and therefore the reconstruction of the volume would not be fully resolved.

3. *Overlapping of the planes*

   If some part of two consecutive planes overlaps, the same spatial portion of the fluid would be analyzed in both of them. Consequently, the velocity measurements taken in both slices would be not independent. This can be a problem for cases where the thickness of the laser sheet is smaller than the smallest scales of the flow. If the thickness is estimated to be smaller than its real size, it can be erroneously considered that the measurements taken at the different planes are independent.

Therefore, it is necessary to know precisely the "effective thickness" of the laser sheet to determine the accuracy of the system and to make sure that consecutive planes are close enough, so that no region of the fluid is missing in the analysis; and far enough to achieve the maximum measurement volume, avoiding unnecessary overlapping of scanning planes.

The definition of the "effective thickness" is based on the technique used to measure the flow velocity. The measurements obtained with PIV depend directly on the tracers illuminated by the laser light. Thus, the proposed definition for the "effective thickness" of the laser sheet is "*the out of plane width of the quasi-planar section of fluid where the particles are illuminated with the laser sheet, and where the scattered light of the particles is detected by the CMOS sensor of the camera, and that affects significantly on the result of the PIV vector field.* The term "*affects significantly"* refers to the fact that at

least 95% of the particles that are paired in the process of obtaining the PIV vector should be contained inside the zone that represent the "effective thickness" value.

The amount of light that reaches the CMOS sensor of the camera depends on the shutter aperture of the camera lens. Particles located in the laser sheet, observed by the camera with a specific shutter aperture, might not be observed when using a smaller shutter aperture. Therefore, it is reasonable to think that the shutter aperture, as well as other possible particle imaging effects, can affect the "effective thickness" of the laser sheet. In order to minimize these effects, the same shutter aperture, laser intensity, type of tracers, camera position and lens were used for all the experiments in this work.

3.2 Laser sheet characterization

3.2.1 Intensity distribution across the laser sheet

Dr. Mullin[2] determined the thickness of the laser sheet based on the light intensity distribution across it. The light intensity profile was measured in the center of the field-of-view by traversing a knife edge across the sheet and collecting the transmitted light onto a photodiode detector. To quantify the thickness, an error function fit was determined from a nonlinear least-squares match to the measured profile, and then differentiated to obtain the resulting sheet-normal Gaussian intensity profile. The three lowest-order moments computed from this Gaussian profile result on the centerline position, the local intensity maximum, and the local $1/e^2$ thickness, which was used as the parameter to define the light sheet width.

The laser sheet intensity profile for the present study was measured using the same technique used by Dr Mullin[2]. The experimental set up used for this purpose is shown in Fig. 3.1a. The position of the laser and sheet-forming lenses was described in Chapter II. The scanning mirror angle was fixed at its mechanical zero position, reflecting the incident light at a 90 degree angle. A knife edge was positioned at the waist of the laser sheet, vertically parallel to it. The knife edge was mounted on a micrometer traversing stage to allow small displacements of the knife across the sheet, as illustrated in Fig. 3.1b. A power meter was placed after the knife edge, facing the incident beam. To avoid laser light reflections from the power meter, some of the incident light was blocked after the knife edge with a diaphragm, as shown in Fig. 3.1c. The knife edge was moved across the laser sheet in increments of 0.051 mm (0.002 inches). For each position of the knife edge, intensity values of the light reaching the power meter were recorded.

The curve obtained for the light intensity incident on the power meter is shown in Fig. 3.2a. The derivative of the obtained curve with respect to the spatial increment was taken, and the result approximated with a Gaussian fit to obtain the intensity profile. The resulting intensity profile measured at the effective focal length f is presented in Fig. 3.2b. This shows that the intensity profile across the laser sheet is almost Gaussian. The value of the second order moment $1/e^2$ is 2.07 mm.

The intensity profile was also measured at different positions before and after the effective focal point ($f \pm 50$ mm, f+100 mm, f+150 mm, f+200 mm, f+250 mm and f+300 mm) as shown in Fig. 3.3. Figure 3.3a represents the approximated Gaussian intensity

profiles obtained at different distances from the effective focal length. As expected, the area under the intensity distribution is higher for positions closer to the light source. This is caused by the diverging shape of the laser sheet created with a cylindrical lens. The normalization of the curves by its area underneath allows the comparison of the light intensity distributions at different locations. The normalized distributions are represented in Fig. 3.3b. The normalized profiles don't vary from f-50 mm < x < f+50, where $x=f$ represents the distance from the last focusing spherical lens (L_2) to the focal point of the beam. This shows that the waist thickness is constant in that region.

3.2.2 Particle distribution across the laser sheet

a. Measurement of the particle distribution with a knife edge

In PIV measurements it is customary to define the laser sheet thickness by using the $1/e^2$ value from the Gaussian intensity distribution across the laser sheet. Unfortunately, this value does not directly relate to the particle seeding concentration and its effect on the PIV accuracy. In the other hand, the previously defined "effective thickness" does. Therefore, it is proposed to use the "effective thickness" for characterizing the laser sheet. The distribution of particles that reflect the laser light, and are detected by the camera ("detected particles") is measured instead of the laser intensity.

To measure the "detected particle" distribution across the laser sheet, a knife edge displaced across the laser sheet was used. Fig. 3.4 represents the experimental set up used for this purpose. This set up is similar to the one used to measure the intensity profile described Section 3.2.1. The knife edge was positioned vertically parallel to the laser

sheet, 50 mm ahead the location of the waist (*f*-50), and traversed across the waist in increments of 0.051 mm. A water tank, seeded with the tracer particles, was positioned right after the knife edge. The tank wall was perpendicular to the incident beam when the scanning mirror was at the mechanical zero position. The High Speed camera was placed perpendicular to the laser sheet at its waist.

Two independent sets of 20 PIV images each were taken for the different positions of the traversing knife edge. A stirrer was installed inside the tank to ensure that each image is statistically uncorrelated from each other. The images were processed with a DIPA (Direct Image Particle Analysis) processor to count the amount of particles detected by the CMOS camera in each image. This application, part of Insight 3G software, distinguishes particles from the background noise, identifying as particles any group of 2 to 30 connected pixels with an intensity higher than a specific threshold value. The average particle size on the images was about 3-4 pixels.

Unfortunately, the results obtained using this method were not accurate enough to obtain the "detected particle" distribution. This is attributed to the background light detected by the CMOS sensor in the camera. For different positions of the knife edge across the laser sheet, the background light seen by the camera changed significantly. To correct this, an appropriate threshold value for the background noise on the DIPA processor was needed. But this threshold value changes for different background intensities, which requires manual modification by the user. Furthermore, for high threshold values, some of the particles are not recognized by the processor; and at low threshold values, some of the background noise is recognized as particles. And these effects are accentuated at the

edges of the laser sheet. Therefore, it becomes impossible to choose a threshold value that allows accurate recognition of the particles independently of the amount of background light.

b. Measurement of the particle distribution with a thin rectangular slit

To avoid the problem associated with the background noise mentioned above, a different measurement technique for the characterization of the distribution of light scattering particles across the light sheet is proposed.

Two knife edges were positioned and glued in front of each other, creating a thin, almost straight gap between them, with an approximate aperture of 0.18 mm. The thin straight slit formed between the knife edges was used to measure the "detected particle" distribution across the laser sheet. The experimental setup used is shown in Fig. 3.5. The setup is identical to the one described in Fig 3.4, with the knife edge replaced by the thin straight slit. The slit was positioned on the transition stage, vertically parallel to the light sheet. Two independent sets of 20 PIV images each were taken for different positions of the gap, which was traversed across the laser sheet in increments of 0.002 inches. By using this configuration, the background noise was more similar between the different sets of images.

Measurement of the light intensity that passes through the slit was also taken for the different traverse positions of the slit using the power meter. Two independent sets of measurements of the intensity were taken.

The size and uniformity of the slit was measured using a digital camera with a macro lens. The image resolution was approximately 0.19 μm/pixel. From the digital images of the slit it was observed that the knife edges were not exactly parallel; with the slit size varying from 167 to 198 micrometers. The main sources of error in this measurement were: (1) the orientation of the camera respect to the calibration target and to the knife edges gap, and (2) the positioning accuracy of the calibration target at the same distance from the camera than the knife edge-gap.

The thermal effect of the laser sheet on the knife edges gap was investigated. The knife edge temperature was measured with a thermocouple and it varied from 22 to 90 ºC during the experiment. Images of the slit were taken at different metal temperatures and compared, with no apparent change in size. This shows that the dilatation effects are negligible, and that the slit size did not vary significantly for the experimental conditions studied.

In order to obtain the distribution of the "detected particles" across the laser sheet (from the data obtained directly with DIPA), the relation between the knife edge gap size and the knife edge traverse step increment needs to be considered. The following method is proposed to understand this relationship.

Define the non dimensional parameter N, as a number that relates the size of the slit (s) with the magnitude of the displacement of the slit across the laser sheet between consecutive measurements (dz), as:

$$N = \frac{s}{dz}. \tag{3.1}$$

According to the slit size measured with the digital camera, and due to the non uniformity of the gap, N for our experiments should be a number between 3.3 and 3.9.

Define Po_i as the average number of particles counted with the DIPA processor for each position of the slit; where i is an index related to the slit position. The first measurement taken, with no light going through the slit, would correspond to the index i=0. The position z=0 is defined as the position of the edge of the slit which is further form the laser light, corresponding to the measurement identified with i=0. This is illustrated in Fig. 3.6. According to this notation, the position of the slit respect to the initial position can be calculated multiplying the displacement increment dz by the corresponding index number. Note that Po_i is the number of particles that correspond to a volume illuminated at the test section with the portion of the laser sheet that is not blocked by the knife edge.

Define P_i as the number of illuminated particles that correspond to a differential volume with a thickness equal to the displacement increment dz. Then, P_i can be calculated as follows 3.2:

$$\mathrm{P_i} = \mathrm{P}o_i + \mathrm{P_{i\text{-}N}} - \mathrm{Po_{i\text{-}1}}. \tag{3.2}$$

The following aspects must be considered about Eq. 3.2:

- This is a recursive formula, which uses the preceding terms to calculate the next terms of the sequence. To solve it, it is required to choose a starting term and repeatedly apply the same process to calculate the following terms. As a starting point, Po_0 was used.

- Po_0 corresponds to the measurement taken when there is not light going through the slit, and therefore Po_0=0. Consequently, the number of particles Po_i is also zero for negative indexes.
- Due to the recursive nature of this formula, any uncertainty and/or error in step measurements accumulates as further terms of the series are calculated.
- The slit size, N, is not known accurately since the gap is not straight and the measurement technique involves experimental errors. The computation of the Po_i terms requires an initial estimation of the slit size, and a trial and error process to calculate the optimal N, N_{opt}. The best estimation of the relation between the slit size and the displacement increments, N_{opt}, will be the one that gives a Po_i distribution more symmetric when calculated with the Eq. 3.2.
- Since N will not be necessarily an integer, the P_{i-N} terms in Eq. 3.2 need to be calculated through linear interpolation.

Figure 3.7a shows the average number of particles counted with the DIPA processor for the different positions of the slit. Eq. 3.2 was applied to the data in Fig. 3.7a, and the most symmetric profiles are obtained for N_{opt}=3.7, as shown in Fig. 3.7b.

The same N_{opt} was obtained for both independent sets of data taken. Both "detected particle" distributions obtained were approximated with a Gaussian fit and showed good agreement, as shown in Fig. 3.8. The peak of the Gaussian fit in each case was used for the normalization of the curves. The y- coordinate on the distributions on Fig. 3.8 represents the fraction of particles that were detected at a given z- location, compared

with the maximum number of particles that the camera could detect (at the center of the laser sheet). After normalization, both distribution plots are averaged and the final particle distribution is obtained.

c. Validation of the results

To check the accuracy of the results for the measurement of the particle distribution, the following validation methods are applied:

- *Application of the recursive formula on reverse order.* Equation 3.2 was also applied to the *Po* data in reverse order, by changing the notation accordingly. The profiles obtained were almost identical, with the same N_{opt}.

- *Measurement of the intensity distribution across the laser sheet.* The same recursive formula can be applied to obtain the power distribution instead of the particle distribution across the laser sheet if the power is measured using the same slit and the same displacement increments dz. N_{opt} should be the same for both applications, independently of the shape of the profiles. The intensity profile should be Gaussian-like, as obtained with previous measurements. Experiments to measure the power distribution with the slit were performed, and good agreement with previous measurements was observed. The best fit was given by N_{opt}=3.7, as shown in Fig. 3.9.

- *Comparison with the direct measurement of the laser beam intensity.* The results obtained from the power measurements and Eq. 3.2, with N=3.7, represent the distribution of the beam intensity across the laser sheet. Therefore, the area under the

curve should provide the total power of the laser beam. These numbers were calculated for two independent experiments, and compared to the direct reading, with an error in the calculated total power of less than 0.5%.

- *Total beam intensity measured at slit size intervals.* The size of the dual knife edge gap was determined to be 3.7 times bigger than the traverse step size increment across the laser sheet. Therefore, the total light intensity incident on the power meter can be calculated by the sum of the values of the intensity data points separated a distance equal to N_{opt} times the step size, and compared with the direct reading of the beam intensity. The numbers match with an error smaller than the 1% for N_{opt}=3.7.

3.3 Inner and outer scaling laws for jets

One of the main objectives of this work is to characterize the small scales of the flow in a turbulent jet. To observe the small scales of the flow, the measuring volume that will be scanned with the TR SPIV needs to be estimated. The size of the control volume must allow measurements at such scale, but also being consistent with the available resolution of the TR SPIV. This puts some limitations on the type of flows this system can measure.

The theory of the energy cascade for turbulent flows states that the energy is transferred from large scale eddies to smaller ones, until is dissipated by viscous effects [1]. According to this theory, there is a range of length and time scales related to various factors of the energy cascade. Essential concepts associated with the scales relevant to the present study are reviewed next.

3.3.1 Time and length outer scales

The local outer length $\delta(x)$ and velocity $u_c(x)$ scales in turbulent shear flows, where x is the downstream distance from the jet source, characterize the local mean shear that drives the turbulence. For turbulent jets in free flow, the local outer velocity scale, $u_c(x)$, is the local centerline velocity; and the local outer length scale, $\delta(x)$, represents the full width over which the mean velocity profile drops 95% of its local peak value (centerline velocity). This is sketched in Fig. 3.10.

The values of the outer scales can be calculated using

$$\mathrm{u_c}(x) = 7.2 \cdot \left(\frac{J_0}{\rho}\right)^{1/2} \cdot x^{-1} \quad \text{and} \tag{3.3}$$

$$\delta(\mathrm{x}) = 0.36 \cdot x \quad . \tag{3.4}$$

Eqs. 3.3 and 3.4, has been obtained experimentally for non buoyant turbulent jets [22][23]; where ρ is the ambient fluid density, and J_0 is the momentum flux.

Since no buoyancy acts on the fluid, J_0 is constant at all downstream distances, and can be calculated for a source with exit area A_e, uniform exit velocity U_0 and uniform exit density ρ, as follows [23]:

$$\mathrm{J}_0 = \rho \cdot U_0^{\,2} \cdot A_e \,. \tag{3.5}$$

Aspects of the flow associated with the outer scales, such as the mean velocity and vorticity, are usually scaled by δ and u_c.

Other parameters related with the outer scales are τ_δ and Re_δ. The local outer time scale $\tau_\delta(x) = \delta(x)/u_c(x)$, represents the time that the structures of size δ require to advect past a fixed point at the local outer velocity $u_c(x)$. The local outer-scale Reynolds number is determined by $Re_\delta(x) = u_c(x)\cdot\delta(x)/\nu$.

3.3.2 Time and length inner scales

The Taylor and the Kolmogorov microscales refer to the smallest turbulent scales of the flow. The local Kolmogorov scale $\lambda_k(x)$ represents the size of the smallest scale eddies, where energy dissipates to heat by viscous dissipation. $\lambda_k(x)$ depends only on the viscosity and dissipation rates ν and $\varepsilon(x)$, respectively, and is defined by Eq. 3.6. The local mean dissipation rate for turbulent jets can be calculated from the local outer scales, according to Eq. 3.7. The Kolmogorov time scale is given by Eq. 3.8 [24] [25].

$$\lambda_k(x) = \left(\frac{\nu^3}{\varepsilon(x)}\right)^{1/4} \tag{3.6}$$

$$\varepsilon(x) = 0.08\frac{u_c(x)^3}{\delta(x)} \tag{3.7}$$

$$\tau_k(x) = (\nu/\varepsilon)^{1/2} \tag{3.8}$$

The characteristic local inner scale of the flow, or Taylor scale $\lambda_\nu(x)$, is defined as the distance over which the velocity gradients within a fine scale structure decrease 20% from their peak value. It is also called dissipation scale, and corresponds to the *average* dimension of the eddies that are mainly responsible for dissipation. The Taylor scale and the Kolmogorov scales are proportional, and for turbulent jets, the constant has been experimentally measured to be 5.9 [26] .The inner Taylor time scale, corresponding to the

Lagrangian time scale on which the Taylor inner scales of the flow evolve, is given by Eq. 3.10 [2].

$$\lambda_{\upsilon}(x) \approx 5.9 \cdot \lambda_k(x) \tag{3.9}$$

$$\tau_\nu(x) = \lambda_\nu(x)^2/\nu \tag{3.10}$$

All inner-scale quantities scale with ν and $\lambda_\nu(x)$, as they are the only relevant physical parameters at the inner scales of the flow. Since the gradient fields in turbulent flows are concentrated into inner-scale structures by the strain-diffusion effects, they must scale by the local inner variables. Velocity is also normalized by these parameters in the present work.

3.3.3 Quasi-universality on inner scales

According to Kolmogorov's classical turbulence theory, the structure, statistics and scaling of the velocity gradient fields at the intermediate and small scales of all turbulent flows, viewed on the inner length and time scales λ_ν and τ_ν, should be identical for local outer-scale Reynolds numbers large enough for a sufficient local inner to outer length scale separation ($(\delta/\lambda_\nu) \sim Re_\delta^{3/4}$). In particular, the gradient fields scaled on the inner variables ν and τ_ν should be independent of Re_δ, the outer scale variables, and the particular shear flow studied [2].

3.4 Spacing between scanning planes

This section explains several aspects that have to be considered on the estimation of the appropriate spacing between scanning planes. These considerations are related to the PIV

nature of the measurements, the characteristics of the turbulent micro-scales of the flow, and the distribution of detected particles across the laser sheet.

3.4.1. Principle of Particle Image Velocimetry

The basic features of the measurement technique used in the present study, PIV, are described briefly as follows. Tracer particles that follow the local fluid motion (see Section 2.2) are added to the flow and illuminated in a plane of the flow twice within a short time interval. The light scattered by the particles is recorded on two separate frames on a camera sensor, and stored as a digital double exposure PIV image. For evaluation of the PIV, recording images are divided in small subareas called “interrogation windows”. Typical sizes of interrogation windows range from 16x16 pixels up to 128x128 pixels depending on the flow and seeding conditions. The local displacement vector for the images of the tracer particles of both images is determined by a statistical cross-correlation method for each interrogation window. The projection of the vector of the local flow velocity into the plane of the light sheet (2 component velocity vector) is calculated taking into account the time delay between the two illuminations and the magnification of the images. The process is repeated for all interrogation areas of the PIV recording to obtain the velocity vector field at the measurement plane.

It is assumed that the particles within one interrogation area move homogeneously between the two frames. The particle image pattern in one interrogation area of the first frame is shifted to a different position on the second frame; and the spatial displacement that produces the maximum cross-correlation (the best match) statistically approximates

the average displacement of the particles in the interrogation area. In the standard Fast Fourier Transform FFT algorithm, the two-dimensional FFT of each interrogation area is calculated. The multiplication of the first interrogation area FFT and the second interrogation area FFT conjugate is computed. The modulus of the 2D FFT of the multiplication creates the correlation plane, where the location of the maximum value in the correlation plane determines the particle displacement [5].

The images of the tracer particles that are illuminated by the laser sheet in both laser pulses, and therefore, remain visible in both frames of the PIV image, are defined as "particle image pairs". According to the PIV principles above, the maximum peak in the cross-correlation is attributed to the "particle image pairs".

3.4.2 Minimum number of particle image pairs

The number of particle image pairs captured in an interrogation area depends on three factors as following:

$$N = N_I \cdot F_I \cdot F_o, \tag{3.12}$$

where N_I is the effective particle image density within the interrogation spot (where "*effective*" stands for particles *detected by the camera*), F_I is a factor expressing the in-plane loss of pairs, and F_0 a factor expressing the out-of-plane loss of pairs (percent of particles that remain illuminated by the sheet). The product of the three quantities yields the mean effective number of particle image pairs in the interrogation spot [5].

Nowadays, it is common to offset the interrogation windows when using any PIV correlation, which minimizes the in-plane loss of pairs, that is, $F_I \rightarrow 1$.

In practice, the data yield can be easily optimized by ensuring the presence of at least three or four particle image pairs [27]. Hence, the number of particle image pairs has to be $N \geq 4$.

Common values for effective particle density (N_I) used for PIV are in the range of 6 to 20 particles per interrogation area. Although N_I depends on experimental characteristics, it can be controlled with the amount of tracers added to the flow, light intensity and particle imaging. Notice that the size of the interrogation area is also a variable to be decided for the experimentalist, depending on the size of the flow scales to be measured.

Therefore, the percentage of particles that need to remain illuminated by the laser sheet (F_o) in order to be paired to obtain the PIV vector, in terms of the effective particle density, is

$$F_0 = \frac{N}{N_I} = \frac{4}{N_I}. \tag{3.13}$$

3.4.3 Maximum velocity across the laser sheet

As explained above, the loss of particles between PIV images is related to the out of plane displacement of the tracers. Therefore, the effective particle density N_I can be associated with the velocity component of the flow across the laser sheet. The "detected

particle" distribution across the light sheet, represented in Fig. 3.11a as $P(z)$, and a set of considerations detailed below, are used to establish that relation.

To get a velocity vector for an interrogation area, the position of particles at two different times, or frames, corresponding to Frame 1 and Frame 2, is compared. Let's consider that all the particles detected in one PIV interrogation area in Frame 1 move together with the same speed. In that case, the computation of the PIV vector for that interrogation area is based on displacement of the group of particles that are seen in both frames.

Since the laser sheet has some thickness, one interrogation area observed in Frame 1 corresponds to a volumetric portion of the fluid. From all the tracer particles that are contained in that volume, the camera only detects some of them, the ones sufficiently illuminated, as defined by the particle distribution curve across the laser sheet, $P_{1_{F1}}(z)=P(z)$ (blue line in Fig. 3.11b).

Let's define S as the displacement of the fluid portion across the laser sheet between frames. At the time corresponding to Frame 2, all the particles from the volumetric portion of fluid observed in Frame 1 move to a different location across the laser sheet. The particles that were detected in Frame 1 as $P_{1_{F1}}(z)$ correspond in Frame 2 to a particle distribution $P_{1_{F2}}(z)=P(z-S)$ (red line in Fig. 3.11b). But at Frame 2, the camera can only detect the particles corresponding to the area under the centered distribution curve $P_{2_{F2}}(z)=P(z)$. Therefore, the portion of the particles that were seen in Frame 1 and can be paired with the particles seen in Frame 2, corresponds to the overlap area of both

curves ($P_{1_{F1}} \cap P_{2_{F2}}$). Note that the physical position of the paired particles across the laser sheet depends on whether it is considered with regard to the time corresponding to Frame 1 or Frame 2, as illustrated in Fig. 3.11c-d.

Hence, it is possible to calculate the portion of particles detected in the interrogation area in Frame 1 that can be paired with the ones seen in Frame 2, as a function of the displacement of that interrogation area across the laser sheet. The maximum percentage of particles that, being detected by the camera in one frame of the PIV image, disappear in the other frame as a consequence of their displacement across the laser, can be formulated in terms of the maximum displacement S_{max} as

$$1-\frac{4}{N_I}=\frac{\int_{z_I}^{\infty}[P_{1_{F2}}(z)-P_{2_{F2}}(z)]dz}{\int_{-\infty}^{\infty}[P\,(z)]dz}=\frac{\int_{S_{\max}/2}^{\infty}[P(z-S_{\max})-P(z)]dz}{\int_{-\infty}^{\infty}[P(z)]dz}. \qquad (3.14)$$

In Eq. 3.14, z_I corresponds to the intersection point between $P_{1_{F2}}(z)$ and $P_{2_{F2}}(z)$, as shown in Fig. 3.11b. The term z_I is $S_{max}/2$ since the curve $P(z)$ is symmetric. This allows the computation of S_{max} for a known "detected particle" distribution and effective particle density per interrogation spot.

The maximum velocity of a particle group across the laser sheet between both frames of the PIV capture is given by

$$V_{\max}=\frac{S_{\max}}{dt}, \qquad (3.15)$$

where dt is the timing between Frame 1 and Frame 2. This is the time between the frames in a PIV pair.

3.4.4 Criteria to establish the maximum resolution of the system

Let's call PP_2 the particles graphically corresponding to the area under ($P_{1_{F1}} \cap P_{2_{F2}}$) (shaded area in Fig. 3.11b). Then, PP_2 is the distribution of the particles that, seen in Frame 2, can be paired between frames as they remain illuminated by the laser sheet. This corresponds to a particle displacement across the laser sheet between frames equal to S_{max}. According to the almost-Gaussian shape of the particle distribution, the ends of the curve that defines PP_2 tend to zero. Therefore, the particles corresponding to the edges of the laser sheet thickness affect less on the computation of the PIV vector, as only a small portion of them are detected by the camera on both frames. Let's define $PP_{2_{95\%}}$ as the centered portion of the distribution curve PP_2 which encloses the 95% of the area under it; and $\delta_{PP_{95\%}}$ the width of that distribution, as shown in Fig. 11c. Similarly, the zone illuminated by the laser sheet in Frame 1 that contains 95% of the particles paired on the PIV correlation is $PP_{1_{95\%}}$. This is the same than $PP_{2_{95\%}}$, but displaced a distance S_{max} across the laser sheet.

From the terms stated above, and with the local Taylor inner scale as a representation of the average size of the smaller scales of the flow on the control volume, the limitations of the system can be summarized as follows:

[1] Velocity of the flow perpendicular to the laser sheet $\leq V_{max}$

Where V_{max} is obtained from Eq. 3.15, and depends on the following:

- $S_{max,}$ which relates the effective particle density N_I, and calculated with Eq. 3.14.
- dt, which depends on the number of planes scanned and the minimum timing between laser pulses.

This ensures a minimum of 4 particle pairs in the PIV correlation.

[2] Effective thickness of the laser sheet = $\delta_{PP_{95\%}} + S_{max} = \delta_e$

For a volume of fluid of the size $\delta_e^{\,3}$, centered across the laser sheet, 95% of the detected particles (in either Frame 1 or Frame 2) are successfully paired in the PIV process if their velocity stays correlated to itself for a time larger than the timing between frames.

[3] Time between PIV frames: $dt \geq \tau_v$

This is a direct consequence of criteria [2], and ensures that the velocity of the group of particles stays correlated to itself between frames of the PIV process.

[4] Measurable Taylor scale of the flow: $\lambda_v \geq 2 \cdot \delta_e$

Applying a Nyquist sampling criteria, it is considered that a separation between planes half the size of the average micro-scale of the flow, λ_v, gives enough resolution to measure the velocity field without loss of relevant information between planes.

[5] Size of the interrogation windows $\leq 2 \cdot \delta_e$

According to the criteria in [4], a size of the interrogation window equal or smaller than half the size of the Taylor scale of the flow, fully characterize the in-plane fluid motion.

[6] Maximum time to complete a volume scanning $\leq \tau_v / 2$

Given that τ_v represents the time in which the small scales evolve, it is expected that no significant changes occur in the scanned volume for a time $\leq \tau_v / 2$.

3.5 Maximum resolution of the present study and flow chart of experimental design

The TR SPIV system described in Chapter II allows the variation of several experimental parameters in order to adapt the system to the flow measurement. The flow chart given in Fig. 3.12 shows the proposed guide line for the selection of parameters for the TR SPIV system to resolve the micro-scales of a flow.

According to the criterion described, the minimum spacing between scanning planes for the laser sheet created with the optic path defined in Chapter II is 2.12 mm (δ_e = 2.12 mm). Therefore, the proposed measurements were done in a control volume in a turbulent jet with $\lambda_v \geq 4.14$ mm.

a)

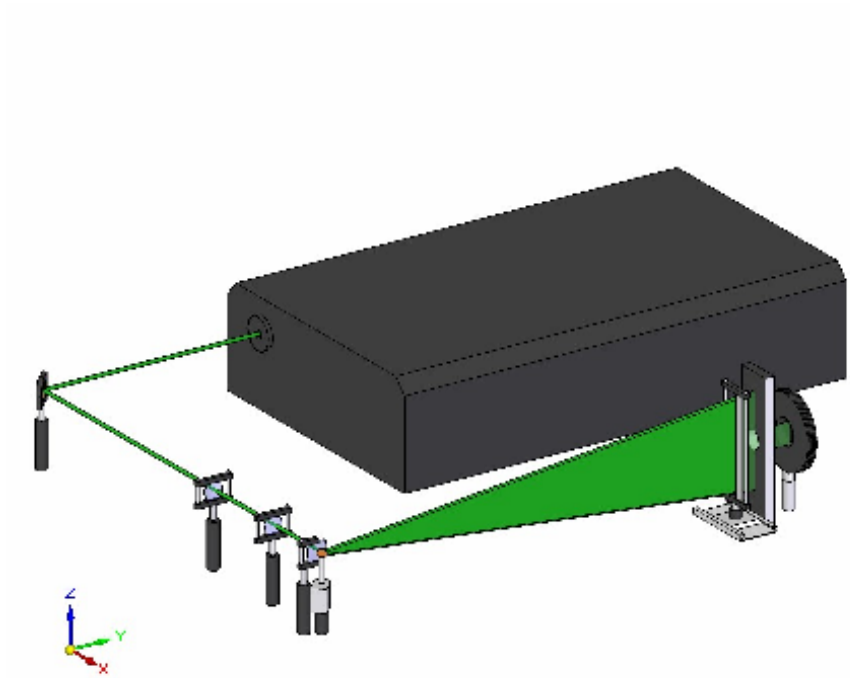

b)

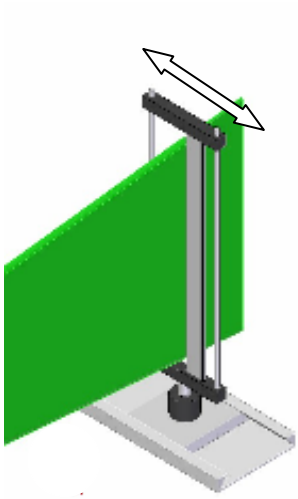

c)

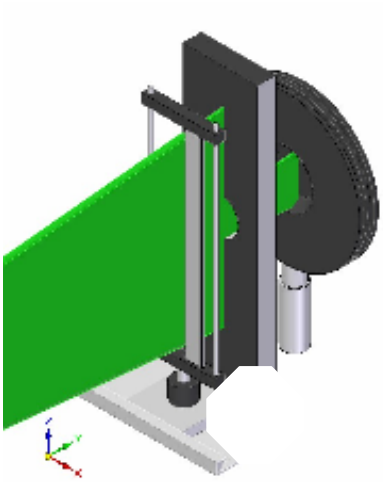

Figure 3.1. Sketch of the experimental set-up for the measurement of the power distribution across the light sheet using one knife edge; (b) close-up view of the knife edge on the transition stage; (c) close-up view, including the voltmeter and the diaphragm to block some of the laser light.

a)

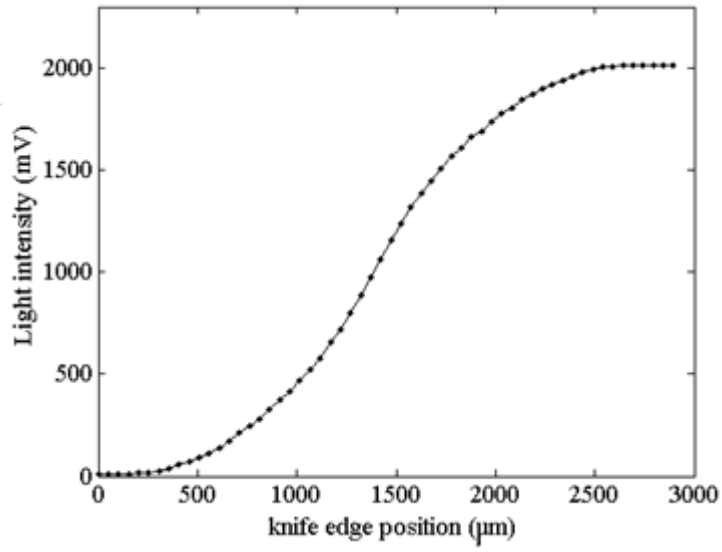

b)

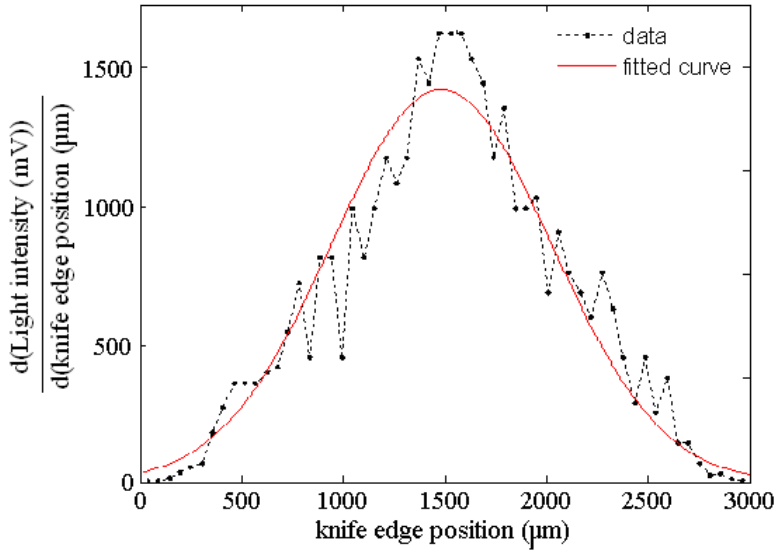

Figure 3.2. Intensity distribution across the laser sheet obtained using one knife edge; (a) plot corresponds to the raw measurement values; (b) results show the intensity profile calculated with the corresponding derivative and Gaussian fit.

a)

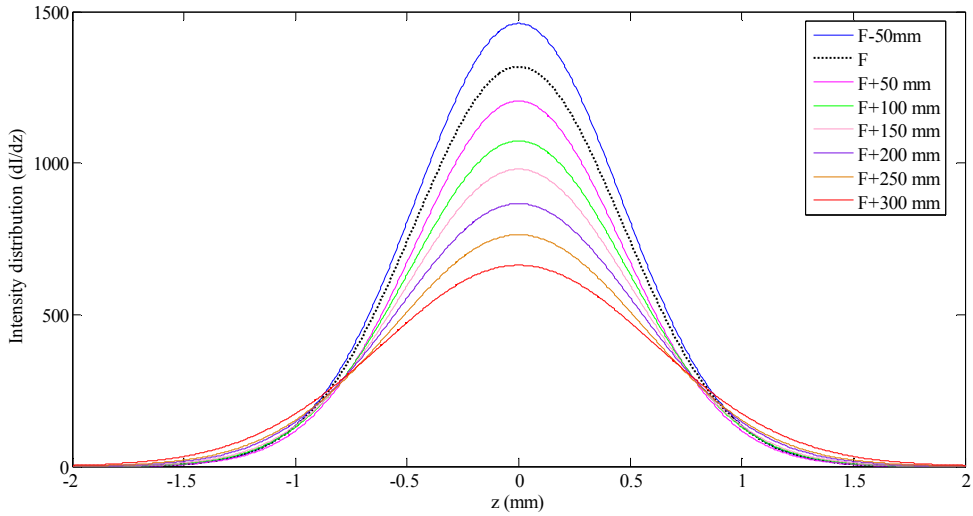

b)

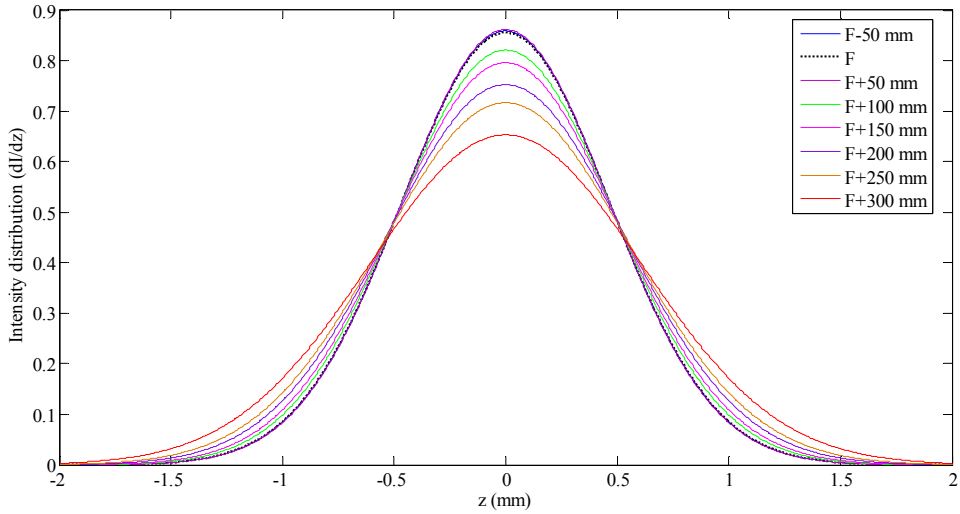

Figure 3.3. Intensity distribution across the laser sheet measured at different distances from the focal point of the laser sheet, showing (a) the Gaussian fit of the measured profiles, and (b) the same profiles normalized. The normalized intensity distributions match for the positions *f*, *f*-50 mm and *f*+50 mm.

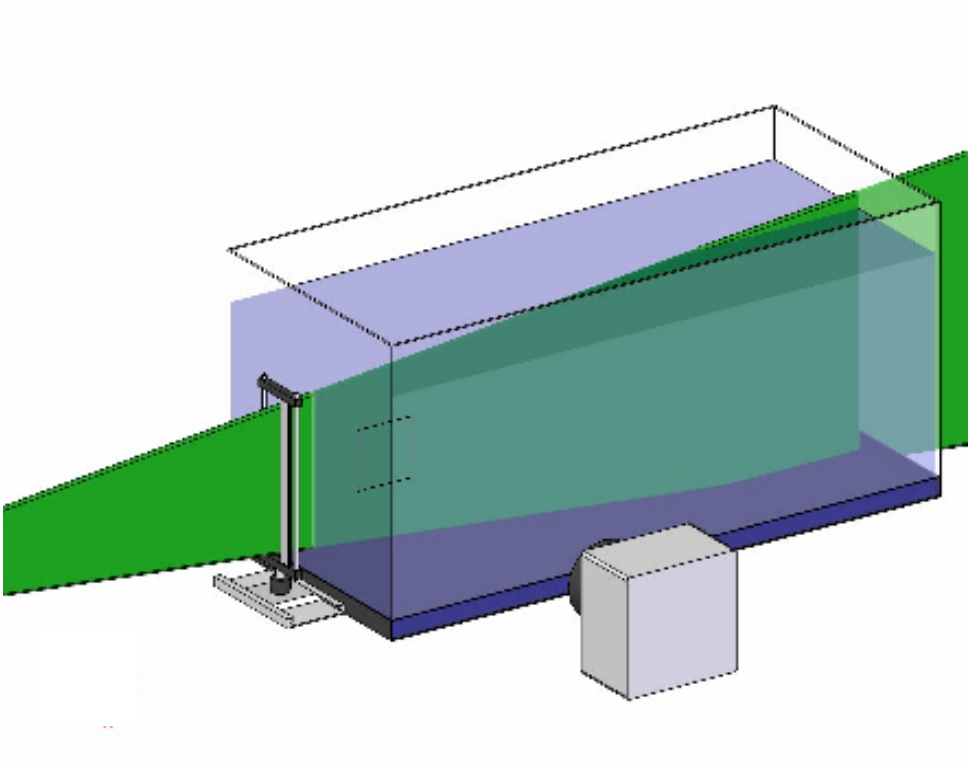

Figure 3.4. Experimental set-up for the measurement of the particle distribution across the laser sheet using one knife edge.

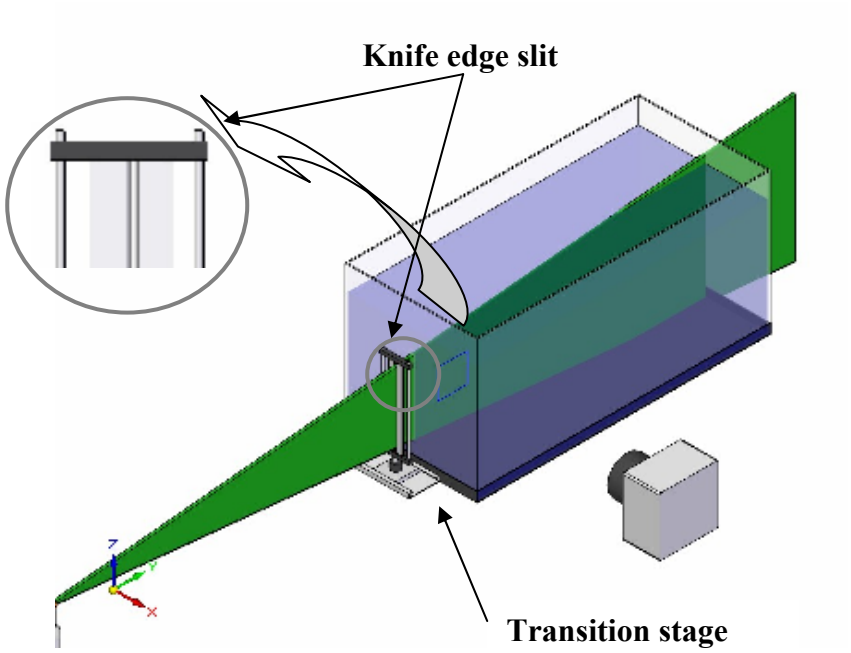

Figure 3.5. Experimental set up for the measurement of the particle distribution across the laser sheet using a straight gap. Insight figure shows the mounted dual knife edge with small gap.

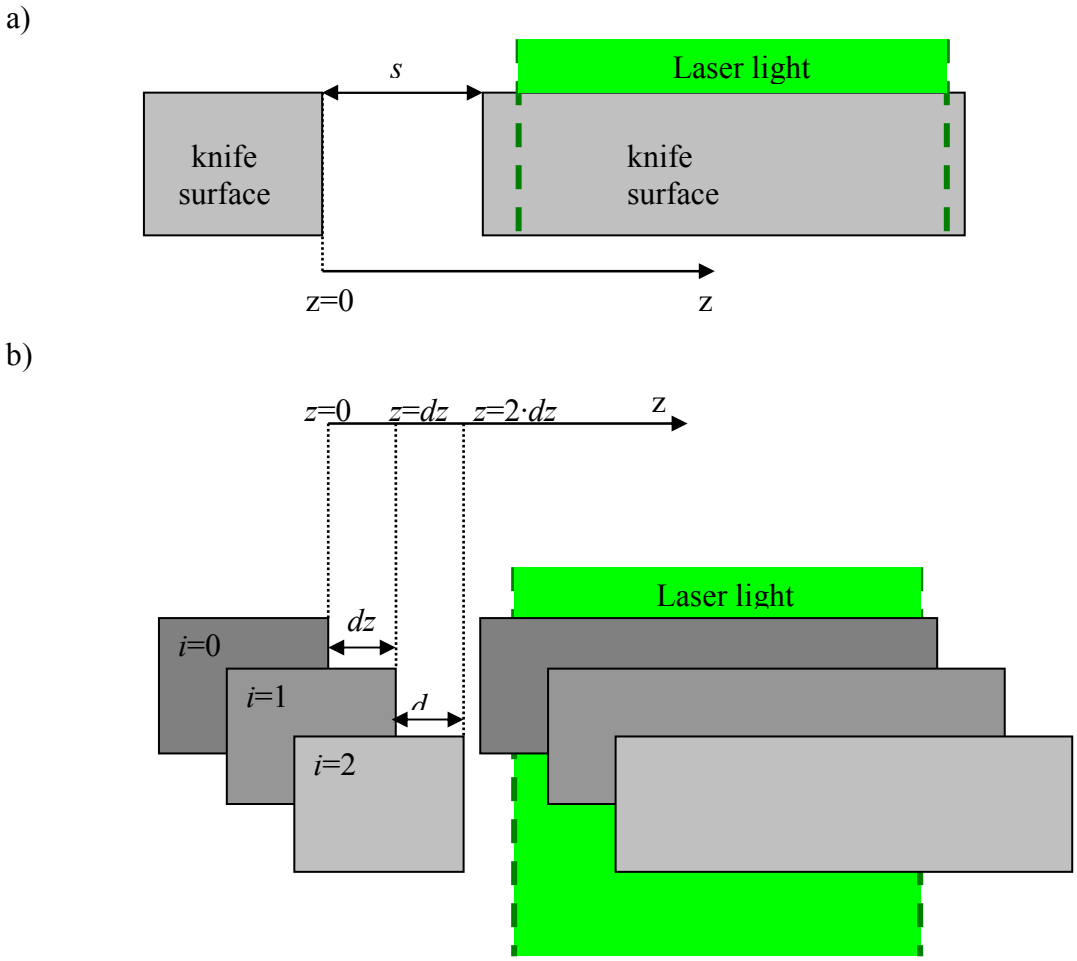

Figure 3.6. Illustration of the displacement of the knife edge gap across the light sheet, showing (a) the position of the knife edge for the first measurement, denoted with index i=0; and (b) the position of the slit for the first 3 measurements. z=0 corresponds to the position of the knife edge that is further from the laser sheet, when i=0. Note that the knife surface is blocking the laser light completely. The gap size is represented with s and dz represent the magnitude of the displacements in which the gap is displaced for consecutive measurements.

a)

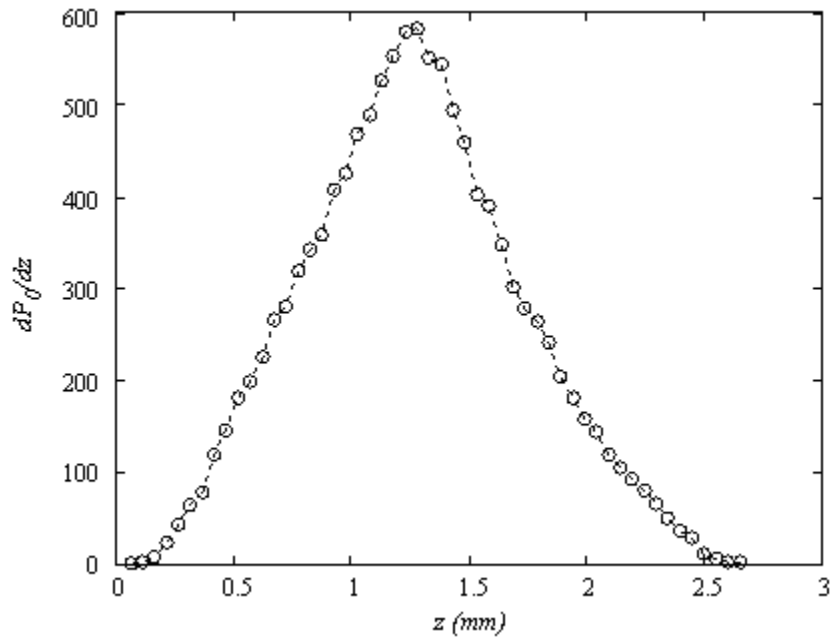

b)

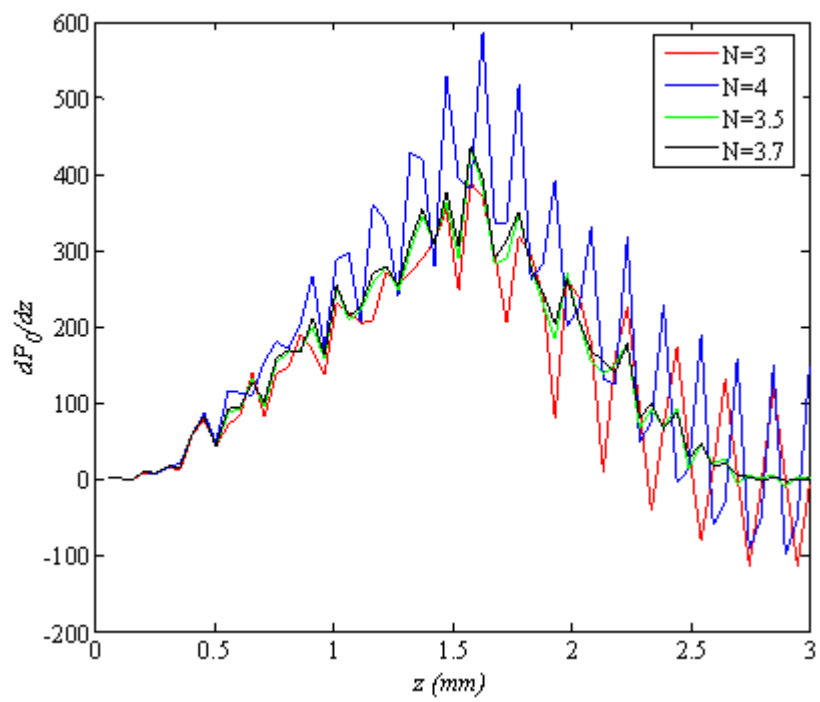

Figure 3.7. Calculation of the distribution of the particles that can be detected by the camera with respect to their position across the laser sheet, showing (a) the number of particles that are detected by the camera for different positions of the slit, and (b) the particle distribution, calculated with Eq. 3.2 for different N. The best fitting is for N_{opt}= 3.7.

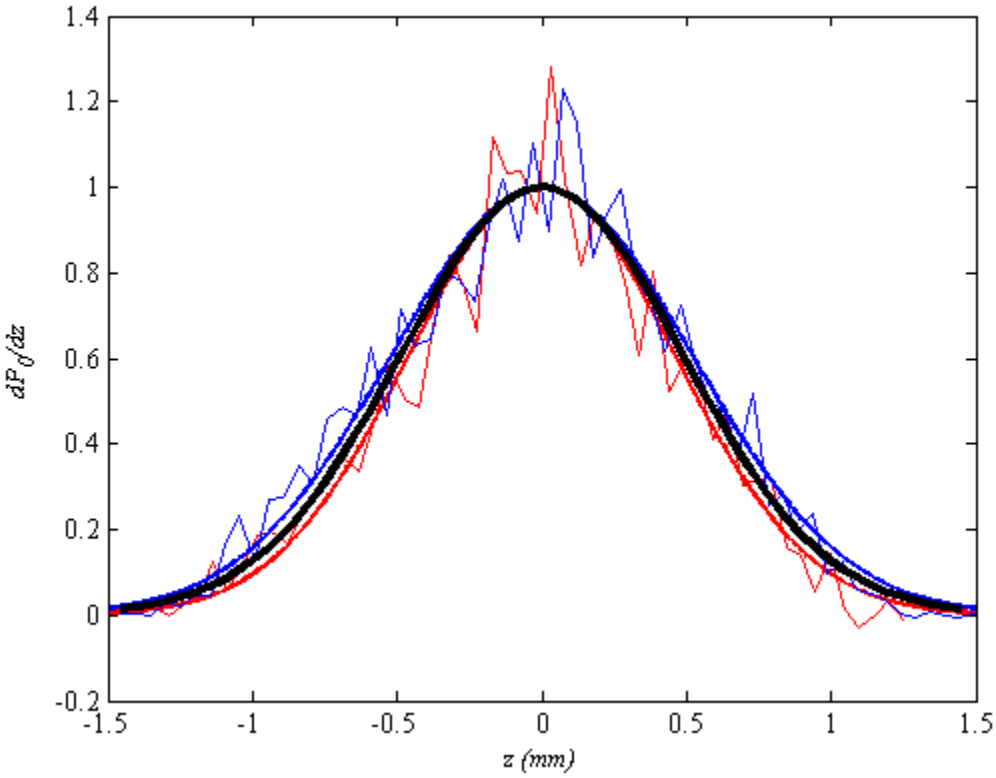

Figure 3.8. Representation of two independent measurements of the particle distribution across the laser sheet, obtained for N_{opt}=3.7. Curves were normalized by their peak value and centered, and fitted by Gaussian curves. The average of both distributions is the final particle distribution (in black). The *y*- axis is the percentage of particles that are seen at each *z*- location, out of the maximum amount of particles that can be seen in one location.

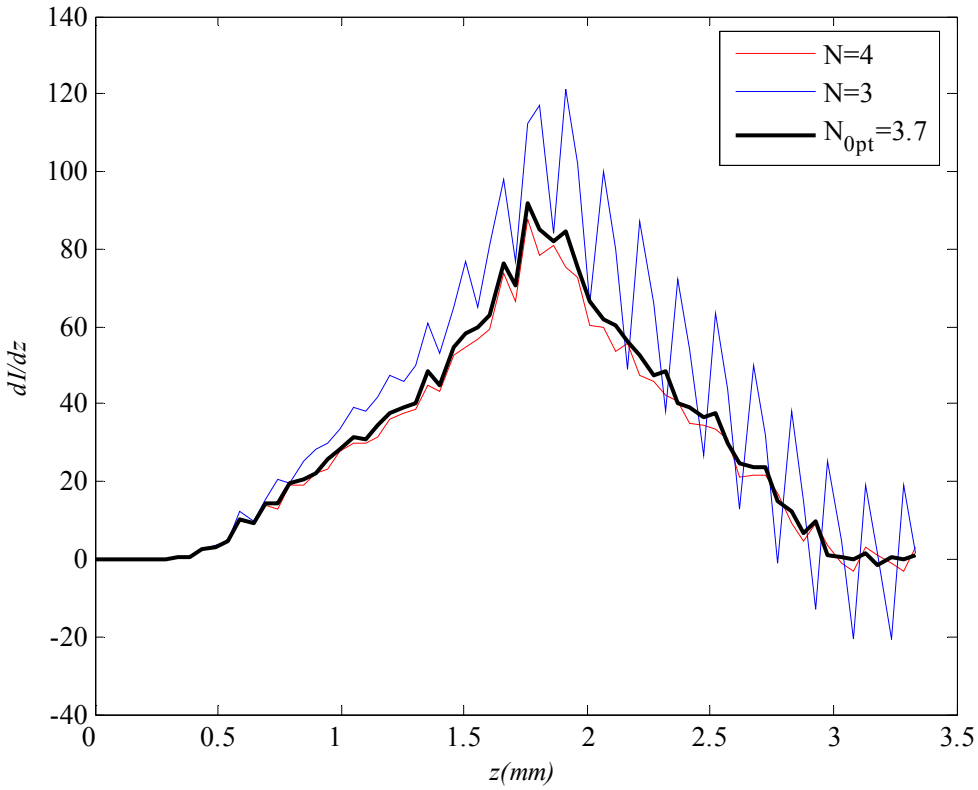

Figure 3.9. Laser power distribution obtained from the dual knife edge; N_{opt} was 3.7.

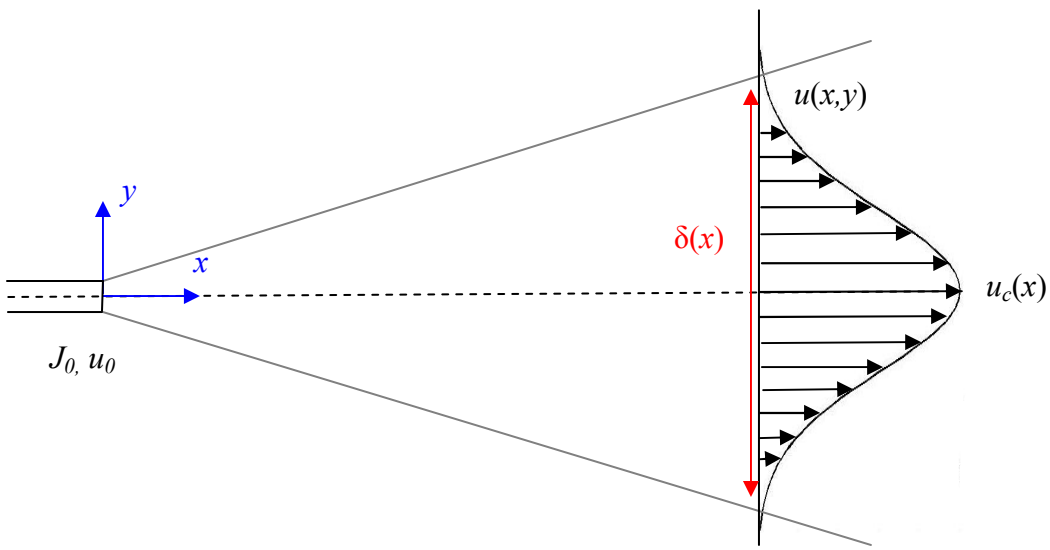

Figure 3.10 Representation of the main parameters (outer scales) for a jet in free flow.

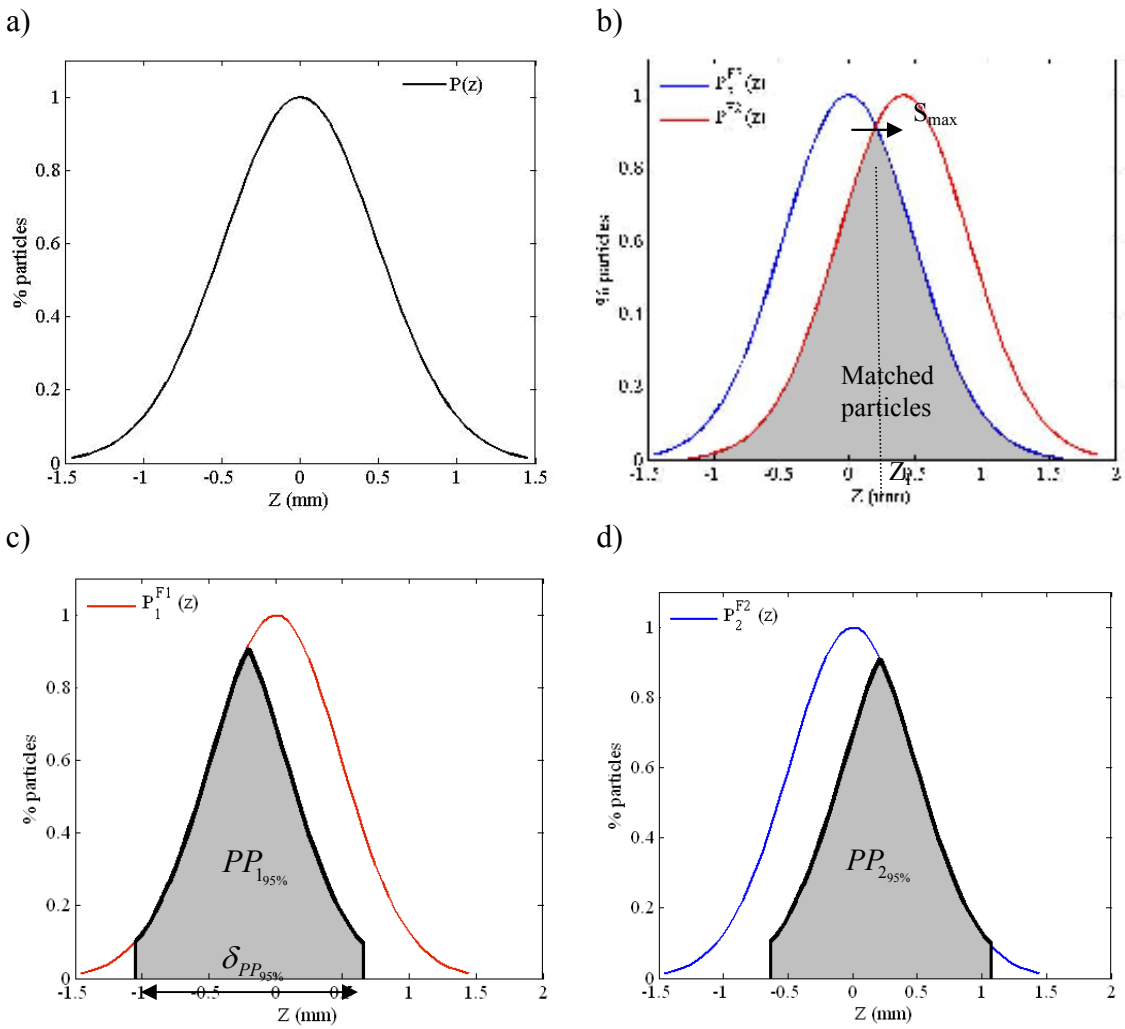

Figure 3.11. (a) Particle distribution across the laser sheet, $P(z)$; (b) on Frame 1, the camera detects a particle distribution $P_{1_{F1}}(z)=P(z)$, represented on blue. In Frame 2, the particles seen in Frame 1 move a distance S_{max} across the laser sheet, corresponding to the particle distribution $P_{1_{F2}}(z)=P(z-S_{max})$, represented in red. The particle distribution that the camera can detect in Frame 2 corresponds to $P_{1_{F1}}(z)=P(z)$. The particles that are seen in both frames correspond to the shaded area. (c): the shaded area corresponds to the 95% of the particles that, seen in Frame 1, can be paired with the ones in Frame 2, called $PP_{1_{95\%}}$. (d) the shaded area corresponds to the 95% of the particles that, seen in Frame2, can be paired with the ones in Frame1, called $PP_{2_{95\%}}$.

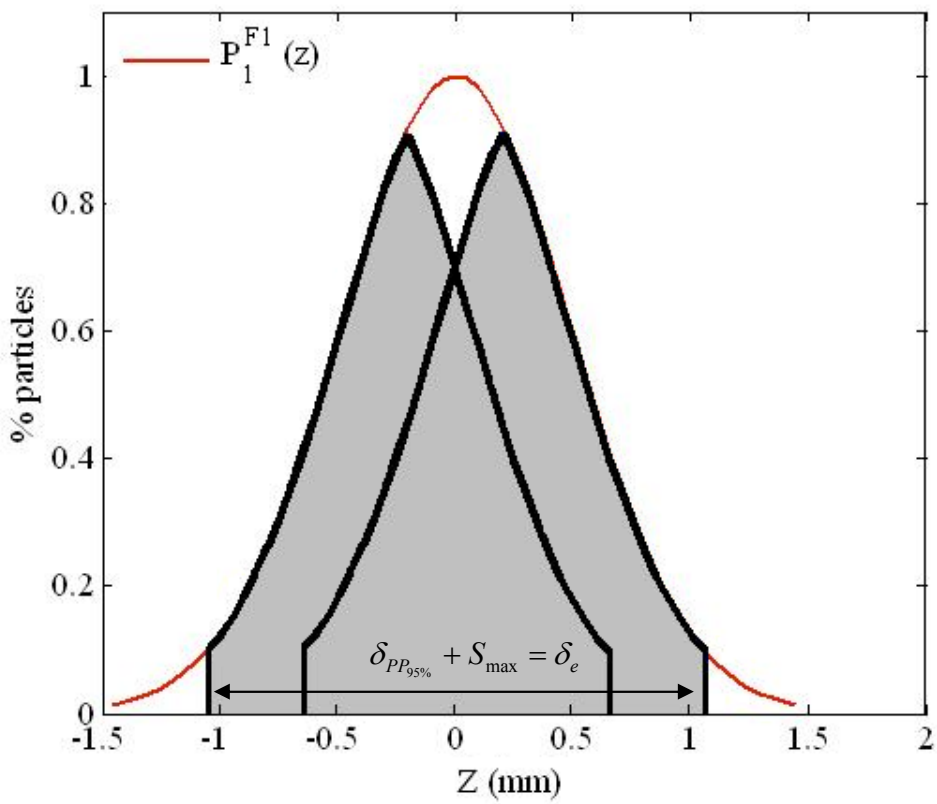

Figure 3.12. Graphical representation of δ_e. For a volume of fluid of the size δ_e^3, centered across the laser sheet, matching criteria [1], at least the 95% of the detected particles (in either Frame1 or Frame2) are successfully paired in the PIV process, as their velocity keep correlated to itself for a time τ_v..

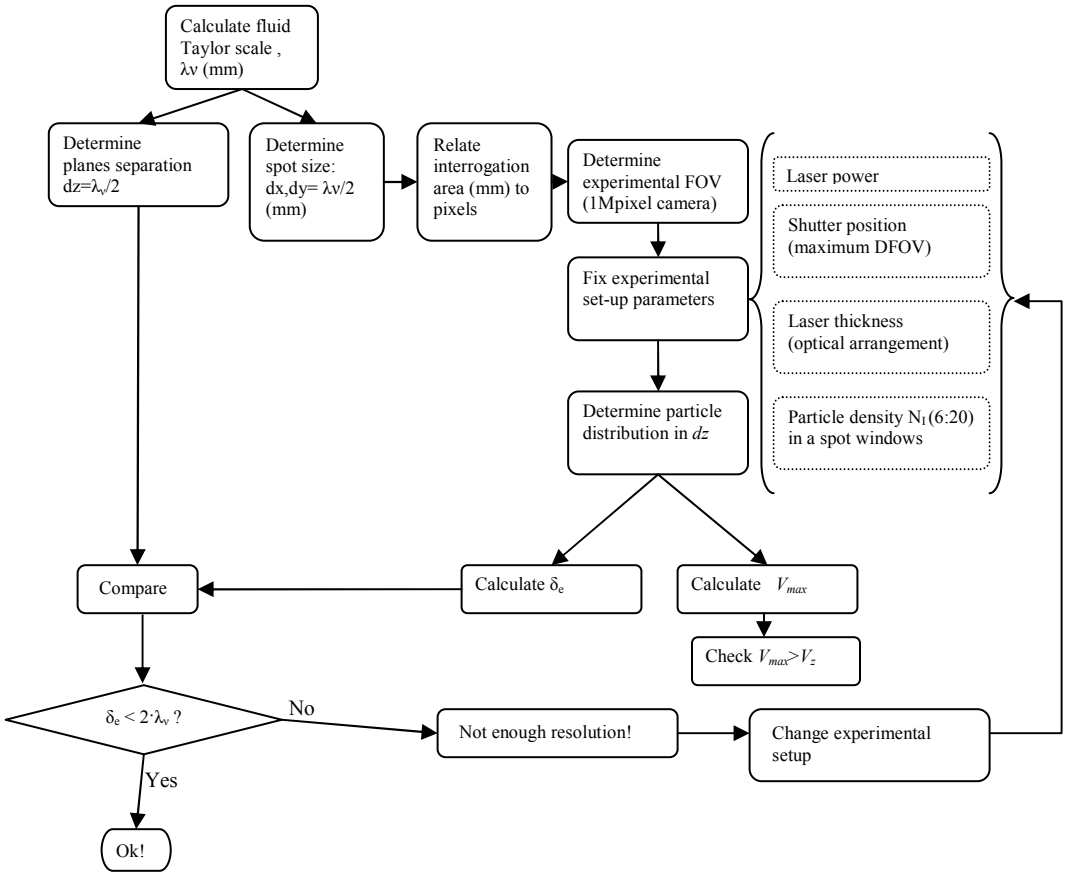

Figure 3.13. Experimental design process flow chart.

Chapter IV

Experimental Setup

The TR SPIV system described in Chapter II was used to study the velocity fields at the small scales of turbulent shear flows. The basic concepts, limitations, calibrations and parameters that define and control the different components of the TR SPIV system are described in Chapter II; while the criterion to determine the smallest flow scale measurable according to those parameters is explained in Chapter III. The setup for the turbulent jet that will be studied and the settings for the optical arrangement and synchronization are described in this Chapter.

4.1 TR SPIV experimental setup

The laser sheet was created with the set of optic lenses described in Section 2.2. The rotation of the scanning mirror inserted in the laser path allowed the scan of the control volume. The software Insight 3G time-capture settings and an electrical triangular wave signal that regulated the movement of the rotating mirror were synchronized as specified in Sections 2.4-2.5 to control the timing and position of the laser sheet pulses.

The minimum spacing between the centers of the scanning planes was set equal to the laser sheets' "effective thickness" calculated in Chapter III (2.12 mm). This avoided any

overlapping between scanning planes, and hence maximized the size of the measurement volume.

The time between laser pulses was set to 500 microseconds. This reduced the camera resolution to 1024x512 pixels. A Phoenix 100mm Macro camera lens was used with the shutter aperture set to *f*:11. The field of view was 446x223 mm. The average effective particle density per interrogation windows was 6 particles, with an average range of particle sizes of 3-6 pixels. Ten laser pulses were used to scan the control volume. The final size of the measured volume was approximately 44.6x22.3x21.2 mm^3.

The image pairs taken from the illuminated planes at two consecutive scanning periods were rearranged according to the scheme shown on Fig 2.9 to create PIV image pairs. The control volume was scanned within 0.45 milliseconds. The time required to capture a PIV image pair was dt=1 ms. Table 4.1 shows the main parameters related to the synchronization of the TR SPIV used during the experiments.

Parameter description	**Symbol**	**Value**	**Units**
Effective thickness	δ_e	2.12	mm
Number of planes	n_{lp}	10	-

Time between laser pulses	t_{lp}	500	µs
Laser pulses frequency	f_{lp}	2000	Hz
Scanner-signal frequency	f_s	100	Hz
Scanner-signal peak-to-peak voltage	V_{pp}	359.8	mV
Time in scanning one volume	t_{scan}	0.45	ms
Time between frames in PIV images	dt	1	ms
Time between successive scanned volumes	-	1	ms
Time between contiguous reconstructed volumetric vector fields	-	1	ms

Table 4.1. Key experimental parameters in the synchronization of the scanning TR-SPIV system.

A FFT cross-correlation algorithm from Insight 3G software was applied for the calculation of the vector fields in each plane. As the main processing parameters, the interrogation window size was set to 40x40 pixels, with 50% overlap, and the Gaussian Peak-to-Background-Peak threshold (parameter used to validate the Gaussian peak obtained in the correlation) was set to 1.3. No pre-processing of the images was considered necessary for the experiment. Only a 3x3 local median validation filter was used as post-processor replacing the spurious vectors by the neighbor 3x3 mean. The percentage of good vectors for the processed images was $\geq$97%.

Seven independent series of 360 individual images were collected, resulting in seven sets of 17 volumetric vector fields reconstructed.

4.2 Flow facility

The turbulent jet in the free flow facility used in this study is shown in Fig. 4.1. The primary components include the jet, the water tank and the injection system.

A 0.75x0.3x0.3 m^3 water tank made of glass allowed full optical access for the scanning laser and camera. The front tank wall was centered and perpendicular to the incident beam when the scanning mirror was at the mechanical zero position. The experimental facility for the present work used hollow glass spheres, with mean diameter of 10 micrometers and mean density of 0.8 g/cm^3, as tracers in water in constant temperature of 22 ºC.

The jet itself consisted of an 80 mm-long piece of rigid acrylic tube with 6 mm-outside diameter and 3mm-inside diameter. The tube was connected to the injection system by a flexible plastic hose with 3 mm inside diameter. The jet was mounted on a rigid base and fixed to the back wall of the tank. It was aligned with the incident laser sheet for the mechanical zero position of the mirror. The nozzle exit was set perpendicular to the incoming laser sheet.

The flow was driven by a Harvard PHD 2000 syringe pump. Two 150 cm^3 syringes were used simultaneously, inducing a 210 cm^3/min flow rate at the jet nozzle. The center point of the measurement control volume was located 475 mm away from the jet exit, as shown in Fig. 4.2. At that point, the Taylor micro-scales of the flow was 4.24 mm. Table 4.2 lists the key experimental conditions in this study.

Parameter description	**Symbol**	**Value**	**Units**

Kinematic viscosity	ν	$1.00472 \cdot 10^{-6}$	m^2/s
Flow rate	Q	210	cm^3/min
Nozzle diameter	D	0.003	m
Jet exit velocity	U_o	0.495	m/s
Jet Reynolds number	Re	1478	-
Momentum flux	J_o	$1.729 \cdot 10^{-3}$	N
Distance of the control volume from jet exit	x	0.475	m
Local jet centerline velocity	u_c	0.0199	m/s
Local outer length scale	δ	0.171	m
Local outer time scale	τ_δ	8.59	s
Local outer-scale Reynolds number	Re_δ	3387	-
Local Taylor length scale	λ_ν	4.24	mm
Local Taylor time scale	τ_ν	18	s
Local mean dissipation rate	ε	$3.72 \cdot 10^{-6}$	m^2/s^3
Size of the PIV interrogation spot	$\Delta x, \Delta y$	1.74	mm
Separation between measurement planes	Δz	2.12	mm
Local Kolmogorov length scale	λ_k	0.72	mm
Local Kolmogorov time scale	τ_k	0.519	s

Table 4.2 Key experimental parameters. The local parameters are calculated at the center of the measurement control volume, at $158.3 \cdot D$ from the jet exit

The syringes were filled for each experiment using fluid from the tank. The temperature and the tracer density on the jet and background fluids were identical. After refilling the syringes, the flow was allowed to settle in the tank for 5 minutes before the experiment was performed. At least 30 minutes passed between different data sets to allow the flow in the tank to come to rest from a previous injection.

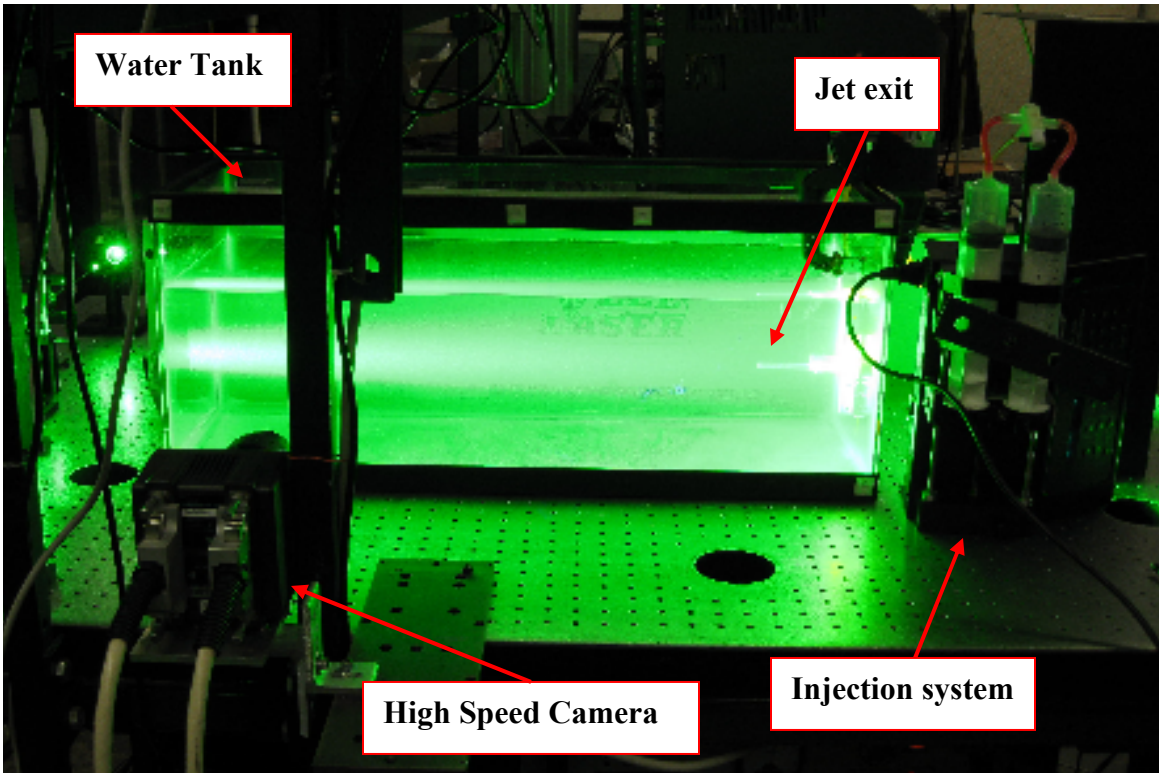

Figure 4.1. Photography of the TR SPIV experimental set up showing the High Speed Camera, water tank, jet and injection system.

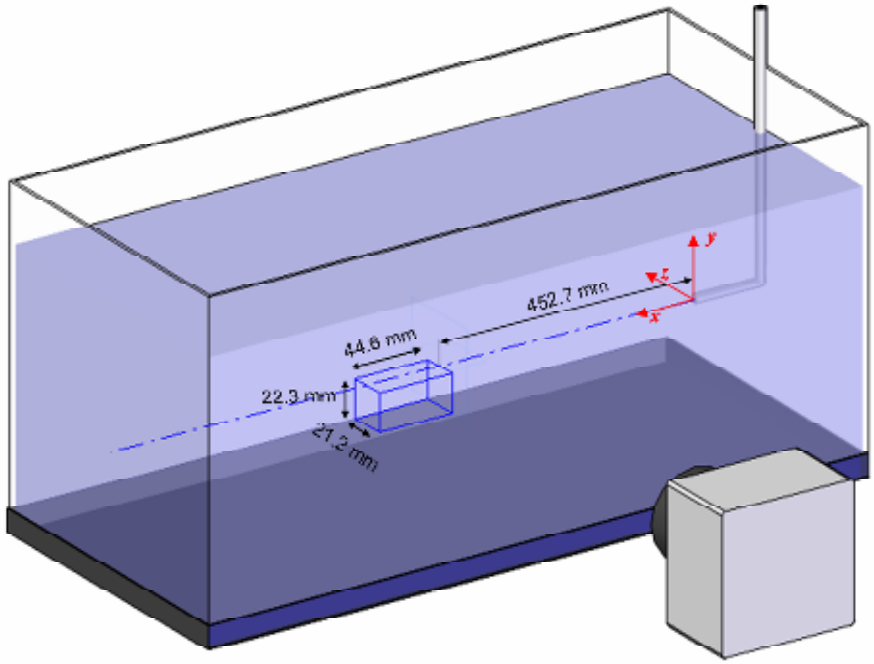

Figure 4.2. Scheme of the position of the control volume on the experimental set up.

Chapter V

Experimental Results and Discussion

This chapter presents results from the study of volumetric velocity fields in a volume that resolves the small scales in a turbulent shear flow, under incompressible and isothermal conditions, based on the measurements taken with the Time Resolved High Speed Scanning Particle Image Velocimetry system developed for this work.

Briefly, the following measurements were performed with the developed system:

- validation of the measurement technique in a turbulent jet. We compared planar measurements taken approximately at the center-plane of the jet with previous studies;
- reconstruction of quasi-instantaneous 2D velocity vector fields in a volume;
- study of the u-and-v velocity gradients in the x-, y- and z- direction in a volume;
- tracking the evolution in time of the quasi-instantaneous volumetric vector fields.

These results provide key information on the volumetric structure and dynamic properties of the small scales on isothermal, incompressible turbulent shear flows; where the experimental results are quite limited, and can provide a basis for development of improved turbulence models.

5.1 Planar measurements

5.1.1 Validation of PIV measurements in a turbulent jet

The flow facility in the present work was validated using classical planar PIV measurements. Measurements of the mean velocity profile and velocity fluctuation profiles were compared with results in the literature for jets in still flow.

Classical planar PIV measurements with a field of view of 90x75 mm were taken at the center plane of the jet, centered at 210 mm from the jet source. Fifteen independent sets of 20 PIV pairs of images each were taken, and the averaged velocity magnitude profile obtained is shown in Fig. 5.1a. The color bar represents the in-plane velocity magnitude. The *x*- and *y*- coordinates are normalized by the jet diameter. Figures 5.1b, 5.2a and 5.2c show the radial profiles of the streamwise velocity component (u), streamwise velocity rms fluctuations (u_{rms}) and radial velocity rms fluctuations (v_{rms}), at 200 mm from the jet source; all of them were normalized by the centerline streamwise velocity. Statistical data from previous measurements on jets on free flow [10][28][29] are shown in Figs. 5.2c and 5.2d for comparison with the present results.

The rms fluctuations u_{rms} and v_{rms} obtained near the center plane of the control volume section are presented in Fig. 5.3. Although measurements were taken at multiple planes, only the ones closer to the centerline of the jet were used for this analysis. In the calculation of the radial profiles of the rms fluctuations in streamwise (u_{rms}) and radial (v_{rms}) velocity components, the local profiles obtained are integrated along the streamwise

x- direction. Both u_{rms} and v_{rms} fluctuations are slightly higher than the literature compared values (Figs. 5.2c and 5.2d), which is attributed to the lack of sufficient statistical independent measurements to get a good velocity average profile. The present study is focused on the instantaneous evolution of the small scales, instead of the average velocity statistics, therefore no large sets of data were taken for the u_{rms} and v_{rms}. However, the results appear to reasonably converge.

The local outer centerline velocity measured for the jet in the present work is compared to the predicted local outer velocity ($u_c(x)$) based on the experimental results by Diez *et al* [23] for turbulent jets in free flow. The mean velocity magnitude profile obtained near the jet centerline is shown in Fig. 5.4. The measurement plane was approximately parallel to the jet centerline, at 1.05 mm from it. The experimental value of $u_c(x)$ at 475 mm from the jet source is 0.0199 m/s, while the predicted value from Eq. 3.3 is 0.02106 m/s. The 5% error is attributed to the lack of sufficient statistical independent measurements.

5.1.2 Sample instantaneous velocity fields

Figures 5.5 and 5.6 show two examples of the measured velocity magnitude $V(x,y)$ and velocity vector components $u(x,y)$, $v(x,y)$ and its evolution between two successive scanning periods. The dimensions are indicated in terms of the local inner length scale λ_v, and the color bar gives the velocity component values normalized by the local inner velocity scale ((ν/λ_v)). The timing between frames on the PIV images was 1 ms, which is the same that time between vector fields obtained for successive measurements taken at

the same plane position. The high time resolution of the measurement technique allows the inspection of the evolution on time of the velocity fields.

Figures 5.7 and 5.8 show two examples of velocity vector fields measured for the ten differentially-spaced planes. The actual separation between planes was approximately 2.12 mm; and the time difference between the measured velocity fields of contiguous planes 500 μs. The velocity fields observed trough the planes that compose the measurement volume appear to be highly correlated, indicating that the spatial resolution of the measurement technique seems to be sufficient to observe the spatial structure of the velocity fields at the small scales of the flow without the loss of relevant information about the fluid motion between planes. Nevertheless, this is not sufficient to proof that the time delay between contiguous planes does not affect the measurements of a scanned volume, and it will be discussed later.

5.2 Volumetric measurements

The measurements taken on the ten approximately-parallel light sheets that form the observed volume were reconstructed on a 3D-spatial grid as parallel planes with a distance between them of approximately 2.12 mm.

The small error on the reconstruction of the volumetric vector field, due to the measurement planes not being exactly parallel, can be related to the positioning of the velocity vectors on the volumetric spatial grid. Note that, according to the position of the camera lenses perpendicular to the plane z=0, the in-plane displacement on the PIV

images corresponds to the *u* and *v* velocity components. The error on the *z*- position of the vectors due to this effect is directly related to the angle of the laser sheet respect to the jet centerline, and estimated to be ± 0.11 mm.

Tecplot10 software was used for the spatial reconstruction, calculation of velocity related parameters (velocity gradients and fluctuations) and volumetric visualization of the planar velocity fields obtained with Insight3G. The actual separation between scanning planes is about 2.4 times the vector-to-vector spacing within each plane (due to the 50% overlap used on the PIV correlation). The space between vectors is linearly interpolated to create volumetric two-dimensional velocity fields.

5.2.1 Average velocity vector fields

Figure 5.9 shows the mean volumetric velocity field obtained from the 119 volumes reconstructed. These results are only shown for qualitative analysis (not enough statistically independent data sets), and therefore the velocity magnitude values are not normalized. The color bar gives the velocity magnitude values in m/s. The vectors are two-dimensional, representing the *u* and *v* velocity components, as the velocity was obtained on the in-plane coordinates of the measurement planes. Some expected features from the obtained mean average velocity profile can be observed:

- the velocity magnitude profiles on planes of constant z are approximately symmetric respect to the vertical plane that contains the jet centerline (plane at constant *x*)

- Figure 5.9c shows 3 isocontours of constant velocity magnitude: 0.011, 0.013 and 0.015 m/s. The isosurfaces are elongated on the *y*- direction, mainly attributed to the fact that the velocity magnitude is computed only from the *u* and *v* velocity components.

5.2.2 Sample quasi-instantaneous velocity and vorticity fields

Figures 5.10-5.11 show two examples of quasi-instantaneous volumetric velocity fields, obtained from two independent data sets. The color bar gives the velocity component values normalized by the local inner velocity scale (ν/λ_v). The vectors are two-dimensional, representing the *u*- and *v*- velocity components. To allow a better visualization of the flow, three isosurfaces of constant velocity are represented in Figs. 5.10b and 5.11b.

Figures 5.12 and 5.13 show velocity magnitude contour plots extracted at planes of constant *x*- and *y*- coordinates, respectively, from the instantaneous volumetric field represented in Fig. 5.11. The separation between the planes extracted is 2 mm. It can be observed that the resolution of the measurements on the three planes is similar, which confirms that the spatial resolution of the system is appropriate for the flow conditions studied.

5.2.3 Sample velocity gradient fields

The velocity gradient fields were obtained by central differencing of the measured velocity component fields in the *x*-, *y*- and *z*- directions within each measurement plane,

resulting on six of the nine tensor component values at each point ($\partial u/\partial x$, $\partial u/\partial y$, $\partial u/\partial z$, $\partial v/\partial x$, $\partial v/\partial y$ and $\partial v/\partial z$). Results were normalized on the inner velocity gradient scales (ν/λ_v^2). The color bar represents the normalized velocity gradient component values. The arrows represent velocity direction.

Figures 5.14, 5.15 and 5.16 show the calculated velocity gradient components at 3 slices taken at z/D=-0.37, *x/D*=153.8 and *y/D*=-2.34 respectively from the volume in figure 5.11. Qualitatively, the magnitude and pattern observed on the velocity gradients is similar for the 6 different tensor components, and for the data obtained at slices at constant *x*, *y* or *z*. It can be observed that the resolution of the measurements on the three planes is similar, which confirms that the spatial resolution of the system is appropriate for the flow conditions studied.

5.2.4 Probability densities of velocity gradients

Figure 5.17 shows the probability density functions (pdfs) of the velocity gradients obtained for the volumes analyzed in this experiment, normalized on the inner scales. The present experiment Re_δ was 3,396.

Mullin *et al* [14] normalized velocity gradients pdfs obtained at Re_δ=30,000 are shown in Fig. 5.18 for comparison with the present data. In principle, the inner-variable scalings should become Re_δ delta independent at sufficiently large values of Re_δ. The similarities between the pdfs is a good indication the Re_δ number for the present experiments was high enough for the fluid to achieve the the quasi universality of the velocity gradients.

Figures 5.19a and 5.19b show the pdfs of the velocity gradients in semi-logarithmic axes for the on diagonal and off-diagonal components. Homogeneous isotropic turbulence theory suggests that the pdfs for the on-diagonal components of the velocity gradients should be identical, as well as the off-diagonal components. Further test for classical isotropy would consist in checking that the width of the rms values of the on- and off-diagonal velocity gradient components are related as follows

$$\frac{\left[\overline{\left(\frac{\partial u_i}{\partial x_j}\right)^2}\right]^{1/2}_{i\neq j}}{\left[\overline{\left(\frac{\partial u_i}{\partial x_j}\right)^2}\right]^{1/2}_{i=j}} = \frac{\left(\frac{2\varepsilon}{15\nu}\right)^{1/2}}{\left(\frac{\varepsilon}{15\nu}\right)^{1/2}} = \sqrt{2}\ . \qquad 5.1$$

It can be observed in Fig. 5.19a that the components and relative width of the pdfs for the on-diagonal velocity gradients ($\partial u/\partial x$, $\partial v/\partial y$) are nearly similar, even for events at the tails of the pdfs, which have a frequency of occurrence nearly 10^4 times smaller than the mean. They also seem nearly symmetric. This provides assessment of isotropy in the on-diagonal velocity gradients.

The pdfs for the off-diagonal velocity gradients in Fig. 5.19b show apparent departures from isotropy. The pdfs of the off-diagonal velocity gradients $\partial u/\partial y$ and $\partial v/\partial x$ seem wider than the on-plane pdfs, which is consistent with the classical results from homogeneous isotropic turbulence. The pdfs of the velocity gradients $\partial u/\partial z$ and $\partial v/\partial z$ seem significantly different from the pdfs of $\partial u/\partial y$ and $\partial v/\partial x$ in height and symmetry.

This deviation could be attributed to the errors in the calculation of the z-spacing between velocity vectors obtained at different measurement scanning planes. The two main sources of error are that the measurement planes were not exactly parallel, and/or any experimental error in the estimation of the exact position of the planes in real space (variations in the V_{pp} voltage of the electric wave that regulates the angle in the scanning mirror, created with an analogical signal generator; and the neglecting of the effects of the glass tank wall index of refraction in the position of the laser sheet).

5.2.5 Time evolution of volumetric velocity fields

Figures 5.20 show the evolution in time of two sample volumetric velocity field during 7 ms. The isocontours of velocity magnitude for 10 consecutive volumes are represented. The dimensions of each plane are indicated in terms of the local inner length scale λ_v, and the color bar gives the velocity component values normalized by the local inner velocity scale (ν/ λ_v). The change on the velocity isocontours is relatively small between consecutive images. This leads to the confirmation that the time between one scanning period is small enough to assume that the flow is “frozen” during one scanning process.

a)

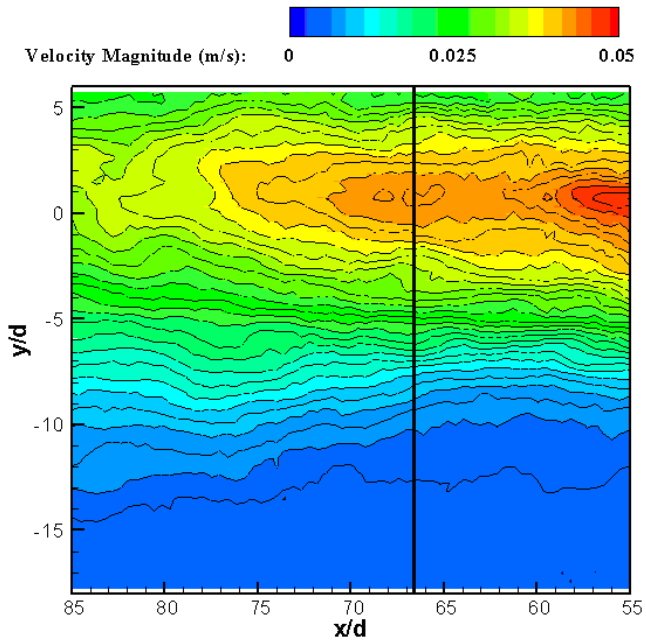

b)

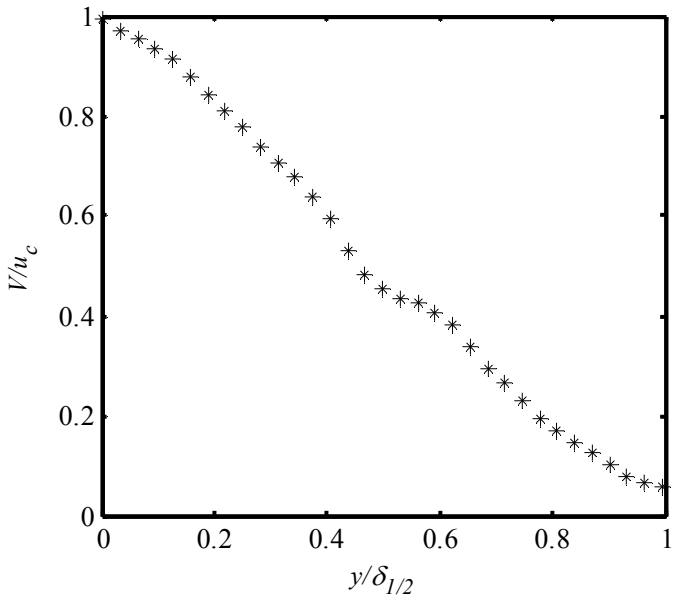

Figure 5.1. (a) averaged velocity magnitude profile obtained at the jet center plane, centered at 210 mm from the jet exit with axis normalized by the jet diameter; (b) radial profile of the streamwise velocity component normalized by the local centerline streamwise velocity (V/u_c) at 200 mm from the jet exit (at the solid line indicated in (a)). The x-coordinate is normalized by the local half jet width $\delta_{1/2}$.

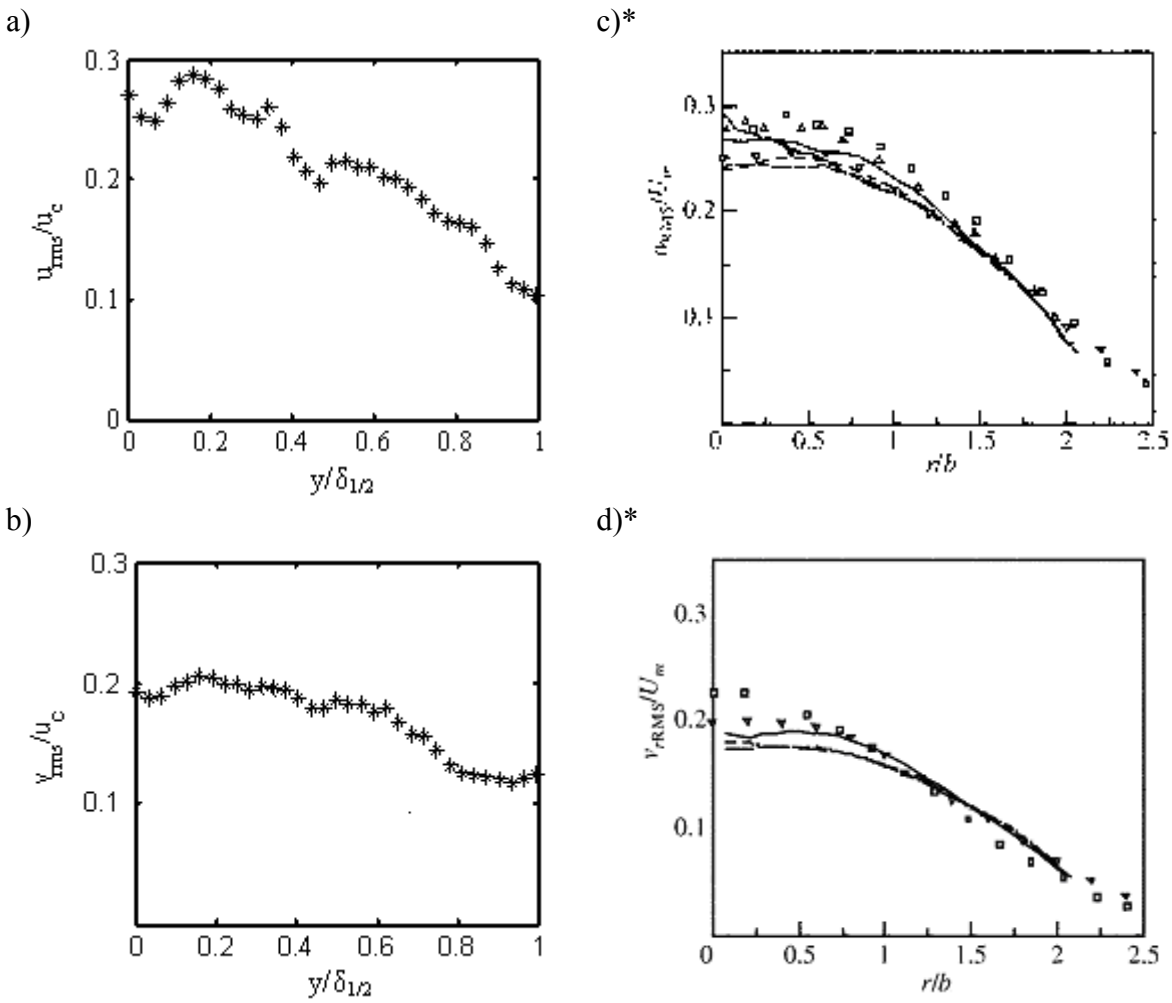

Figure 5.2. Radial profiles of the flucutations u_{rms} and v_{rms} statistical quantities of the jet at 200 mm from the jet exit; showing (a) intensity of streamwise velocity fluctuations and (b) intensity of radial velocity fluctuations. Plots from Matsuda and Sakakibara (2005) are shown in (c) and (d) with the following legend (—, Re=1500; —·—, Re=3000; —··—, Re=5000; ○,▲,■,---, Wygnanski and Fiedler (1969);▼, Ninomiya (1992)). In all cases the radial coordinate is normalized with the local half-value width of u_c; and the velocity with u_c.

a)

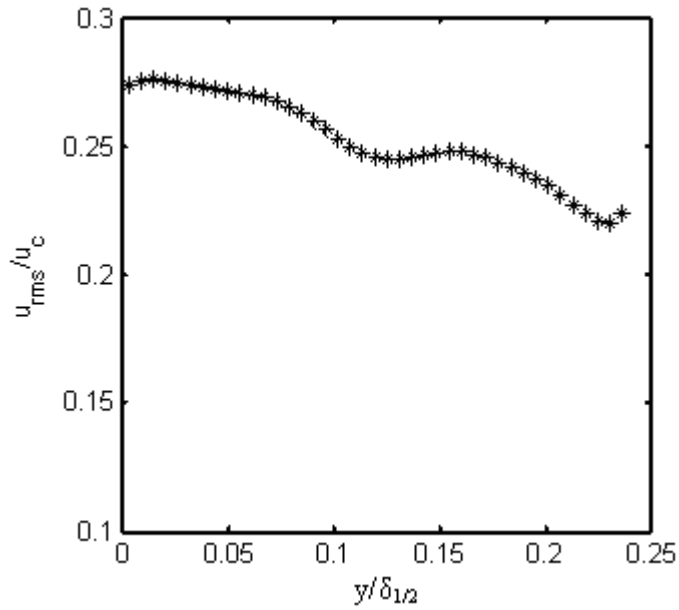

b)

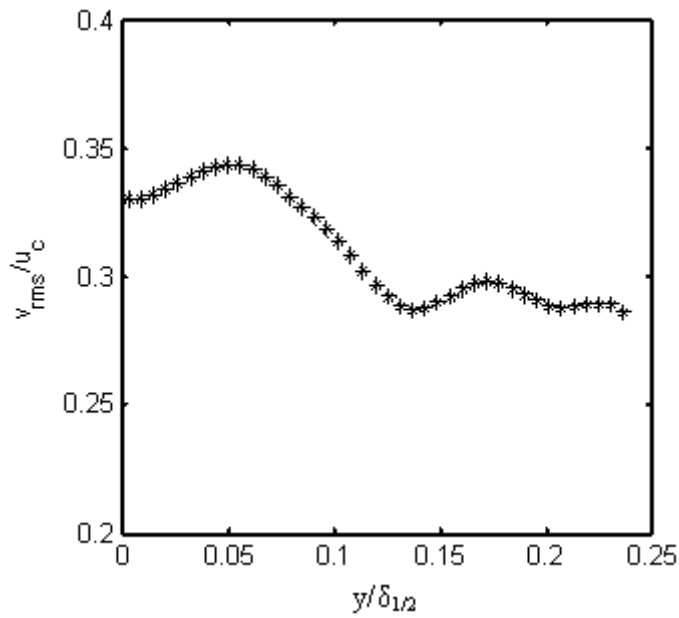

Figure 5.3. Radial profiles of fluctuations of the jet near the center plane of the control volume section, showing (a) intensity of streamwise velocity fluctuations and (b) intensity of radial velocity fluctuations.

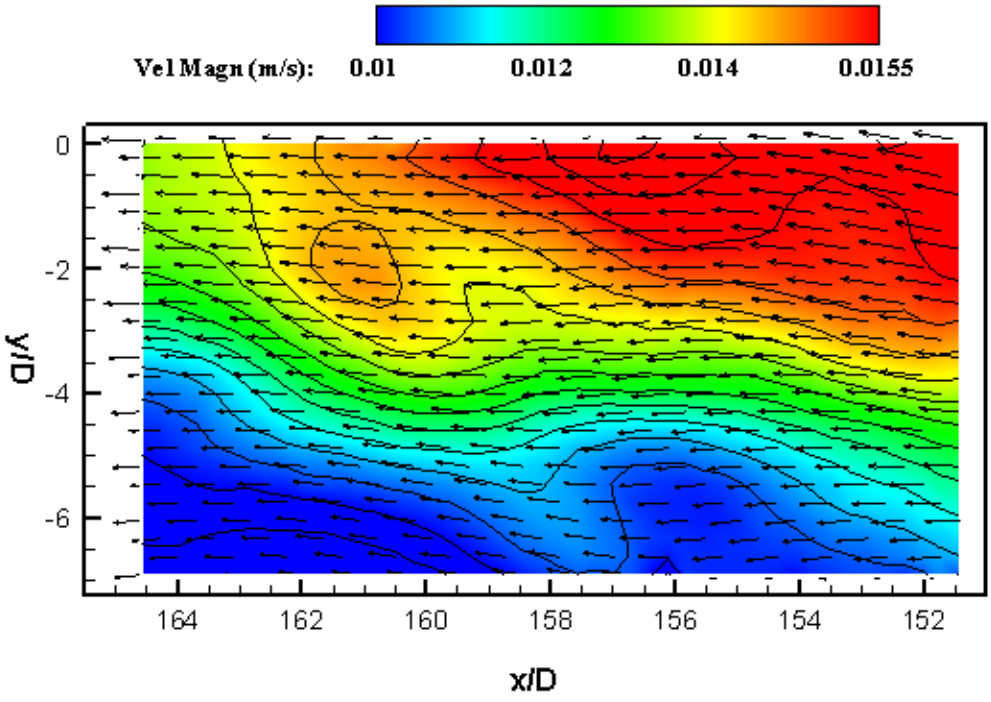

Figure 5.4. Averaged velocity magnitude profile obtained at a measurement plane near the center of the scanned volume (1.05 mm from the jet centerline)

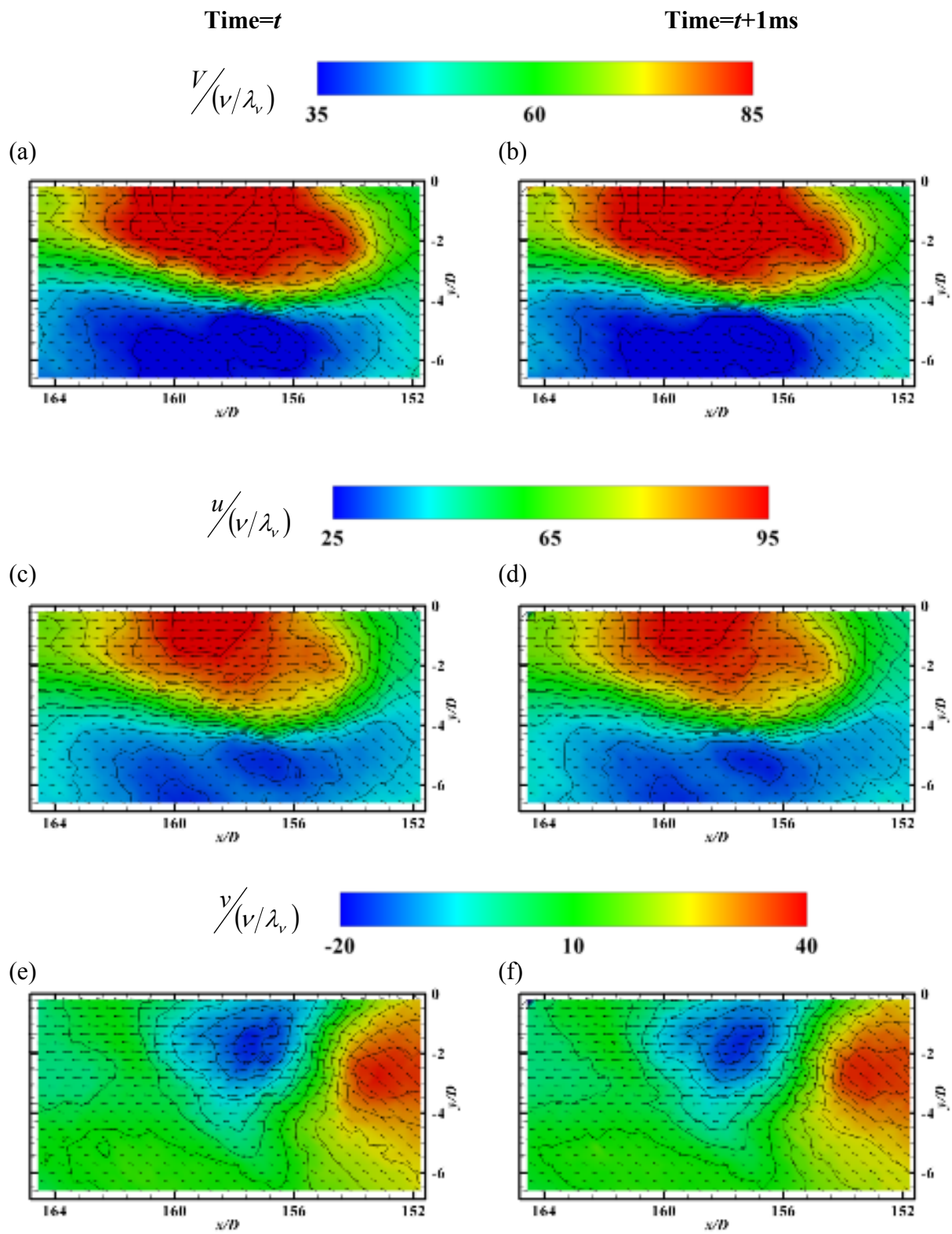

Figure 5.5. Example of the measured velocity and velocity components vector in one of the scanned planes of the control volume (near the center of the control volume), and its evolution between two successive scanning periods fields for *U(x,y)* (a-b); *u(x,y) (c-d); and v(x,y)* (e-f). The velocities are normalized by ν/λ_ν.

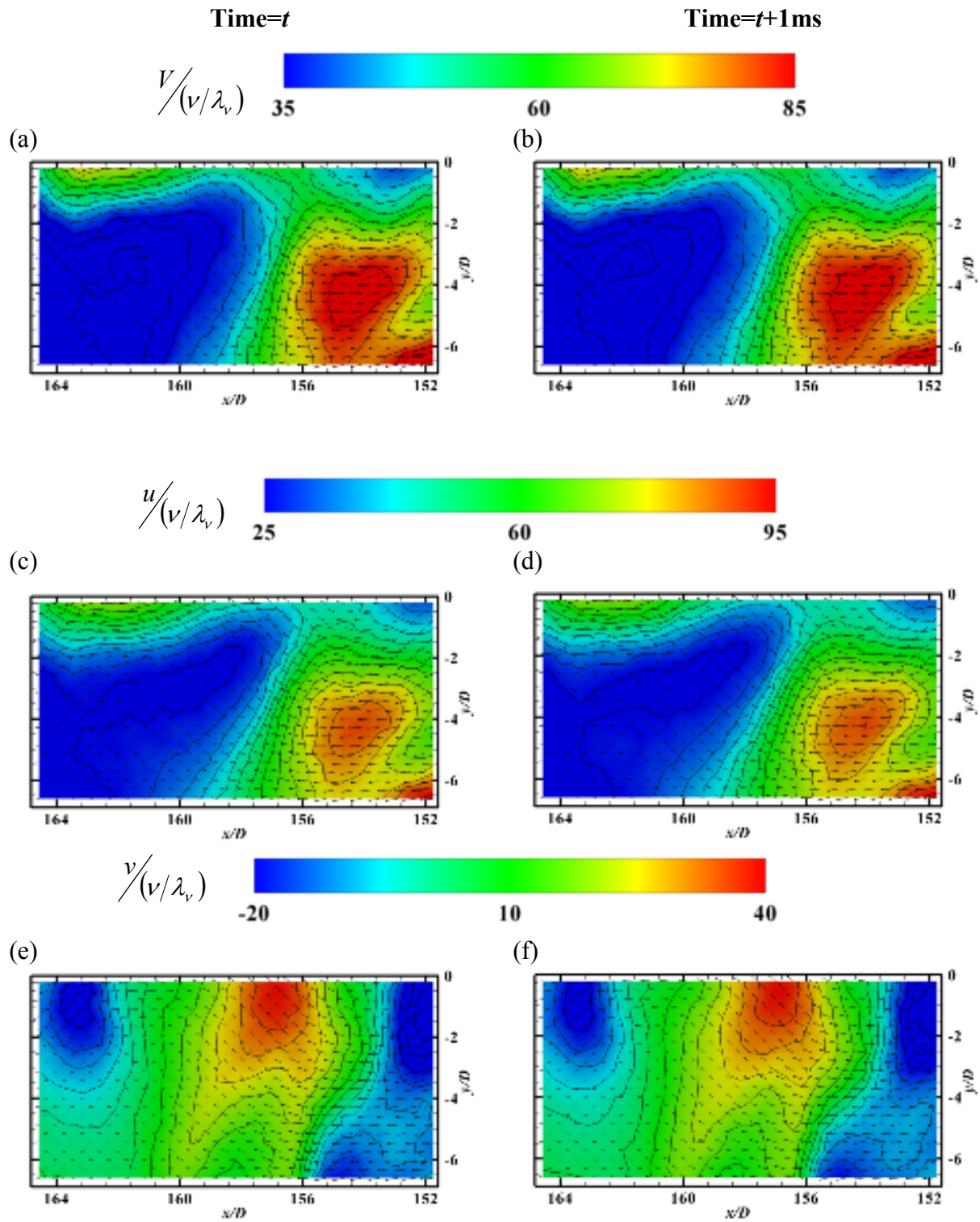

Figure 5.6. Other example of the measured velocity and velocity components vector in one of the scanned planes of the control volume (near the center of the control volume), and its evolution between two successive scanning periods fields for *V(x,y)* (a-b); *u(x,y) (c-d); and v(x,y)* (e-f). The velocities are normalized by ν/λ_ν.

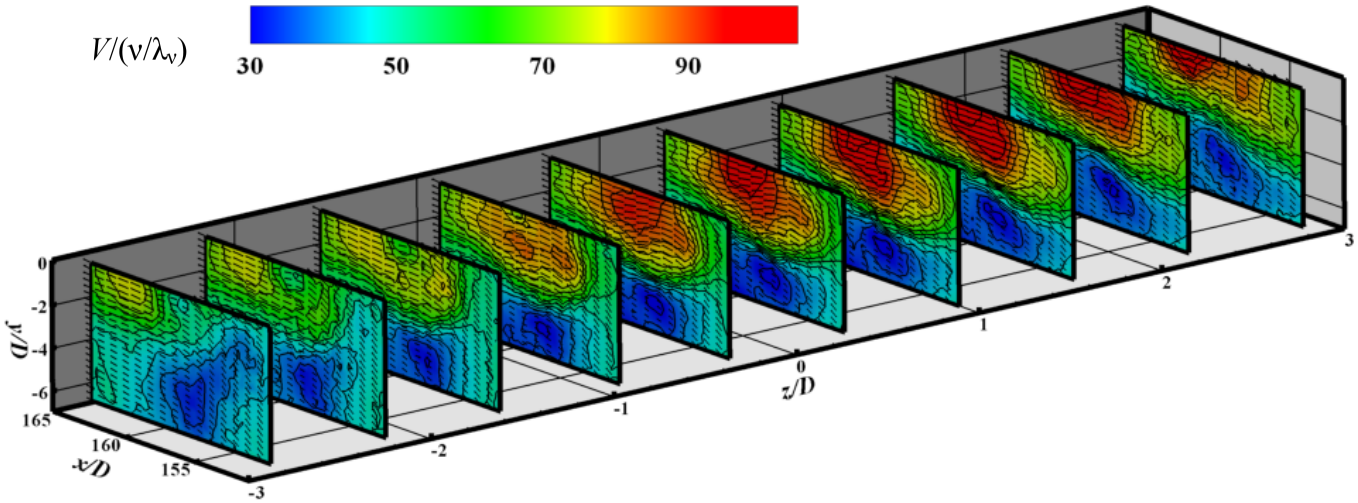

Figure 5.7. Example of the measured velocity magnitude at the scanned planes of the control volume.

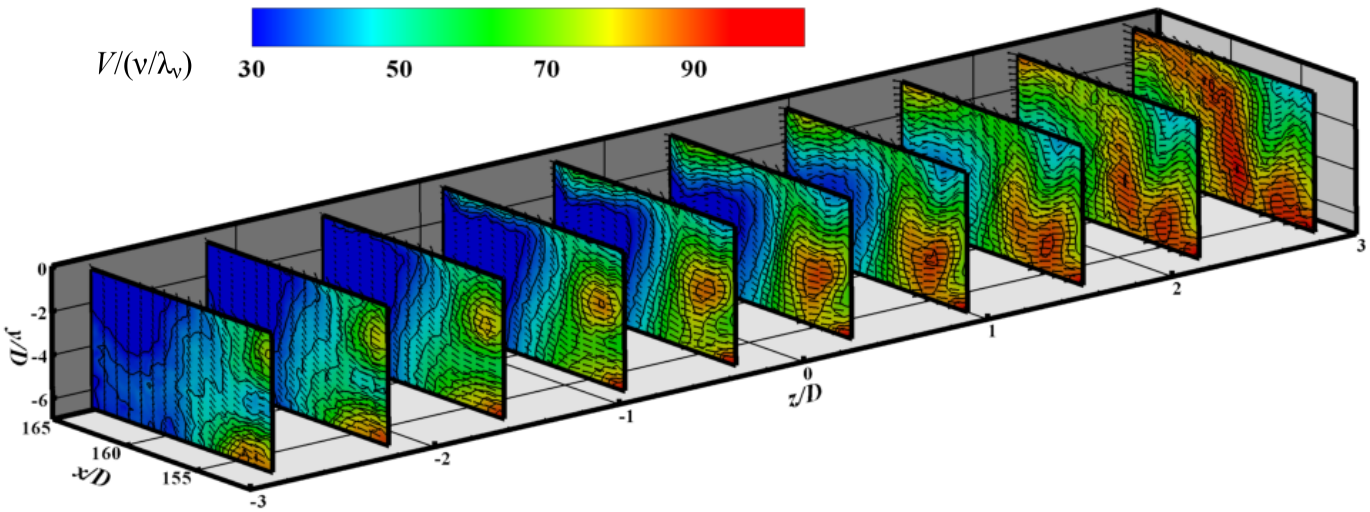

Figure 5.8. Example of the measured velocity magnitude at the scanned planes of the control volume.

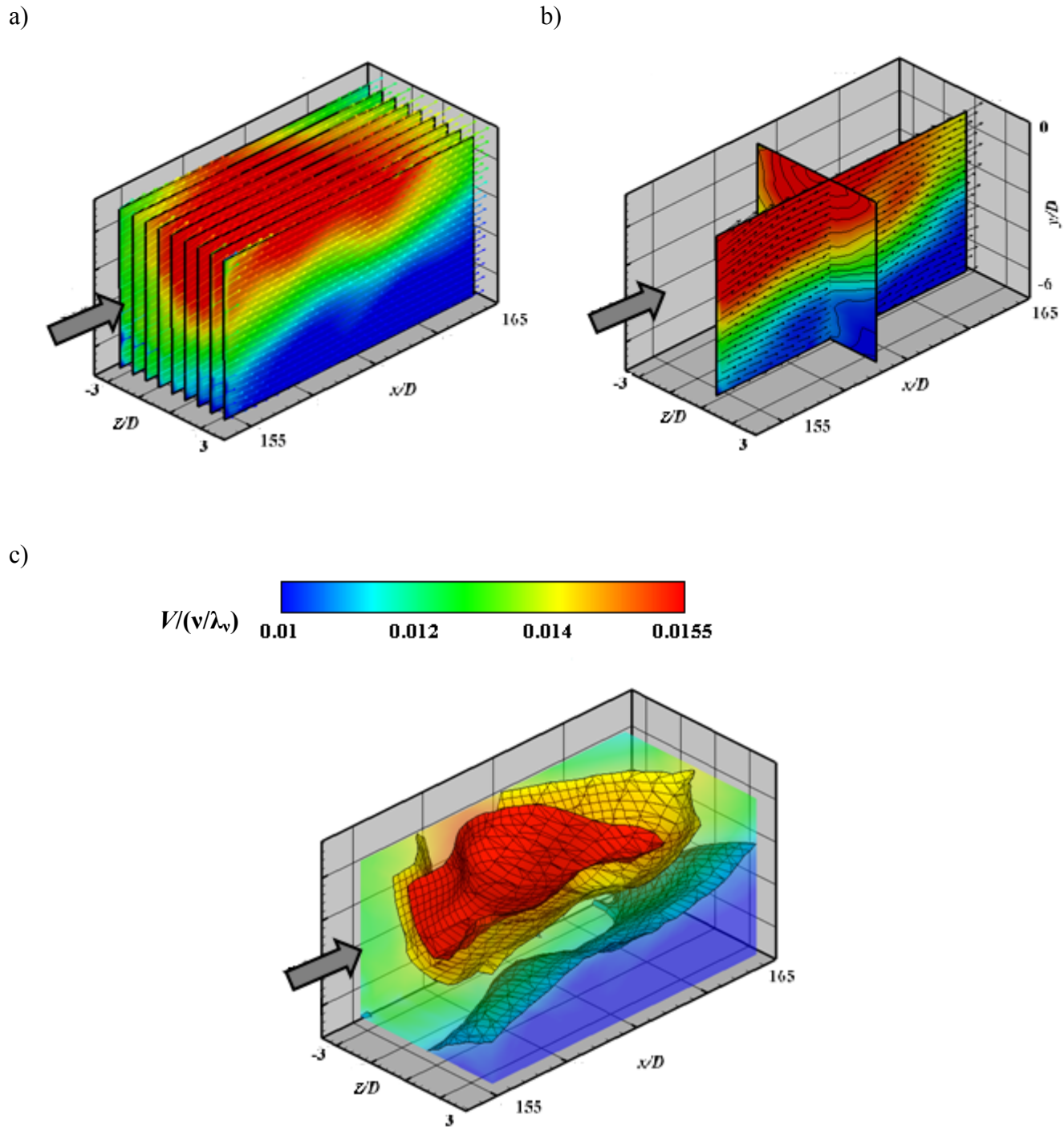

Figure 5.9. Averaged volumetric velocity field, showing (a) slices at constant z/D, (b) detail of two slices at constant *x/D* and *z/D*, (c) isocontours of velocity magnitude at 0.011, 0.013 and 0.015 m/s.

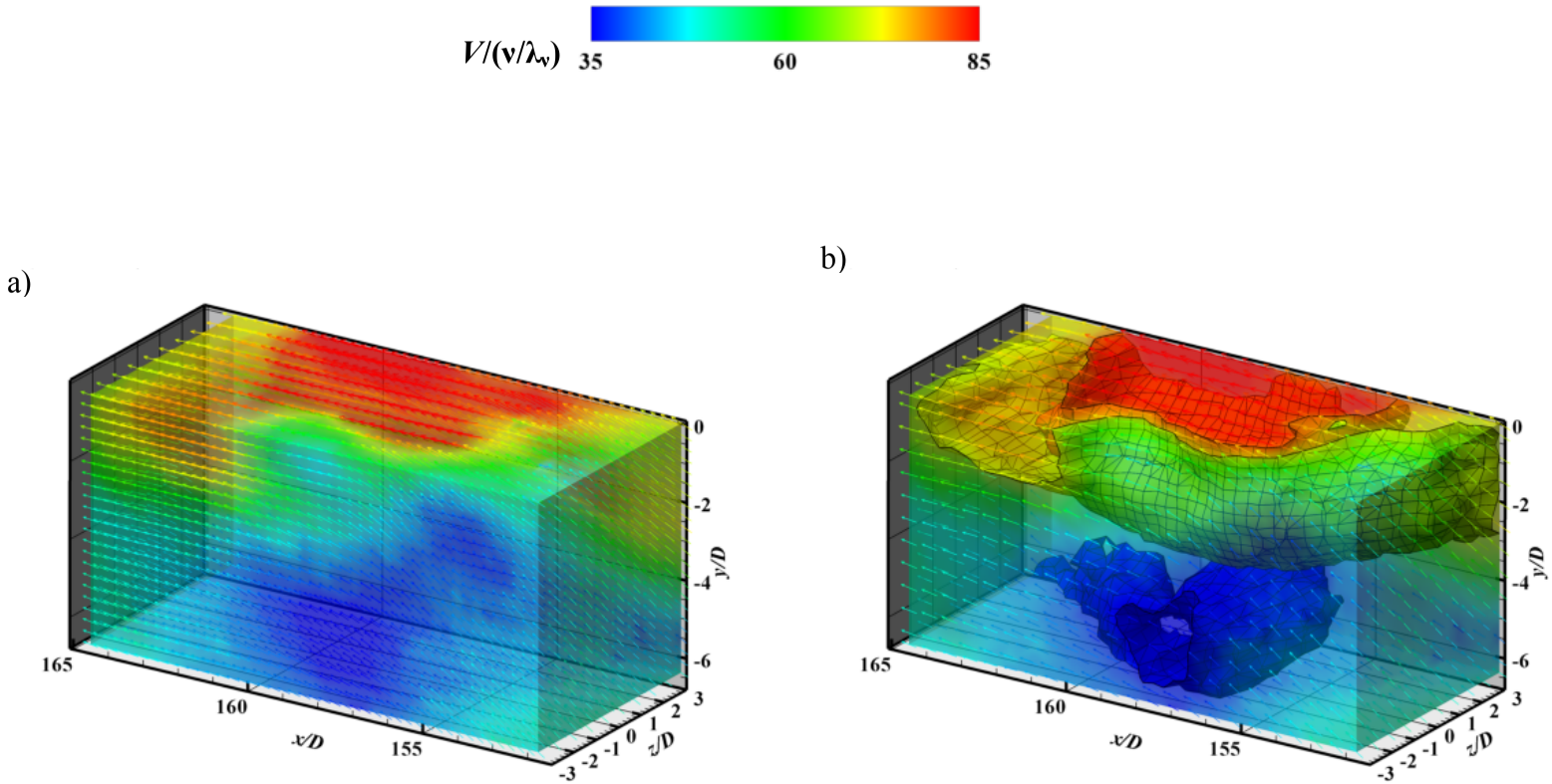

Figure 5.10. Example of a quasi-instantaneous volumetric velocity field reconstructed from the scanned *x-y* planes shown in Fig. 5.7. The color bar gives the velocity component values normalized by the local inner velocity scale (ν/λ_v). The vectors are two-dimensional, representing the u- and v- velocity components, as the velocity is obtained on the in-plane coordinates of the measurement planes. To allow a better visualization of the flow, three isosurfaces of constant velocity magnitude ($V/(\nu/\lambda_v)$.=35, 70 & 80) are represented in (b).

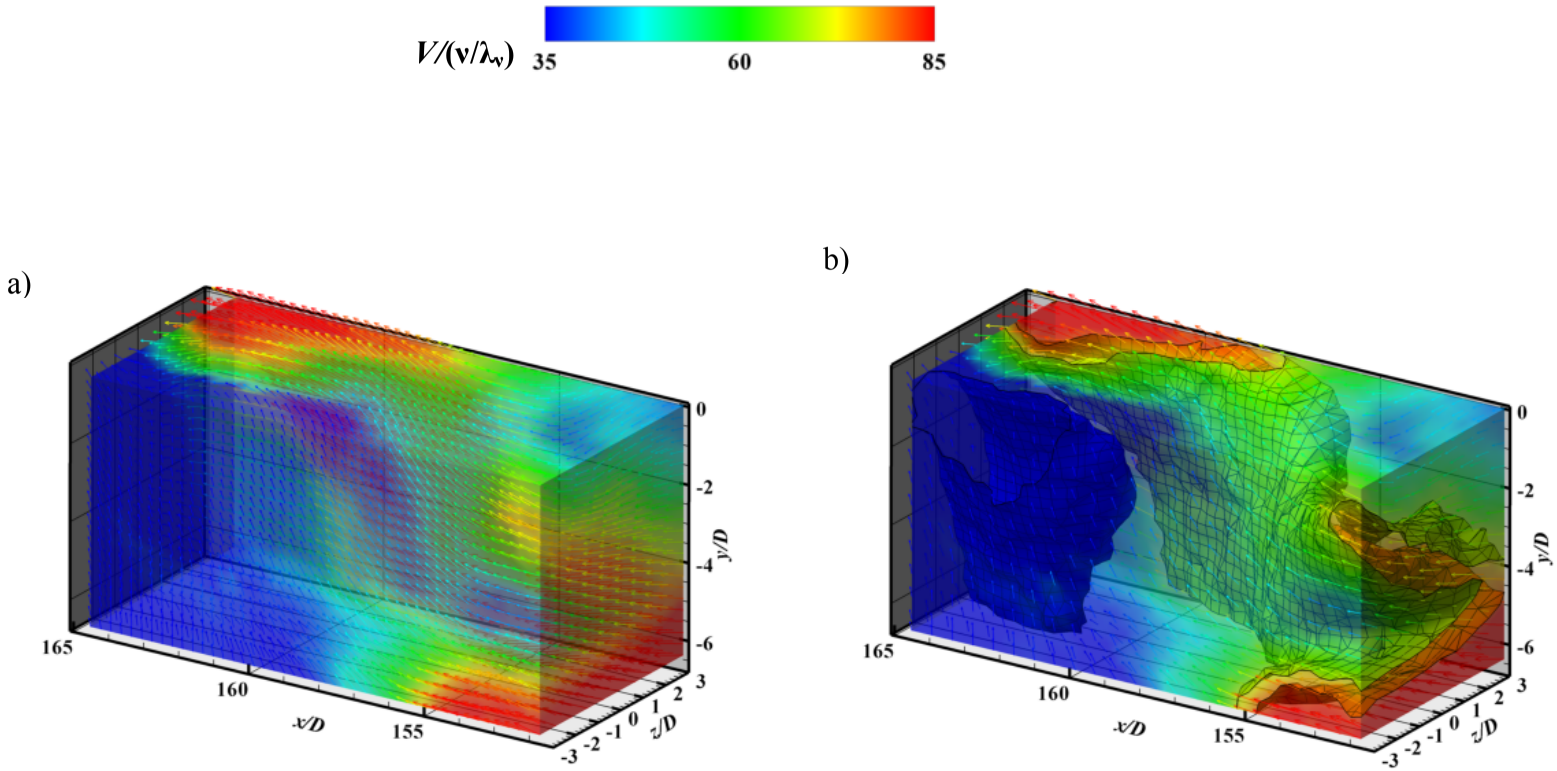

Figure 5.11. Example of a quasi-instantaneous volumetric velocity field reconstructed from the scanned *x-y* planes shown in Fig. 5.8. The color bar gives the velocity component values normalized by the local inner velocity scale (ν/λ_v). The vectors are two-dimensional, representing the u- and v- velocity components, as the velocity is obtained on the in-plane coordinates of the measurement planes. To allow a better visualization of the flow, three isosurfaces of constant velocity magnitude (V=25, 70 & 80) are represented in (b).

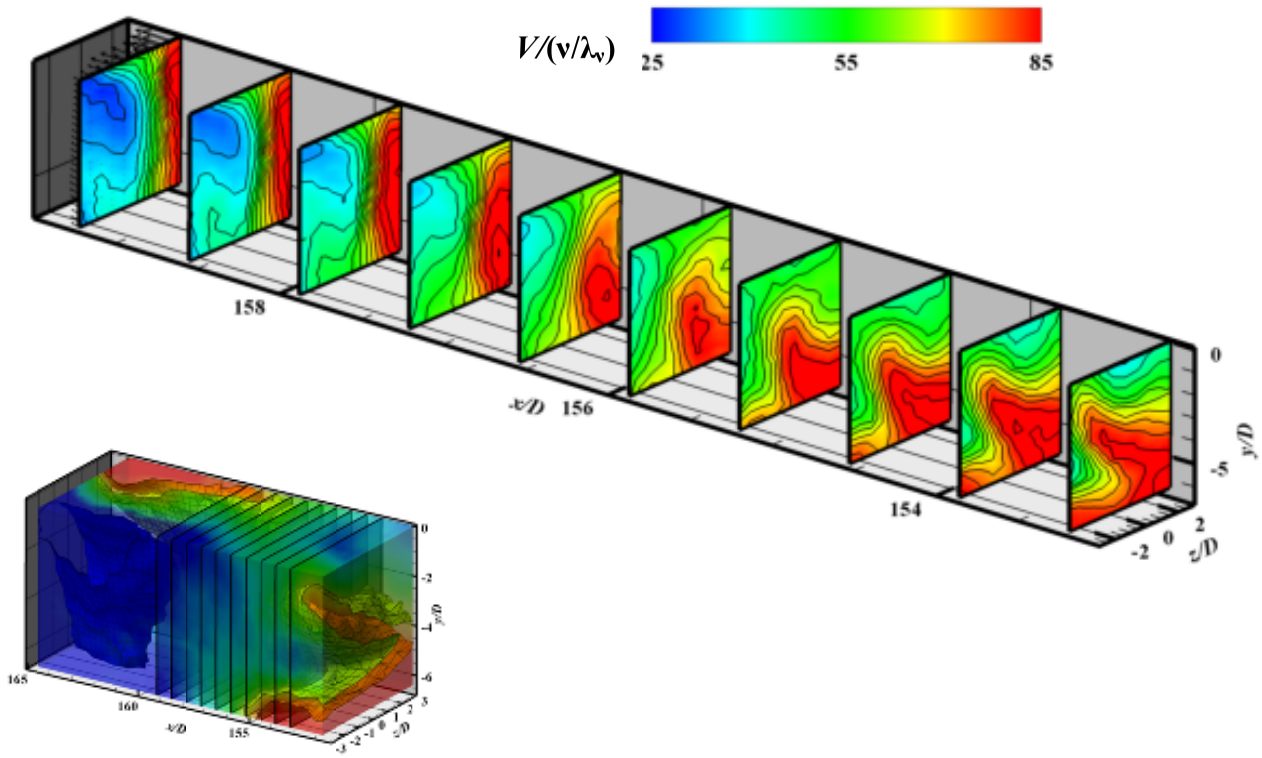

Figure 5.12. Example of the velocity magnitude contour plot at *z-y* planes. These planes are reconstructed from the scanned *x-y* planes shown in Fig. 5.11.

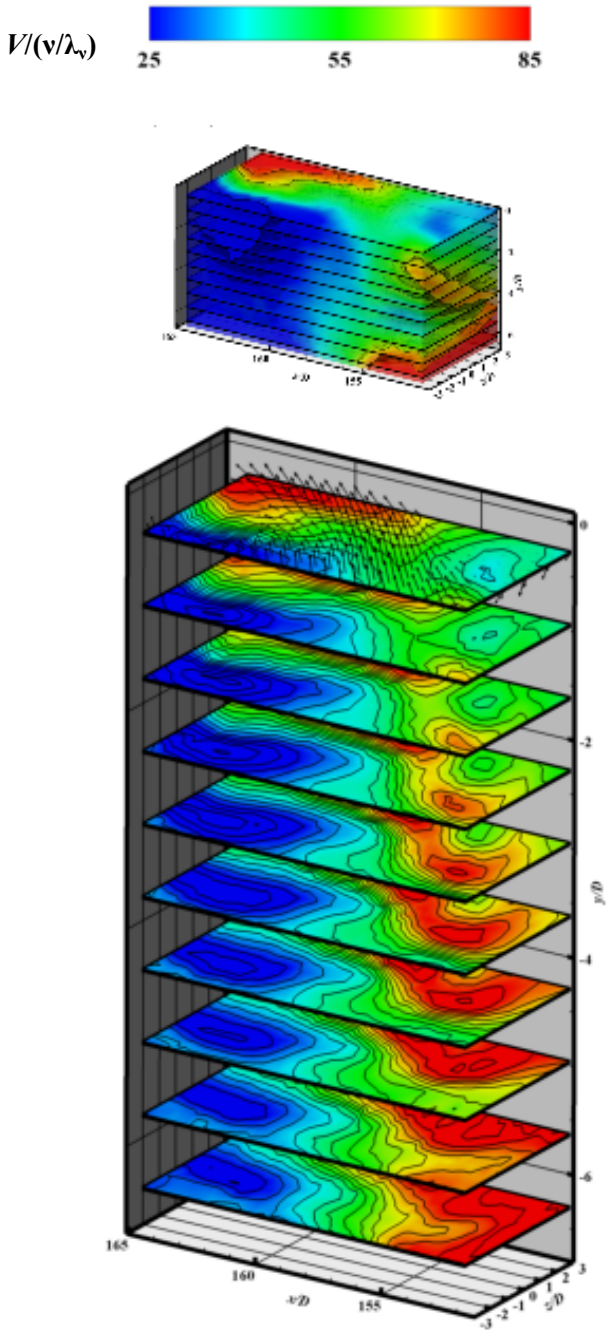

Figure 5.13. Example of the velocity magnitude contour plot at *x-y* planes. These planes are reconstructed from the scanned x-y planes shown in Fig. 5.11.

a)

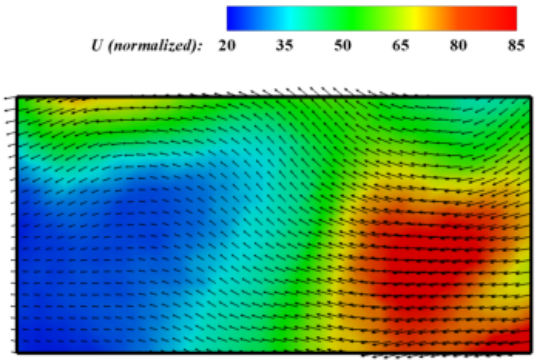

b)

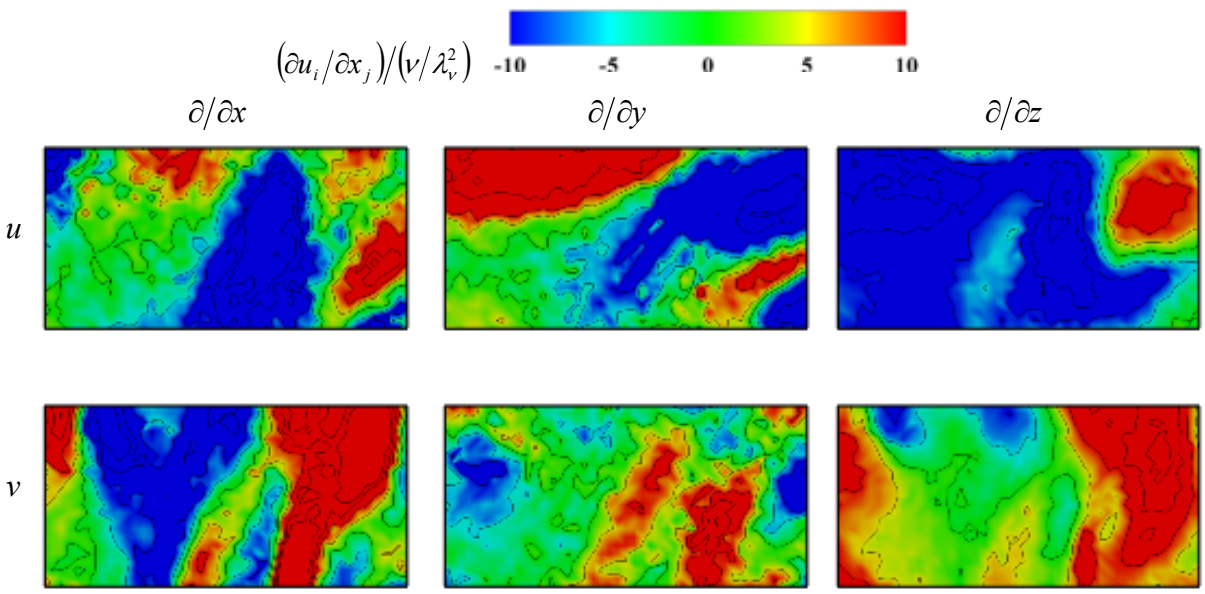

Figure 5.14. Instantaneous velocity gradient contour plots for a plane at *z/D* =-0.37. The velocities are normalized by ν/λ_ν.

a)

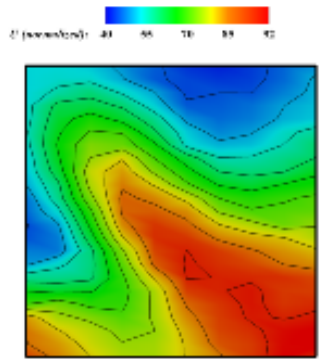

b)

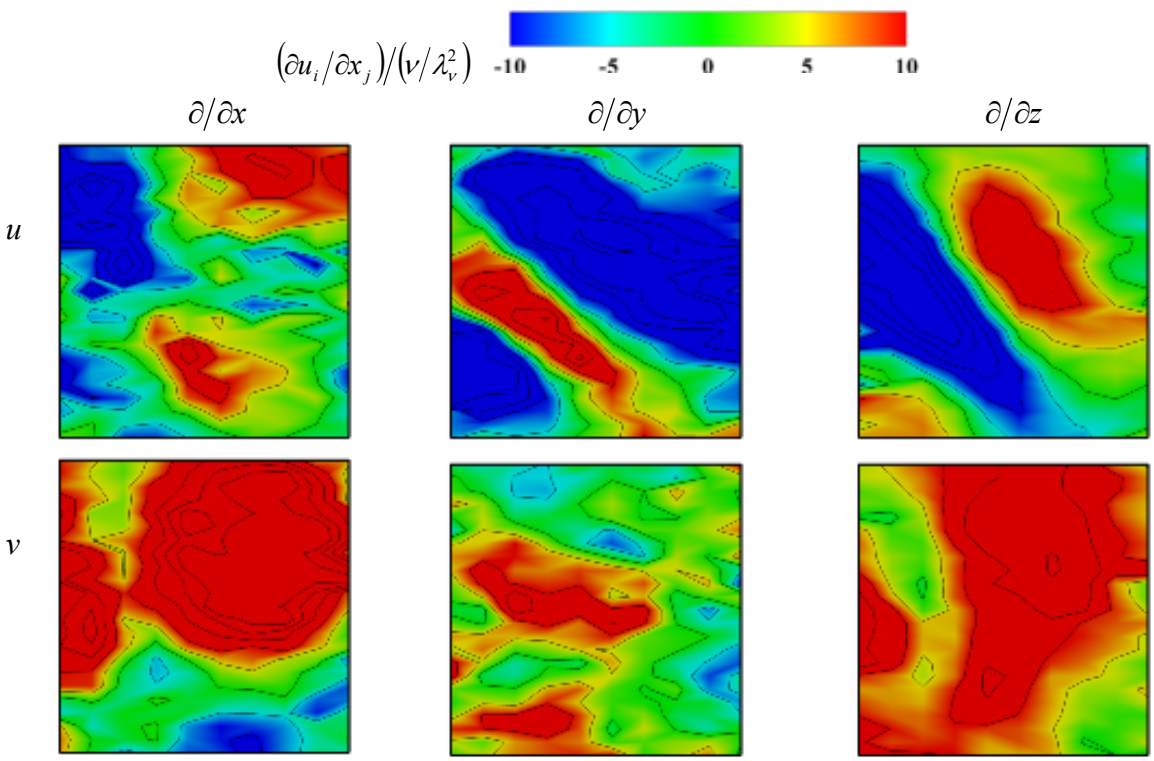

Figure 5.15. Instantaneous velocity gradient contour plots for a plane at *x/D* =153.8. The velocities are normalized by ν/λ_ν.

a)

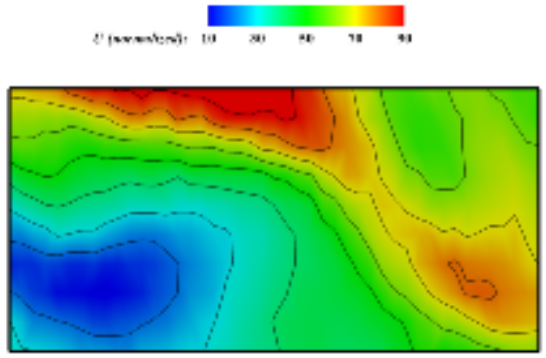

b)

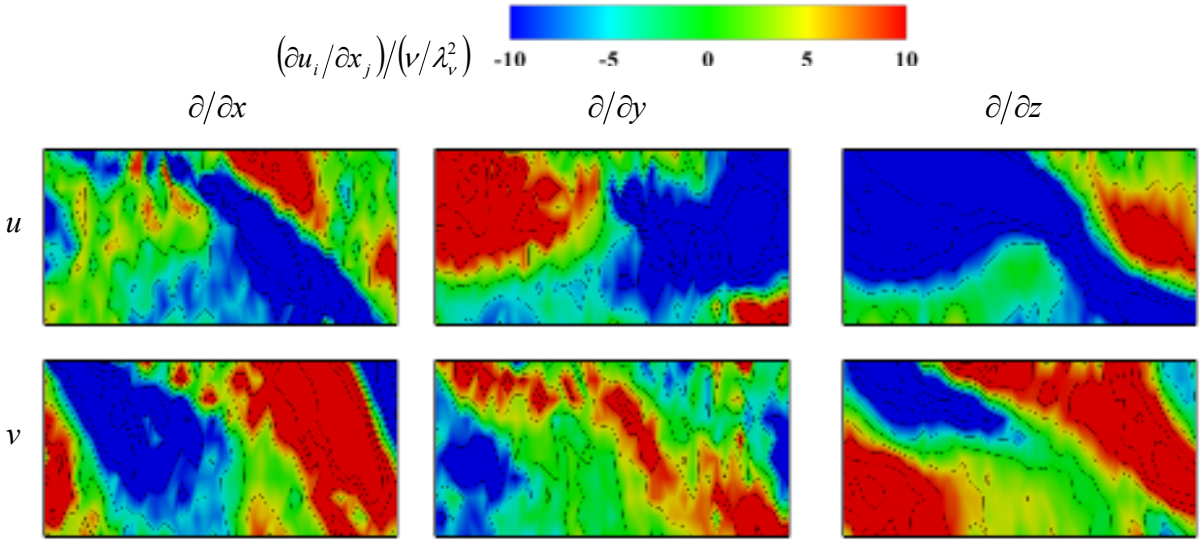

Figure 5.16. Instantaneous velocity gradient contour plots for a plane at *y/D* =-2.34. The velocities are normalized by ν/λ_ν.

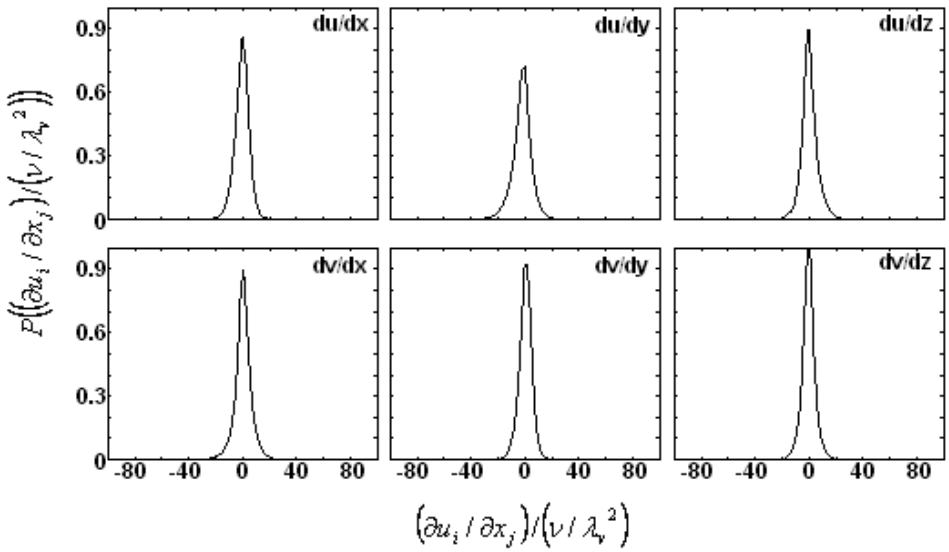

Figure 5.17. Probability density functions of the velocity gradients $\partial u / \partial x$, $\partial u / \partial y$, $\partial u / \partial z$, $\partial v / \partial x$, $\partial v / \partial y$ and $\partial v / \partial z$. Computed for the 10 independent sets (170 volumes).

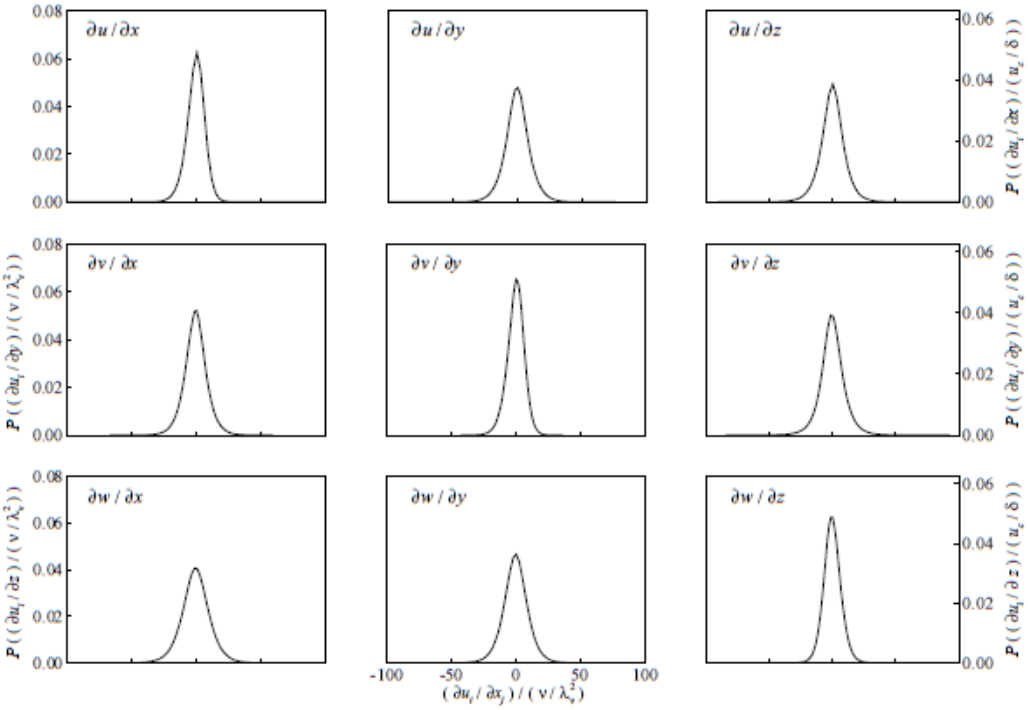

Figure 5.18. Probability density functions of the velocity gradients obtained by Mullin *et al* (2005) for a Re_δ=30,000

a)

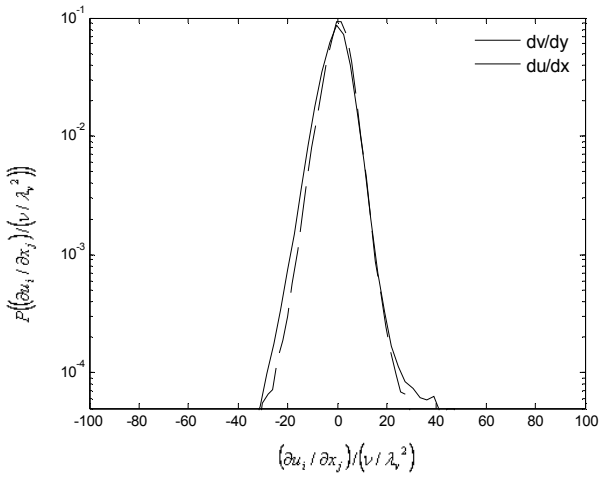

b)

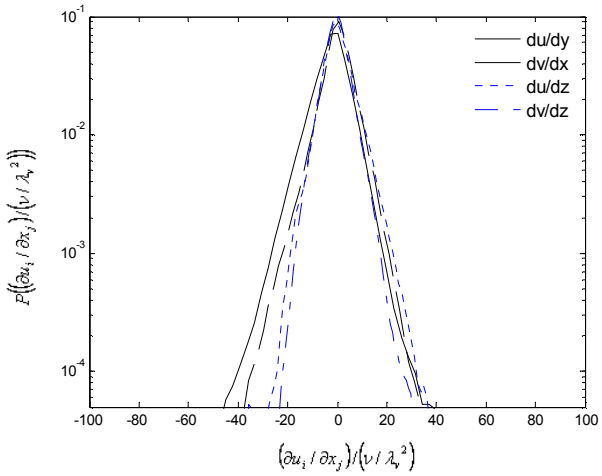

Figure 5.19. Pdfs of the velocity gradients, showing (a) on-diagonal (i=j) components, and (b) off-diogonal (i≠j) components, on semi-logarithmic axes.

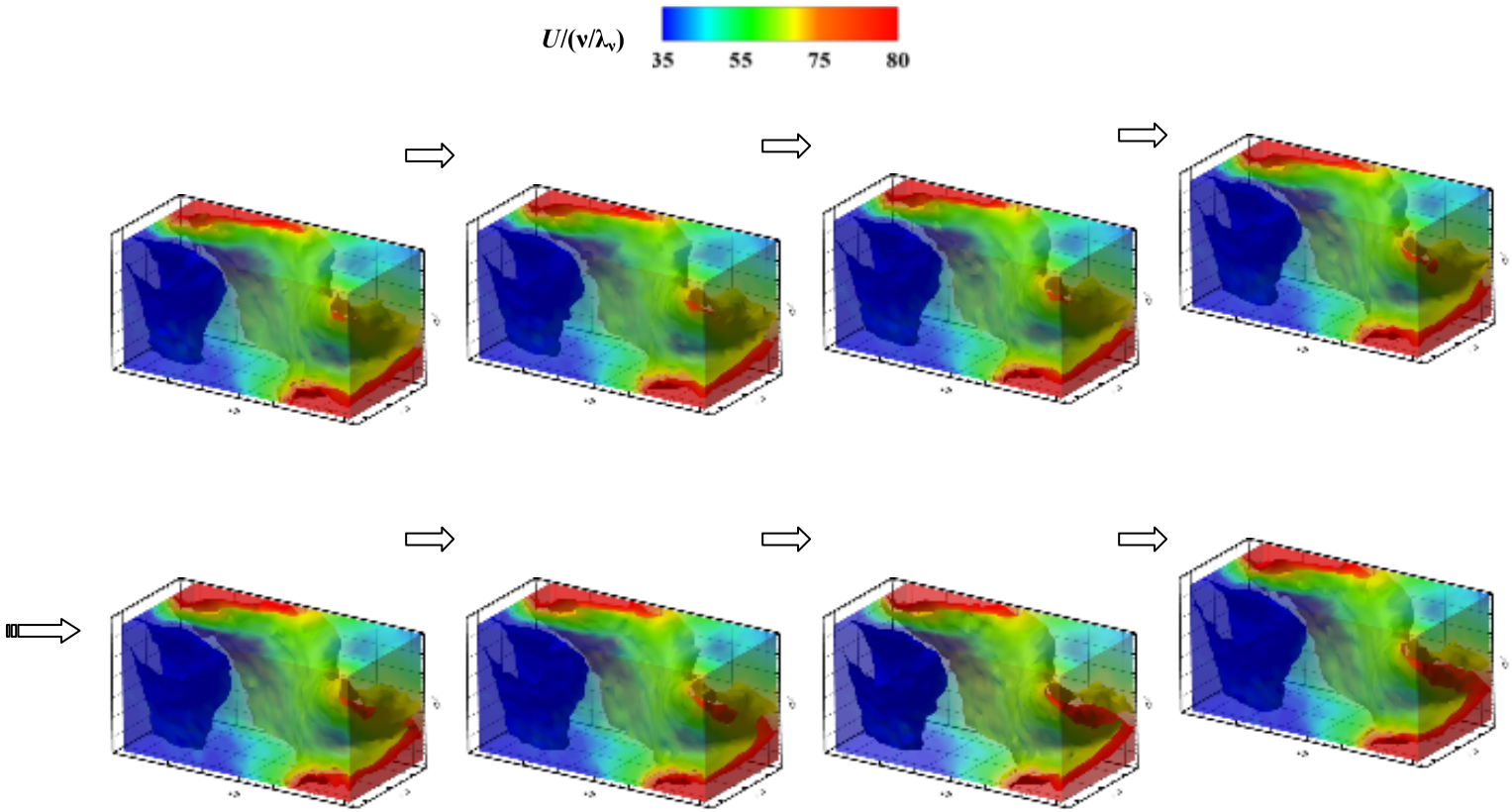

Figure 5.20. Isosurfaces of velocity magnitude (V=25, 70 & 80) for 8 consecutive volumes.

Chapter VI

Concluding Remarks

This chapter gives a summary of the results and conclusions from the present study on the development and implementation of a Time Resolved Scanning Particle Image Velocimetry technique for the study of the quasi-universal small scales in turbulent shear flows. Suggestions for future work are also included.

6.1 Review of Results

A criterion to determine the smallest turbulent flow scale measurable with the TR SPIV system has been proposed. The definition of the concept and procedure for the calculation of the "effective thickness" of the laser sheet is considered one of the key aspects in the proposed criterion. The distribution of particles observed by the camera across the laser sheet has been measured with a knife edge gap, and determined to be well approximated by a Gaussian fit. This distribution has been used to determine the maximum velocity component of the flow allowed across the laser sheet to guarantee a minimum number of particle image matches on the PIV cross-correlation process. The Taylor length and time scales of the flow have been associated with this maximum velocity, such that the particle groups enclosed in an interrogation window during the PIV process are required to keep

their velocity correlated to themselves for the time and space interval within the two laser pulses of the PIV process. As a result, the "effective thickness" of the laser sheet is determined, and is associated with the particles in the interrogation window. To satisfy a Nyquist sampling criteria, the measurable smallest length-scale of the flow is designated as half of the "effective thickness" measured. The smallest length-scale for the TR SPIV configuration used in this work was 4.24 mm.

As a consequence of this criterion, the laser sheet thickness and seeding particle density become determining factors in the spatial resolution of the PIV measurements, and by extension, in the Scanning PIV technique.

The results obtained validated the measurement technique in a turbulent jet. The flow was chosen such that the local Taylor scales at the measurement volume matched the requirements established. For that flow, the quasi-instantaneous volumetric 2-component velocity field was reconstructed. The spatial resolution of the velocity magnitude measurements seamed similar across the x- y- and z- directions of the volume. The similarity in the velocity isocontours between consecutive volume measurements confirms the high time resolution of the system for the present application; and the volume measurements are considered instantaneous. The pdfs of the velocity gradients were compared with literature using appropriate normalization, with good agreement. The comparison of the six velocity gradients obtained indicates for possible anisotropy of the flow, probably related to the shear forces.

6.2 Suggestion for future work

The present thesis work was mostly focused on the design and calibration of the TR SPIV system. Further analysis on the results obtained could be performed to study aspects such as the pdfs of the velocity, the non-isotropy observed on the velocity gradients, scaling laws, and vorticity profiles and statistics. The TR SPIV system could be used to analyze the small scales of other turbulent flows and allow a better understanding of the phenomena.

The use of a second camera in stereoscopic configuration, with a proper calibration process, would lead to full 3 velocity component volumetric vector fields. With such measurements, it would be possible to fully resolve and visualize the coherent structures at the small scales of turbulent flows.

REFERENCES

[1] S.B. Pope, Turbulent Flows, Cambridge University Press, 2000.

[2] J.A. Mullin, A study of velocity gradient fields at intermediate and small scales of turbulent shear flows via Dual-Plane Stereo Particle ImageVelocimetry, Ph. D. Thesis, Department of Aerospace Engineering, The University of Michigan, 2004.

[3] Y.I. Kaneda, T.; Yokokawa, M.; Itakura, K.; Uno, A. , Energy dissipation rate and energy spectrum in high resolution direct numerical simulations of turbulence in a periodic box, Physics of Fluids, v , n 2, p L21-4, Feb. 15 (2003) L21-24.

[4] R.J. Adrian, Multipoint optical measurements of simultaneous vectors in un-steady flow- a review, J. Heat and Fluid Flow 7 (1986) 127.

[5] M. Raffel, S. Werelye, J. Kompenhans, Particle Image Velocimetry. A practical guide., 2 ed., Springer, 1998.

[6] C. T. Li, K-C Chang, M.R.Wang, PIV measurements of turbulent flow in planar mixing layer, Experimental Thermal and Fluid Science 33 (2009) 527-537.

[7] C. Bruecker, Whole-volume PIV by the concept of a scanning light sheet: technique and application to 3D unsteady bluff body wakes, ASME/JSME Fluids Engineering and Laser Anemometry Conference and Exhibition, Fluids Engineering Division (Publication), 229 (1995) 115-121.

[8] S. Burgmann, C.B. cker, W.S. der, Scanning PIV measurements of a laminar separation bubble, Experiments in Fluids 41 (2006) 319–326.

[9] A.K. Prasad, R.J. Adrian, Stereoscopic particle image velocitmetry applied to liquid flows, Exp. Fluids 15 (1993) 49-60.

[10] T. Matsuda, J. Sakakibara, On the vortical structure in a round jet, Physics of Fluids 17 (2005) 025106.

[11] S. Burgmann, J. Dannemann, W. Schroder, Time-resolved and volumetric PIV measurements of a transitional separation bubble on an SD7003 airfoil, Exp. Fluids 44 (2007) 609-622.

[12] T. Hori, J. Sakakibara, High-speed scanning stereoscopic PIV for 3D vorticity measurement in liquids, Measurements science and technology 15 (2004) 1067–1078.

[13] J.A. Mullin, W.J.A. Dahm, Dual-plane stereo particle image velocimetry (DSPIV) for measuring velocity gradient fields at intermediate and small scales of turbulent flows, Experiments in Fluids 38 (2005) 185–196.

[14] C.W. M. Raffel, S. Werelye, J. Kompenhans, Analytical and experimental investigations of dual-plane particle image velocimetry, Optical Engineering 35 (1996) 2067-2074

[15] J.A.H, J. M. Coupland, Particle image velocimetry: three-dimensional velocity measurements using holographic recording and optical correlation, Applied Optics 31 (1992) 1005-1007.

[16] T.G. Hwang, D.H. Doh, K.Okamoto, 4D-PTV - measurements of an impinged jet with a dynamic 3D-PTV, Journal of Visualization 8 (2005) 245-252.

[17] G.E. Elsinga, F. Scarano, B. Wieneke, B.W.van Oudheusden, Tomographic particle image velocimetry, Experiments in Fluids 41 (2006) 933-947.

[18] M. Samimy, S.K. Lele,. Motion of particles with inertia in a compressible free shear layer, Phys. Fluids A3 (1991) 1915-1923

[19] N.T. Clemens, M.G. Mungal, A planar Mie scattering technique for visualizing supersonic mixing flows, Expts. Fluids 11(1991) 175-185

[20] K. Hoyer, M. Holzner, B. Luthi, M. Guala, A. Liberzon, W. Kinzelbach, 3D scanning particle tracking velocimetry, Exp. Fluids 39 (2005) 923-934

[21] Hecht, Eugene. 1989. Optics. Addison Wesley

[22] P.N. Papanicolau, Investigations of round verticlal turbulent buoyant jets, J. Fluid Mech 195 (1988) 341-391

[23] F.J Diez., W.J.A. Dahm, Effects of heat release on turbulent shear flows. Part 3. Bouyancy effects due to heat release in jets and plumes, J. Fluid Mech. 575 (2007) 221-251

[24] F. John, J.E. Marsden, L. Sirovich, Applied Mathematical Sciences, Springler-Verlag, 1991

[25] A. N. Kolmogorov, A refinement of previous hypotheses concerning the local structure of turbulence in viscous incompressible fluid at high Reynolds number, J. Fluid Mech., 13 (1936) 82-85

[26] C. A. Friehe, C. W. Van Atta, C. H. Gibson, Jet turbulence: dissipation rate measurements and correlations, Turbulent shear flows CP-93 (1971) 18-1-7

[27] R. D. Keane and R. J. Adrian, Theory of cross-correlation analysis of PIV images, Applied Scientific Research, 49 (1992) 191-215

[28] I. Wygnanski, H. Fiedler, Some measurements in the self-preserving jet, J. Fluid Mech., 38 (1969) 577-612.

[29] N. Ninomiya, N. Kasaki, Measurement of the Reynolds stress budgets in an axisymmetric free jet with the aid of three-dimensional particle tracking velocimetry. Proc. Ninth Symposium on “Turbulent Shear Flows” (1993) Kyoto, Japan

`